

AD-A276 844



2

WL-TR-93-3099

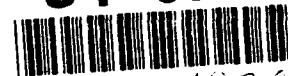


**ACTIVE CONTROL FOR FIN BUFFET ALLEVIATION**

Holt Ashley  
Stephen M. Rock  
Ramarao Digumarthi  
Kenneth Chaney  
Alfred J. Eggers, Jr.  
*RANN, Incorporated*  
260 Sheridan Avenue, Suite 414  
Palo Alto, CA 94306 -2011

DTIC  
SELECTE  
MAR 11 1994  
S E D

94-07886



411929

JANUARY 1994  
FINAL REPORT FOR PERIOD JUNE 1992 - JUNE 1993

**APPROVED FOR PUBLIC RELEASE; DISTRIBUTION IS UNLIMITED**

FLIGHT DYNAMICS DIRECTORATE  
WRIGHT LABORATORY  
AIR FORCE MATERIEL COMMAND  
WRIGHT PATTERSON AIR FORCE BASE, OHIO 45433-7562

94 3 10 014

NOTICE

*When Government drawings, specifications, or other data are used for any purpose other than in connection with a definitely Government-related procurement operation, the United States Government thereby incurs no responsibility nor any obligation whatsoever; and the fact that the government may have formulated, furnished, or in any way supplied the said drawings, specifications, or other data, is not to be regarded by implication or otherwise as in any manner licensing the holder or any other person or corporation, or conveying any rights or permission to manufacture use, or sell any patented invention that may be any way related thereto.*

*This report is releasable to the National Technical Information Service (NTIS). At NTIS, it will be available to the general public, including foreign nations.*

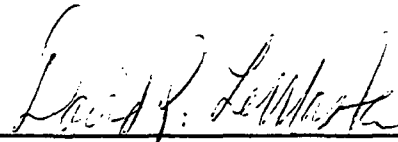
*This technical report has been reviewed and is approved for publication.*



**ALEXANDER H. HSIA**  
Project Engineer  
Control Dynamics Branch  
Flight Control Division



**FRANK R. SWORTZEL, Chief**  
Control Dynamics Branch  
Flight Control Division



**DAVID P. LEMASTER, Chief**  
Flight Control Division  
Flight Dynamics Directorate

*If your address has changed, if you wish to be removed from our mailing list, or if the addressee is no longer employed by your organization please notify WL/FIGC, 2210 Eighth St Ste 21, Wright-Patterson Air Force Base, OH 45433-7531 to help us maintain a current mailing list.*

*Copies of this report should not be returned unless return is required by security considerations, contractual obligations, or notice on a specific document.*

# REPORT DOCUMENTATION PAGE

Form Approved  
OMB No. 0704-0182

Public reporting burden for this collection of information is estimated to average 1 hour per response, including the time for reviewing instructions, searching existing data sources, gathering and maintaining the data needed, and completing and reviewing the collection of information. Send comments regarding this burden estimate or any other aspect of this collection of information, including suggestions for reducing this burden, to Washington Headquarters Services, Directorate for Information Operations and Reports, 1215 Jefferson Davis Highway, Suite 1204, Arlington, VA 22202-4302, and to the Office of Management and Budget, Paperwork Reduction Project (0704-0182), Washington, DC 20503.

1. AGENCY USE ONLY (Leave blank)      2. REPORT DATE      3. REPORT TYPE AND DATES COVERED  
 JANUARY 1994      FINAL, 06/01/92 -- 06/30/93

4. TITLE AND SUBTITLE      5. FUNDING NUMBERS

ACTIVE CONTROL FOR FIN BUFFET ALLEVIATION

C F33615-92-C-3605  
 PE 62201  
 PR 2403  
 TA 05  
 WU 98

6. AUTHOR(S)

H. ASHLEY, S.M. ROCK, R. DIGAMURTHI, K. CHENEY  
 AND A.J. EGGERS, JR.

7. PERFORMING ORGANIZATION NAME(S) AND ADDRESS(ES)      8. PERFORMING ORGANIZATION REPORT NUMBER

RANN, INC.  
 260 SHERIDAN AVE, STE 414  
 PALO ALTO, CA 94306-2011

9. SPONSORING / MONITORING AGENCY NAME(S) AND ADDRESS(ES)      10. SPONSORING / MONITORING AGENCY REPORT NUMBER

FLIGHT DYNAMICS DIRECTORATE  
 WRIGHT LABORATORY  
 AIR FORCE MATERIEL COMMAND  
 WRIGHT-PATTERSON AFB, OH 43433-7562

WL-TR-93-3099

11. SUPPLEMENTARY NOTES

12a. DISTRIBUTION / AVAILABILITY STATEMENT      12b. DISTRIBUTION CODE

APPROVED FOR PUBLIC RELEASE; DISTRIBUTION IS UNLIMITED

13. ABSTRACT (Maximum 200 words)

THIS REPORT SUMMARIZES WHAT HAS BEEN LEARNED, DURING ONE YEAR OF CONTRACT EFFORT, REGARDING THE USE OF ACTIVE CONTROL TO ENHANCE THE STRUCTURAL LIFE OF TWIN VERTICAL STABILIZERS ON AIRCRAFT WHICH ROUTINELY OPERATE TO HIGH ANGLES OF ATTACK. THESE DORSAL SURFACES HAVE IN SEVERAL INSTANCES EXPERIENCED UNANTICIPATED SEVERE BUFFETING DUE TO BURSTING OF WING-LEADING-EDGE VORTICES. ON BOTH EXISTING AND FUTURE DESIGNS, ACTIVE CONTROL IS SHOWN TO OFFER AN ALTERNATIVE TO THE WEIGHT PENALTY OF STRUCTURAL REINFORCEMENT AS A WAY OF AVOIDING DAMAGE. A SUMMARY OF PRIOR RESEARCH RELEVANT TO THE SUBJECT IS FOLLOWED BY A DESCRIPTION OF THEORETICAL METHODOLOGY BASED ON SUPERPOSITION OF NORMAL VIBRATION MODES. IN AN APPENDIX, A REFINED FORMULATION IS GIVEN FOR THE STATISTICS OF THE BUFFETING AIRLOADS. THE F/A-18 AND F-15 ARE USED AS EXAMPLES. ON THE FORMER, SUBSTANTIAL FATIGUE LIFE ENHANCEMENT IS SHOWN POSSIBLE BY DRIVING THE RUDDER IN RESPONSE TO MEASURED FIN-TIP ACCELERATION. THIS SIMPLE APPROACH FAILS ON THE F-15, BUT A SMALL CONTROLLABLE VANE ATTACHED TO THE FIN CAN AMELIORATE BUFFETING QUITE SATISFACTORILY. THE F-15 ANALYTICAL MODEL MUST BE IMPROVED, HOWEVER, BEFORE THE FINDINGS ARE APPLICABLE TO FULL-SCALE.

14. SUBJECT TERMS      15. NUMBER OF PAGES

ACTIVE CONTROL, TAIL BUFFET, AEROSERVOELASTICITY,  
 INTEGRATED STRUCTURES AND CONTROL

142

15. PRICE CODE

17. SECURITY CLASSIFICATION OF REPORT      18. SECURITY CLASSIFICATION OF THIS PAGE      19. SECURITY CLASSIFICATION OF ABSTRACT      20. LIMITATION OF ABSTRACT

UNCLASSIFIED

UNCLASSIFIED

UNCLASSIFIED

UL

FOREWORD

The research reported here was performed by RANN, INC., Palo Alto CA, under Air Force Contract F33615-92-C-3605, entitled "Active Control for Fin Buffet Alleviation." This was supported by Flight Dynamics Directorate, USAF Wright Laboratory, Wright-Patterson Air Force Base OH, with Capt Alexander H. Hsia (WL/FIGCC) as Project Monitor, during the period 1 June 1992 through 30 June 1993.

The Principal Investigator was Dr. Holt Ashley. The authors of this report wish to acknowledge the substantial assistance of several engineers from McDonnell Aircraft Company, especially Mr. Rudolph Yurkovich, as well as the continuing cooperation of Capt Hsia and Dr. James Olsen, Chief Scientist, Flight Dynamics Directorate.

Accession For	
NTIS CRA&I	<input checked="" type="checkbox"/>
DTIC TAB	<input type="checkbox"/>
Unannounced	<input type="checkbox"/>
Justification .....	
By .....	
Distribution / .....	
Availability Codes	
Dist	Avail and/or Special
A-1	

## TABLE OF CONTENTS

<u>Section</u>	<u>Page</u>
FOREWORD . . . . .	iii
LIST OF FIGURES . . . . .	vii
DEFINITIONS OF PRINCIPAL SYMBOLS . . . . .	x
1.0 INTRODUCTION . . . . .	1
2.0 ANALYSIS OF THE FIN STRUCTURAL DYNAMICS; ASSOCIATED AERODYNAMIC TERMS . . . . .	5
2.1 MODAL EQUATIONS OF MOTION . . . . .	5
2.2 MOTION-DEPENDENT AERODYNAMICS . . . . .	7
2.3 REDUCTION DUE TO $\alpha$ IN THE EFFECTIVE DYNAMIC PRESSURE . . . . .	9
2.4 AERODYNAMIC INPUTS DUE TO BUFFETING; RESPONSE BY POWER SPECTRAL METHODS . . . . .	10
3.0 STATE-VECTOR FORMULATION AND ACTIVE CONTROL . . . . .	18
3.1 PHILOSOPHY OF CONTROL SYSTEM DESIGN . . . . .	18
3.2 THE STATE-VECTOR FORMULATION . . . . .	20
3.3 FATIGUE LIFE ESTIMATION . . . . .	24
4.0 RESULTS OF CONTROL SYSTEM ANALYSIS . . . . .	28
4.1 THE F/A-18 AIRCRAFT . . . . .	28
4.2 THE F-15 AIRCRAFT . . . . .	59
5.0 CONCLUSIONS AND RECOMMENDATIONS . . . . .	85
REFERENCES . . . . .	87
APPENDIX A DERIVATION AND CALCULATION OF SPECTRA OF BUFFETING INPUT PRESSURES AND AIRLOADS . . . . .	92
A.1 MATHEMATICAL BACKGROUND . . . . .	92
A.2 EXAMPLE OF THE F/A-18 . . . . .	100
A.3 EXAMPLE OF THE F-15 . . . . .	104
APPENDIX B SUMMARY OF PRIOR AND CONCURRENT RESEARCH . . . . .	111
B.1 PAST EXPERIENCE WITH BUFFETING . . . . .	111
B.2 MEASUREMENT AND PREDICTION OF THE FLOWFIELD ABOVE SWEPTBACK WINGS AT HIGH $\alpha$ . . . . .	113
B.3 MEASUREMENT AND PREDICTION OF "OPEN-LOOP" BUFFET RESPONSE . . . . .	120
B.4 PASSIVE AND ACTIVE CONTROL OF FIN BUFFETING . . . . .	125

LIST OF FIGURES AND TABLES

<u>Figure</u>		<u>Page</u>
1	F-15 Eagle at $\alpha = 22^\circ$ , showing typical streamlines defining the flow affecting the vertical stabilizers (from Ref. 1).	2
2	Dimensionless PSD of buffeting pressure at $\alpha = 32^\circ$ for a typical location on the F/A-18 fin.	15
3	The objective is to use a feedback control law to modify the transfer function from $\Delta C_p$ to bending moment or some other quantity which measures fatigue damage.	19
4	Vertical tail structure of F/A-18 with skin removed.	26
5	Geometry and dimensions of an F/A-18 fin and rudder.	29
6	Distributions of flexural and torsional stiffness along the E.A. of fixed portion of an F/A-18 fin.	30
7	Dimensions and C.G. locations for a sectional approximation to F/A-18 fin and rudder.	31
8	Nodes and beam elements for the ALGOR model approximating an F/A-18 fin and rudder.	32
9	Three-quarter views of the four lowest-frequency natural modes of the F/A-18 fin/rudder. Circles identify nodes in the deflected positions. Each part compares the predicted frequency with laboratory measurement.	34
9	Continued	35
10	Trapezoidal area elements used by LATIS1 in calculating air loads on F/A-18 fin & rudder.	36
11	Curve-fit to the aerodynamic coefficient $\bar{A}_{11}$ for F/A-18 fin in form of Eq. (18).	38
12	Curve-fit to the aerodynamic coefficient $\bar{A}_{1R}$ for F/A-18 fin in form of Eq. (19) with $u = \delta_R$ .	39
13	Effect of angle of attack on the yawing moment derivative $dC_N/d\delta$ due to rudder, as measured in flight on the High- $\alpha$ Research Vehicle.	40
14	Spatial variation of buffet characteristics at constant air speed, angle-of-attack and density.	42
15	Variation of buffet pressure characteristics with angle-of-attack at constant air speed and density.	43
16	Dimensionless amplitude and phase angle of transfer function from rudder command $\delta_{RC}$ to first- and third-mode amplitudes $q_1$ , plotted vs. input frequency for the reference F/A-18 flight condition.	46
17	Predicted PSD (lower curve) vs. flight-measured PSD (upper curves) for acceleration at instruments near the CF-18 fin tips. LEX fence was on. Altitude 10,000 ft.	47
18	PSD of F/A-18 fin root bending moment due to buffeting at $\alpha = 32^\circ$ , $q_\infty = 300$ psf, sea level. Solid curve is open-loop; dashed curve for fin-tip acceleration feedback to cause RMS $\delta_R \approx 3.2^\circ$ .	51

19	PSD of rudder angle required to reduce RMS fin-root bending moment by 33%. . . . .	51
20	Effect of increasing RMS rudder displacement on relative RMS bending moment at root of F/A-18. (Same flight condition as Fig. 18.) . . . . .	52
21	Same as Fig. 20, except only for frequencies in the range 10-20 Hz. . . . .	52
22	Same as Fig. 20, except only for frequencies in the range 32-55 Hz. . . . .	53
23	Relative damage to F/A-18 fin root. . . . .	58
24	Exploded view of right- & left-hand F-15 fins and stabilators, with details of structural layout and fin materials. . . . .	60
25	Nodes and elements for F.E. model of F-15 fin and rudder. Concentrated inertias are assigned to each node, but only the elements along the E.A.'s have finite beam-rod elasticities. . . . .	61
26	Nodes and elements for F.E. model of F-15 all-movable stabilator and aft-fuselage boom. (Property assignments similar to Fig. 25.) . . . . .	61
27	F-15 first bending mode, as seen from rear. $F_1 = 10.87$ Hz <u>vs.</u> measured 9.2 - 9.8 Hz. . . . .	62
28a	F-15 second combined mode, as seen from rear. $F_2 = 27.06$ Hz <u>vs.</u> measured 30 Hz. . . . .	63
28b	F-15 second combined mode ("Stick-Figure" fin, rudder, stabilator and aft fuselage boom, seen in three-quarter view). . . . .	63
29	F-15 first fin torsion mode, seen in three-quarter view. $F_3 = 41.23$ Hz <u>vs.</u> measured 32 Hz. . . . .	64
30	F-15 second bending mode (with rudder rotation, as seen from rear). $F_4 = 44.1$ Hz <u>vs.</u> measured 36.5 Hz. . . . .	64
31	PSD of the pressure in psi, measured at station #7 ( $x = 17.15$ in, $z = 94.05$ in, according to system used here) on a 13%-scale model of a rigid F-15 fin (Ref. 1). $\alpha = 22^\circ$ ; $q_\infty = 12$ psf. . . . .	69
32	PSD of Fig. 31, plotted <u>vs.</u> dimensionless frequency and normalized to unit area under the curve. . . . .	70
33	Root locus plot for feedback from F-15 fin accelerometer A1 to rudder command. Scales are in $\text{sec}^{-1}$ . . . . .	73
34	Root locus plot for feedback from F-15 fin accelerometer A2 to rudder command. Scales are in $\text{sec}^{-1}$ . . . . .	74
35	Root locus plot for feedback from F-15 fin accelerometer A3 to rudder command. Scales are in $\text{sec}^{-1}$ . . . . .	75
36	Root locus plot for feedback from F-15 fin accelerometer A4 to rudder command. Scales are in $\text{sec}^{-1}$ . . . . .	76
37	F-15 fin and rudder with tip vane. . . . .	78
38	Input and response PSD's for tip-vane control of buffeting of F-15 fin at $\alpha = 22^\circ$ , $q_\infty = 245$ psf. Dashed A2 acceleration curve is open loop, solid curve for a relative feedback gain of 0.1. . . . .	81
39	Same as Fig. 38, except feedback gain of 0.25. . . . .	82
40	Same as Fig. 38, except feedback gain of 0.5. . . . .	83

41	Pressure transducer locations on a 13%-scale model of F-15 fin/rudder. (Dimensions are in inches except for percent-chord lines.) . . . . .	105
42	Location of the measurement plane. (Figure 3 of Ref. 33). . . . .	116
43	Velocity vector $ u_{yz} $ in the measurement plane at $\alpha = 15.0^\circ$ , $\alpha = 25.0^\circ$ and $\alpha = 30.0^\circ$ ; $Re = 1.0 \times 10^6$ . (Adapted from Fig. 4 of Ref. 33.) . . . . .	118
44	Contours of dimensionless RMS lateral crossflow velocities $\sqrt{v'^2}/U_\infty$ in the measurement plane at five $\alpha$ 's. (Adapted from Fig. 13, Ref. 33. Numbers are percent.) . . . . .	119

Table

Page

1	Relative fatigue damage with and without active control. . . . .	56
2	Influence of angle of attack on averaged effective dynamic pressure over the F-15 fin/rudder. . . . .	68
3	Coordinates, in two reference frames, of four accelerometers mounted on the right F-15 fin. . . . .	71
4	Root-mean-square levels of acceleration and tip-vane angle associated with the four levels of control in Figs. 38-40. . . . .	80
A1	Dimensionless RMS $\Delta p$ 's from Ref. 11, along with estimated corresponding quantities from Ref. 5. $\alpha = 32^\circ$ , $q_\infty = 7.5$ psf. . . . .	103



## DEFINITIONS OF PRINCIPAL SYMBOLS\*

- a Acceleration (often reported in g's).
- A, B, D, H Matrices involved in state-vector forms of equations of motion and measurement. [See Eqs. (24) & (25).]
- $A_{mi}$   $i^{\text{th}}$  inertia moment defined by Eq. (32).
- $A_{ij}$  Dimensionless aerodynamic generalized force on  $i^{\text{th}}$  mode due to unit motion in  $j^{\text{th}}$  mode.
- $A_{iR}$  Dimensionless aerodynamic generalized force exerted by rudder on  $i^{\text{th}}$  mode.
- $b_r$  Reference length involved in definition of Strouhal No.
- $C_p = \frac{p-p_\infty}{q_\infty}$  Pressure coefficient.
- CSD(...) Cross-spectral density relating the quantities in parens.
- f Vibration frequency in Hz.
- $F = \frac{fb_r}{U_\infty}$  Reduced frequency or Strouhal No.; F is also force input.
- g Standard Earth gravity ( $386 \text{ in/s}^2$ ).
- h Height to aerodynamic center of tip-vane.
- $H_{ij}$  Complex frequency response function relating input j to output i.

---

\*For the most part, units of dimensioned quantities used in this report are in the inch-second-pound force system. The conversion to S.I. units is a well-known process.

$i = \sqrt{-1}$       Imaginary unit.

$i, j$       Summation indices used for modal superposition, etc.

$I_{\theta}$       Rotary inertia about x-direction.

$k, \ell$       Summation indices running over area elements on fin/rudder.

$K_k, K_{k\ell}$       Ratios of RMS  $\Delta p$  to RMS pressure at reference station.

$m$       Mass per unit area of lifting surface.

$M$       Mach No.; bending moment; number of area elements.

$M_i$       Generalized mass of  $i^{\text{th}}$  mode.

$M_j$       Mass of  $j^{\text{th}}$  area element.

$N$       Number of modes; yawing moment.

$p$       Pressure.

$\text{PSD}(\dots)$       Power spectral density of quantity in parens.

$q$       Dynamic pressure of airstream.

$q_i$       Coordinate defining displacement of  $i^{\text{th}}$  mode.

$Q_i$       Aerodynamic generalized force acting on  $i^{\text{th}}$  mode.

$R_{ii}$       Autocorrelation function for quantity  $(\dots)_i$ .

$R_{ij}$       Cross-correlation function between quantities  $(\dots)_i$  and  $(\dots)_j$ .

$s$       Laplace transform variable.

$x_i$

S	Plan area of lifting surface
$[S_q], [S_Q]$	Matrices of output & input PSD's & CSD's, respectively.
t	Time coordinate.
$U_\infty$	Speed of flight or free stream.
[V]	Column matrix or vector.
x,y	State vectors used in control analysis.
x,y,z	Rectangular Cartesian coordinates (see Fig. 1). [y is also used for displacement of structure in y-direction.]
Y	Aerodynamic force in y-direction.
$\alpha$	Angle of attack.
$\beta$	Sideslip angle.
$\Gamma$	Distribution matrix for buffeting pressure in state-vector Eq. (26).
$\delta_R, \delta_V$	Angle of rotation of rudder & tip vane, respectively.
$\zeta_i$	Critical damping ratio of $i^{\text{th}}$ mode.
$\xi, \eta$	Dummy variables replacing x,z in integrals over the fin area.
$\rho$	Air density.
$\Sigma$	Summation.
$\tau$	Lag time in correlation function.

- $\phi_i$  Dimensionless shape of normalized  $i^{\text{th}}$  mode.
- $\mathbf{B}$  Distribution matrix for buffeting pressure in measurement Eq. (27). Phase angle of CSD.
- $\omega = 2\pi f$  Circular frequency of simple harmonic motion.
- $\omega_i$  Undamped natural frequency of  $i^{\text{th}}$  mode.

Subscripts, Superscripts, etc.

- ( )<sub>a</sub> Identifies accelerometer location.
- (...)<sub>C</sub> Identifies a control input.
- (...)<sub>D</sub> Identifies disturbance input due to buffeting pressures.
- (...)<sub>F</sub> Quantity related to vertical stabilizer (fin).
- (...)<sub>i</sub> Property of  $i^{\text{th}}$  vibration mode.
- (...)<sub>iM</sub> Identifies input due to motion in  $i^{\text{th}}$  mode.
- (...)<sub>R</sub> Quantity related to the rudder.
- (...)<sub>T</sub> or (...)<sub>V</sub> Quantity related to tip-vane.
- (...)<sub>∞</sub> Property of free stream approaching aircraft in flight.
- ( $\dot{\quad}$ ) Derivative with respect to time.
- ( $\overline{\quad}$ ) Complex amplitude of simple harmonic quantity; time average.
- (...)\* Complex conjugate.

- $\Delta(\dots)$  Discontinuity in pressure, etc. between two sides of surface.
- $[\dots]$  Sometimes used to define a matrix or vector.
- $|\dots|$  Magnitude of complex quantity.

## 1.0 INTRODUCTION

Commencing June 1, 1992, and supported by USAF Flight Dynamics Directorate under Contract F33615-92-C-3605, RANN, INC., undertook a 1-year program of research with the following objective: for fighter aircraft with twin vertical stabilizers, which operate to high angle of attack  $\alpha$ , to examine the possibility that active control can alleviate the response to buffeting and enhance fatigue life of the structure. Although there is no way that the phenomenon could have been anticipated during the initial phases of their design, "fin buffeting" as a consequence of high- $\alpha$  maneuvers has been encountered on several military aircraft with such twin tails. For example, a detailed description and structural consequences in the case of F-15 will be found in Refs. 1 and 2\*. Other affected fighters include F-14 and F/A-18. Future designs for which some level of buffeting is anticipated are F-22, with measurements on a wind-tunnel model already reported in Ref. 3, the European EFA and French Rafale. Although they have single, center-line vertical stabilizers, similar phenomena have occurred at high  $\alpha$  on X-29 and X-31; see Ref. 4 for measurements of associated vortex behavior on the latter research vehicle.

Subsequent sections and Appendix B provide more information and literature citations on the vortical/turbulent flow-field responsible for the fin excitation, on the nature of

---

\*Figure 1 depicts two views of the F-15 configuration.

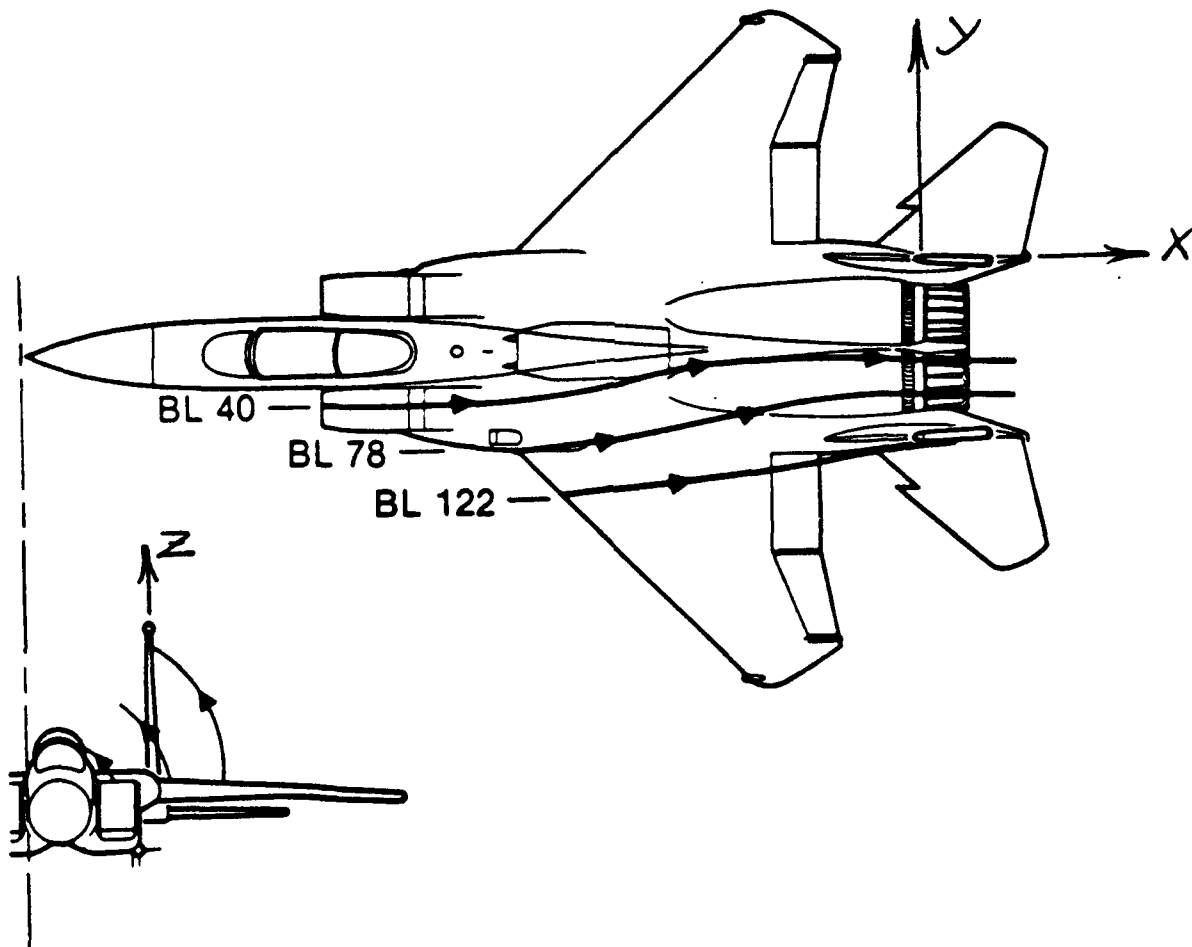


Figure 1. F-15 EAGLE at  $\alpha = 22^\circ$ , showing typical streamlines defining the flow affecting the vertical stabilizers (from Ref. 1).

the response and on measures which have been taken to ameliorate the observed damage. During early operational deployment of both F-15 and F/A-18, buffet-induced cracking was encountered at various fin-structure locations. The corrective action involved strengthening and stiffening, which by both laboratory test and flight experience appear to have ensured adequate life in the fleets. In addition small "fences" installed on the F/A-18 leading-edge extensions (LEX) succeeded in reducing the response by approximately 50% (see, e.g., Ref. 5). This has unfortunately

been a costly experience, as one can infer from the several necessary reinforcements depicted in Fig. 30 of Ref. 5.

With regard to future vehicles as well as for anticipated new models of existing aircraft, a question which has received only limited attention (see e.g., Ref. 1, Vol. I, p. 29) is whether practicable active-control measures might have promise for significant structural life extension. The present report summarizes what RANN, INC. has learned about this issue during the first year of contract effort. The initial focus of research was on F/A-18, owing to the availability of extensive useful data supplied by the manufacturer. Its powered rudder turns out to be a surprisingly effective instrument for increasing the estimated structural life. Furthermore, a preliminary analytical model of the F-15 empennage has also been developed and examined for buffet response amelioration by means of both the rudder and a small rotatable vane attached to the fin tip. Although the results achievable with the latter device appear promising, it is emphasized that the current F-15 structural representation has inadequacies that require adjustment.

By way of organization, this report summarizes in an Appendix the most significant prior investigations relevant to fin buffeting, including the few proposed attempts at passive or active control. Based on linear superposition of normal modes of free vibration, Sect. 2 describes the theoretical "plant" which here serves as the object for active control studies. Specially emphasized is the scheme for approximating the random inputs due



to buffeting flow, which rely on published measurements from scale models. Another Appendix addresses the difficult question of partial spatial correlation among the forcing pressures at different stations over the fin.

Turning to active control, the next section describes the state-vector formulation of the equations of motion and certain approximations necessitated by this approach. The sensors and effectors available to the system designer are discussed. Some details are given regarding control theory, as is the scheme adopted for estimating the relative effects of buffet alleviation on the fatigue life of fin structure. Finally, the results of control system analyses are presented in detail for both of the chosen aircraft.

## 2.0 ANALYSIS OF THE FIN STRUCTURAL DYNAMICS; ASSOCIATED AERODYNAMIC TERMS

### 2.1 MODAL EQUATIONS OF MOTION

Chapters 3 and 4 of Ref. 6 and numerous other texts explain how natural modes of free, undamped vibration offer an efficient tool for the analysis of forced motion of linear elastic systems. As for the two aircraft which are the objects of investigation herein, isolated modes of a single half-tail -- restrained by attachment to the rest of the fuselage in essentially cantilever fashion -- appear quite adequate to represent fin buffeting, which is very nearly a linear phenomenon both structurally and aerodynamically (cf. the prediction methods of Refs. 5, 6 and 7). As will be seen, superimposed cantilever modes of the fin alone do the job on the F/A-18. The F-15 empennage structure is more complicated, however, so that motion of the stabilator and a supporting aft-fuselage boom must be accounted for.

A convenient system of Cartesian coordinates is illustrated in Fig. 1, with the origin located somewhere along the root of the right fin,  $x$  aft and  $z$  upward in the plane of the surface. Right and left fins can be treated independently, and at least in the case of F/A-18 there is complete mirror symmetry between the two. Because the structure is very stiff in-plane, one need consider only displacements in the  $y$ -direction measured from the unstrained position. Let the dimensionless function  $\phi_i(x,z)$  define the  $i^{\text{th}}$  vibration mode. Then the modal-superposition

assumption states that any time-dependent displacement can be written

$$y(x,z,t) = \sum_{i=1}^N q_i(t) \phi_i(x,z) \quad (1)$$

N is the number of modes required to ensure adequate convergence -- 3 for F/A-18, 4 for F-15, but possibly larger for more complicated structures with more closely spaced natural frequencies. As shown in the texts, each modal coordinate  $q_i(t)$  is governed by the differential equation (overwritten "dots" indicates differentiation with respect to time t)\*

$$\begin{aligned} M_i [\ddot{q}_i + 2 \rho_i \omega_i \dot{q}_i + \omega_i^2 q_i] \\ = Q_i(t) = \int \int_{fin} \Delta p(x,z,t) \phi_i(x,z) dx dz, \end{aligned} \quad (2)$$

where

$$M_i = \int \int_{fin} m(x,z) \phi_i^2(x,z) dx dz, \quad (3)$$

$\rho_i = i^{\text{th}}$  structural damping ratio,

$\omega_i = i^{\text{th}}$  natural frequency (undamped), and

$m(x,z) =$  mass per unit surface area.

In the chosen system of units, the  $\phi_i(x,z)$  are normalized in such a way that each modal generalized mass  $M_i = 1$ .  $\Delta p(x,z,t)$  appearing in the last member of Eq. (2) is the instantaneous difference in pressure between the two sides of the fin, positive when a force is exerted in the positive y-direction. It consists

---

\*Note that all terms in Eq. (2) have dimensions of force.

of the sum of contributions from 1.) fin motion itself ("aeroelastic" terms), 2.) aerodynamic controls such as commanded rudder rotation, and 3.) buffeting pressure distributions. It follows that the aerodynamic generalized force exerted on the  $i^{\text{th}}$  mode reads

$$Q_i(t) = Q_{iM}(t) + Q_{iC}(t) + Q_{iD}(t). \quad (4)$$

Detailed forms of these three terms will be discussed below, but it is mentioned that, if other than rudder control is applied,  $Q_{iC}(t)$  may appear differently from the integral in Eq. (2).

In connection with the applications described in Sect. 4, more information will be supplied on the mode shapes, the circular frequencies  $\omega_i$  and their calculation. For lower-frequency modes of structures like those dealt with here, the intrinsic critical damping ratios  $\zeta_i$  tend to be of the order 1-2%. It is a conservative assumption to neglect them in Eqs. (2). This has been done here because the energy dissipation due to aerodynamic forces  $Q_{iM}(t)$  turns out to be substantially larger than the structural contribution.

## 2.2 MOTION-DEPENDENT AERODYNAMICS

Although it is well known that, at high  $\alpha$ , the empennage is exposed to a turbulent flow shielded and partially separated by the wing surface upstream, one finds a consensus among theoretical modelers that the unsteady "aeroelastic" loads due to the modal motions can be adequately approximated with linearized

potential theory (e.g., Chap. 5, Ref. 6). It is believed that these airload calculations can be made more accurate by reducing the effective dynamic pressure (averaged over the surface) to some fraction of full flight dynamic pressure. They have been calculated, for low Mach number and as a function of dimensionless frequency, by means of a program LATIS1. This single-surface adaptation of doublet-lattice theory (Ref. 9) was supplied to RANN, INC. by Mr. L. Hutsell of USAF Flight Dynamics Directorate. For use in modal equations, the output is an  $N \times N$  matrix of complex generalized forces. LATIS1 requires, as inputs, three-dimensional details of the lifting surface and polynomial curve-fits to the natural modes. Here it was necessary for F/A-18 to revise the code so that different polynomials represented the fin and rudder motions. For the F-15, loads were calculated for both fin and stabilator.

The theory requires the modal motions to be simple harmonic at prescribed frequency  $\omega$ . This is, however, exactly the form needed for power-spectral methods of response calculation. Hence one can write

$$Q_{iM}(t) = \bar{Q}_{iM} e^{i\omega t} = q S_F \sum_{j=1}^N \bar{A}_{ij} \bar{q}_j e^{i\omega t} \quad (5)$$

For rudder inputs to the  $i^{\text{th}}$  mode, one writes similarly for each  $i$

$$Q_{iC}(t) \equiv Q_{iR}(t) = q S_F \bar{A}_{iR} e^{i\omega t} \quad (6)$$

In Eqs. (5) and (6)  $q$  is the effective dynamic pressure and  $S_F$

the fin plan area. In Eq. (5)  $\bar{A}_{ij}$  can be seen by reference to Eq. (2) to represent the dimensionless generalized force exerted on the  $i^{\text{th}}$  mode due to oscillatory motion of unit amplitude in mode  $j$ . According to standard practice for linear systems, one uses the complex notation for sinusoidally-varying quantities, with the real part being the quantity of actual physical interest. Thus,

$$\bar{A}_{ij} = A_{ijR} + i A_{ijI} \quad (7)$$

LATIS1 has a special feature which enables calculation of the various contributions  $Q_{iC}(t)$  to generalized forces due to prescribed rudder oscillations. It can, furthermore and as needed, be used for tip vanes and other control devices whose action is aerodynamic.

### 2.3 REDUCTION DUE TO $\alpha$ IN THE EFFECTIVE DYNAMIC PRESSURE

As mentioned above, at high  $\alpha$  one must account, in terms like  $Q_{iM}$  and  $Q_{iC}$ , for partial masking of the free-stream airflow due to parts of the vehicle ahead of the empennage. Unless wholly unjustified complexity is to be introduced into the aerodynamics, this can be accomplished only by some approximate empirical scheme. Here it was decided to estimate an averaged dynamic pressure  $q$  over the surface in question, as a fraction of free-flight  $q_{\infty}$ . Their ratio then depends only on  $\alpha$ . Numerical results based on steady-state measurements of stability derivatives are given in Sect. 4.

#### 2.4 AERODYNAMIC INPUTS DUE TO BUFFETING; RESPONSE BY POWER SPECTRAL METHODS

Essential to the practical analysis of fin buffeting is the assumption that the inputs and outputs to the system described by equations like (1) and (2) are stationary random processes. It is, of course, well known that the most important occurrences are associated with fairly rapid aircraft maneuvers. But the frequencies or inverse time constants with which changes take place in parameters like  $\alpha(t)$  are so small compared with the frequency content of the turbulent shaking that structural life, etc., can be determined by studying a series of time "blocks," for each of which  $\alpha$  and  $q_{\infty}$  are prescribed constants.

During such maneuvers the buffet loads are actually superimposed on slowly time-varying loads due to fin incidence, sideslip and the like. When examining the effectiveness of active control, however, "open-loop" and "closed-loop" results can justifiably be compared without accounting for these "D.C." contributions. It follows that the present investigation can be limited to zero-mean statistics. The next approximation that will be adopted is that quantities of interest have nearly Gaussian probability density functions. For input pressures this is verified by reference to data like Fig. 16 of Ref. 19.

Chapter 11 of Meirovitch (Ref. 10) is a useful source of information on these mathematical processes. Beginning at Sect. 11.8, Ref. 10 explains how power-spectral techniques furnish a

convenient vehicle for analyzing phenomena like buffet, and this is the approach adopted here. As used in this report, the power spectral density (PSD) of such a random time function is the Fourier transform of twice\* its autocorrelation function. The cross-spectral density (CSD) is defined similarly from the cross correlation between two signals. The remarkable efficiency of this methodology can be illustrated by reference to a linear system with single random input and output,  $F(t)$  and  $X(t)$  respectively. Their power spectra are related by (cf. Eq. 11.98, Ref. 10)

$$\text{PSD}(X) = |H_{XF}(i\omega)|^2 \text{PSD}(F), \quad (8)$$

where  $H_{XF}(i\omega)$  is the complex frequency response function (or transfer function) connecting sinusoidal variations of  $F$  and  $X$  at circular frequency  $\omega$ . Equation (8) must be replaced by matrix relations -- still purely algebraic -- when there are multiple inputs and outputs.

Three other points are worth noting in this tutorial introduction. The first is that the mean-square value of any zero-mean signal can be found from

$$\overline{x^2} = \int_0^{\infty} \text{PSD} [x(f)] df, \quad (9)$$

where  $f = \omega/2\pi$  is the frequency in Hz. The second is that only sinusoidal transfer functions are needed when relating inputs and outputs. Thus aerodynamic quantities like those defined in Eqs.

\*Note that Ref. 10 omits the factor 2.



(5) and (6) are "ready-made" for the analysis. The third has to do with the artificiality that results from PSD's being quadratic forms even though the systems under study are linear. Suppose, for example, that PSD(a) stands for the spectrum of an acceleration measured in g's. Let the Fourier transform be made on frequency f. Then the units of PSD(a) turn out to be g<sup>2</sup> per Hz.

As can be seen from Eqs. (2) and (4), the driving "inputs" to the buffeting empennage are the generalized forces  $Q_{iD}(t)$ , which are integrals of the pressure loading  $\Delta p$  due to turbulence and weighted by the respective modal amplitudes  $\phi_i(x,z)$  over the fin. The last part of this subsection and the Appendix A describe how the statistics of  $Q_{iD}(t)$  have been estimated. Irrespective of the details, the final product is an  $N \times N$  matrix  $[S_Q]$  of PSD's and CSD's. For a given  $\alpha$  and flight condition,  $[S_Q]$  might be written

$$[S_Q] \equiv \begin{bmatrix} \text{PSD}(Q_1) & \text{CSD}(Q_1Q_2) & \dots & \dots & \dots \\ \text{CSD}(Q_2Q_1) & \text{PSD}(Q_2) & & & \\ \vdots & & & & \\ \vdots & & & & \text{PSD}(Q_N) \end{bmatrix} \quad (10)$$

The corresponding "output" quantities are the time histories  $q_i(t)$  of modal displacements, from which estimates can be constructed of accelerations, internal loads like bending moments and the associated stresses in the fin structure.

As derived, for example, in Sect. 11.17 of Ref. 10, there is

a matrix  $[S_Q]$  of output spectra similar to Eq. (10). The relation between the two matrices requires solving Eqs. (2) (or equivalent) for an  $N \times N$  set of sinusoidal complex frequency response functions  $H_{ji}$ , each dependent on  $\omega$  or  $f$ . Thus  $H_{24}(i\omega)$  would be found by setting  $Q_4(t)$  equal to the unit oscillation  $e^{i\omega t} = e^{2\pi i f t}$  and the other  $Q_i = 0$ ,  $i \neq 4$ . The second output then becomes

$$q_2(t) \equiv \bar{q}_2 e^{i\omega t} = H_{24}(i\omega) e^{i\omega t} , \quad (11)$$

$\bar{q}_2$  is the complex amplitude containing the magnitude of  $q_2$  and its phase lead relative to  $Q_4$ .

Given the  $N \times N$  matrix of  $H_{ji}$ , the input and output spectra are connected by

$$[S_Q] = [H_{ji}^* (i\omega)][S_Q][H_{ji}(i\omega)]^T . \quad (12)$$

Here the star denotes the conjugate of a complex quantity. Equation (12) can be generalized in an obvious way to unequal numbers of inputs and outputs.

In Section 3 it is shown how the very general analysis above can be simplified -- first by reducing the (open-loop or closed-loop) equations of motion to state vector form and second by adopting approximations for the terms in  $[S_Q]$ . Appendix A explains, for a prescribed flight condition, how the effects of forcing pressures can be handled in detail.

A great deal of attention has been paid to representing these turbulent pressures  $\Delta p$  in the burst vortex region. The PSD's and CSD's of  $\Delta p$  acting on the fin and rudder are known to depend on  $\alpha$  and on effective dynamic pressure  $q_\infty$ . Moreover, there is consensus (see, e.g., Fig. 14, Vol. I, Ref. 11) that there is a direct proportionality of these airloads to  $q_\infty$  at a given  $\alpha$  and zero sideslip, so that PSD/CSD's vary with  $q_\infty^2$ .

In view of the anticipated scaling laws, it was decided to conduct initial studies of each aircraft analyzed at one flight condition. Thus for the F/A-18 this was the the severe  $\alpha = 32^\circ$  and 300 psf dynamic pressure. (This is just an illustrative example here. Other conditions are, of course, introduced when structural life estimation is carried out; see Subsection 4.1.) Based on wind-tunnel measurements reported by McDonnell (Ref. 11) and by Canadian National Research Council (e.g., Ref. 5), a power spectrum was constructed for  $\Delta p$  in the form of an augmented Rayleigh distribution. This depends on a single parameter: reduced frequency based on flight speed  $U_\infty$  and an arbitrary reference length  $b_r$ . The influence of airspeed (or Mach No.) therefore enters through a simple scaling. This is illustrated by Fig. 2, where the PSD of pressure coefficient  $C_p = \Delta p/q_\infty$  is plotted vs.  $b_r f/U_\infty$  at  $\alpha = 32^\circ$ . From measurements in the foregoing references and elsewhere, there is evidence to support the approximation that, although the level and RMS of the pressure spectrum vary from point to point over the fin, its dimensionless

shape at a given  $\alpha$  can be assumed constant.

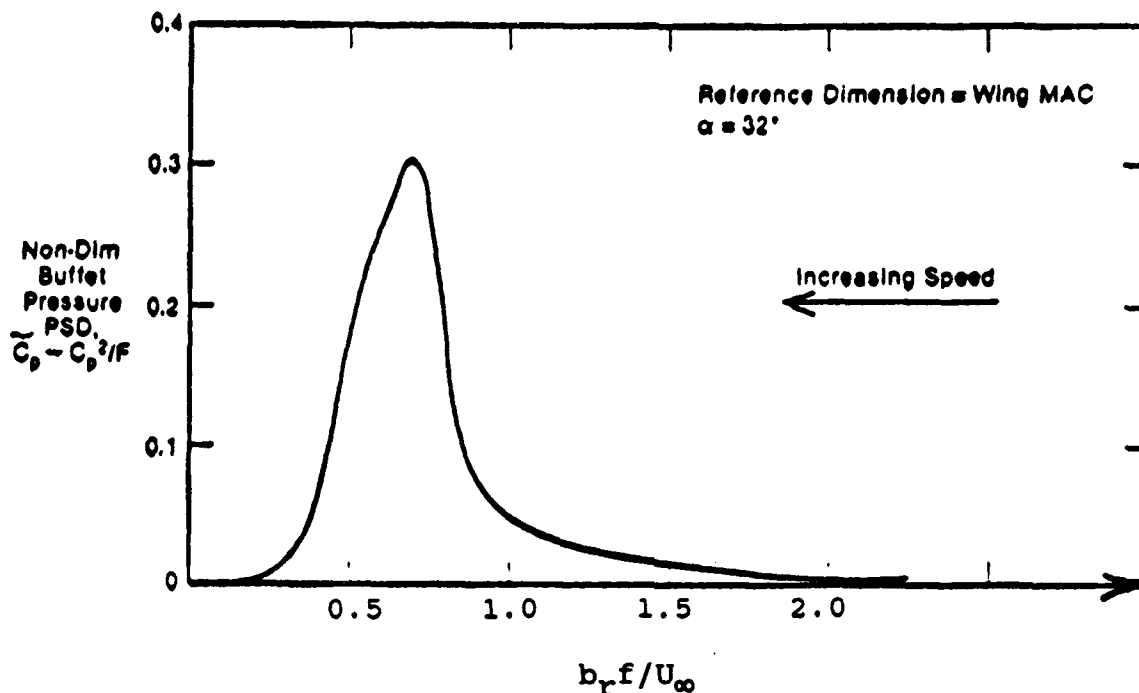


Figure 2. Dimensionless PSD of buffeting pressure at  $\alpha = 32^\circ$  for a typical location on the F/A-18 fin.  $b_r$  is wing mean aerodynamic chord.

One data problem which has been overcome for the CF-18 arises from the fact that the Canadian investigators publish statistics for the absolute pressures on either face but not for  $\Delta p$ . Fortunately, they do provide enough data on resultant normal force to infer a rather high negative correlation between integrated pressures over the two faces. It seems a reasonable approximation to assign the same correlation to local pressures that is known to exist for their surface integrals. Furthermore, the assumption of negative correlation between two sides of the fin is also supported by measurements on an F-15 model (see phase angles on Fig. 201e, Vol. II, Ref. 1).

In Appendix A, the pressure PSD and CSD expressions are derived in general and then reduced to two limiting forms: the first based on an assumption of 100% spatial correlation among the instantaneous  $\Delta p$ 's over the entire surface, the second which presumes that these pressures are uncorrelated as between the fin/rudder stations for which available references supply data. As a matter of interest, working formulas are reproduced here for the members of matrix  $[S_Q]$ , Eq. (10), in the limiting cases. Each involves replacing integrals over the fin-rudder area  $S_F$  by sums over  $M$  small area elements  $\Delta S_k$ , into which  $S_F$  is divided for calculation purposes. Each  $\Delta S_k$  is centered on one of the fin/rudder stations for which  $\Delta p$  spectra are available. Also define a constant  $K_k$  as the ratio of RMS pressure differences

$$K_k = \frac{[\Delta p_{RMS}]_k}{[\Delta p_{RMS}]_{REF}}, \quad (13)$$

where  $[\Delta p_{RMS}]_{REF}$  is the value at a reference location. At this location, the RMS should be relatively large, and the power spectrum of  $\Delta p$  there should be the one chosen as representative of the entire fin (cf. Fig. 2). Finally, with  $F = b_r f / U_\infty$ , let  $PSD_{\Delta C_p}(F)$  be the power spectrum of dimensionless pressure difference at the reference station and at the chosen  $\alpha$ .

When the spatial correlation of  $\Delta p$  is 100%, so that

$$CSD_{k\ell}(F) = q_\infty^2 K_k K_\ell PSD_{\Delta C_p}(F) \quad (14)$$

relates the pressure at station  $k$  to that at station  $\ell$ , one finds for the generalized forces

$$\begin{aligned} \text{CSD}(Q_i Q_j) & \qquad \qquad \qquad (15) \\ & = \alpha_\infty^2 [\text{PSD}_{\Delta C_p}(F)] \left[ \sum_{k=1}^M K_k \Delta S_k \phi_{ik} \right] \left[ \sum_{\ell=1}^M K_\ell \Delta S_\ell \phi_{j\ell} \right] \end{aligned}$$

In Eq. (15),  $\phi_{ik}$  is evidently the displacement of mode  $i$  at station  $k$ , etc. The PSD's or diagonal terms in matrix  $[S_Q]$  are just obtained by setting  $i = j$ .

On the other hand, when there is zero correlation among the various  $\Delta p$ 's, one sets  $\text{CSD}_{k\ell}(F) = 0$  for  $k \neq \ell$ . This leads to the single summation

$$\begin{aligned} \text{CSD}(Q_i Q_j) & \qquad \qquad \qquad (16) \\ & = \alpha_\infty^2 [\text{PSD}_{\Delta C_p}(F)] \sum_{k=1}^M K_k^2 (\Delta S_k)^2 \phi_{ik} \phi_{jk} , \end{aligned}$$

with the obvious reduction when  $i = j$ . The more complicated (and realistic) case of partial spatial correlation is discussed in the Appendix.

### 3.0 STATE-VECTOR FORMULATION AND ACTIVE CONTROL

#### 3.1 PHILOSOPHY OF CONTROL SYSTEM DESIGN

The ultimate aim of intervention by means of active control is to ameliorate all those agents which are responsible for fatigue damage to the empennage. "Fatigue life" of an aircraft is usually defined in terms of the number of hours of typical operation which can be flown before significant damage is encountered anywhere in the structure. The objective is therefore to seek means whereby buffeting response can be alleviated and, if necessary for the vehicle in question, life can be enhanced to a useful degree. Figure 3 is a block diagram illustrating how this might be accomplished by use of a feedback control law. The sensors in this case are one or more accelerometers placed conveniently where the response can be measured -- i.e., the modes become "observable" in the language of control. Other instruments, such as strain gauges, can also serve, but a single accelerometer has proved adequate for most of the present analyses.

For the F/A-18 study it will be seen in Subsection 4.1 that the hydraulically-actuated rudder holds promise as an "effector" to meet the stated objective. Small rotatable vanes attached to the fin's upper structure have also been examined, as have other measures such as piezoelectric actuators (to a limited degree). The position of the effector on the fin is another important issue, since vibration modes which contribute to fatigue damage must be "controllable" from there.

# OVERVIEW OF CONTROL

---

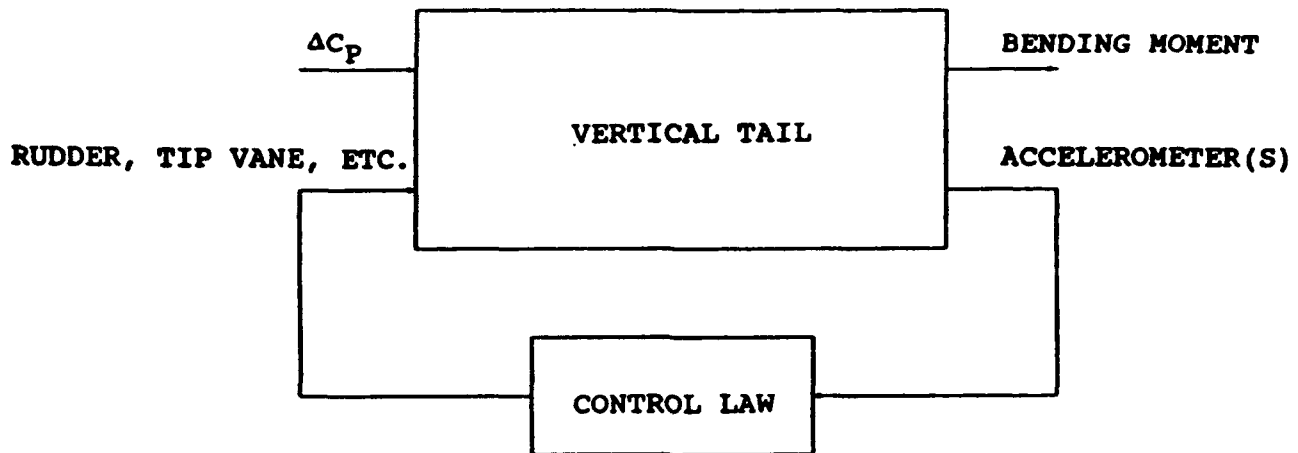


Figure 3. The objective is to use a feedback control law to modify the transfer function from  $\Delta C_p$  to bending moment or some other quantity which measures fatigue damage.

The third tool available to the designer is the control law or "algorithm," whereby sensed signals are processed. Delivered to the rudder, etc., the result of this processing must favorably affect the response. During the research reported herein, it has turned out that single sensors, single effectors and quite simple control laws can do a satisfactory job. This does not, however, imply that improved performance would not be achieved with multiple-element systems and/or more sophisticated algorithms (e.g., "optimal control;" see Ref. 12). What it does imply is that good results can be obtained for the F/A-18 with the simple approach at one flight condition, and that these results might be extendable to the rest of the envelope. Such extensions appear feasi-



ble either by "gain scheduling" or developing adaptive control algorithms, although the latter seems not to be required.

### 3.2 THE STATE-VECTOR FORMULATION

Chapter 6 of Ref. 13 provides an excellent guide to the technique selected for buffet control analysis. For each aircraft the first step is to rewrite the modal equations (2), (4), (5) & (6) symbolically as

$$M_i[\ddot{q}_i + 2\zeta_i\omega_i\dot{q}_i + \omega_i^2q_i] = q_{SF} \sum_{j=1}^N \bar{A}_{ij}q_j + q_{SF}\bar{A}_{iR}\delta_R + Q_{DIST}, \quad (17)$$

The next step is to convert Eq. (17) into a set of coupled first-order ordinary differential equations that can be expressed in standard state-variable matrix form. This was accomplished in several steps. First, it was recognized that the summations appearing on the right hand side of Eq. (17) could be approximated by

$$\bar{A}_{ij}q_j = a_{ij}q_j + b_{ij}\dot{q}_j + c_{ij}\ddot{q}_j \quad (18)$$

$$\bar{A}_{iR}\delta_R = d_{iC}\delta_R + e_{iC}\dot{\delta}_R + f_{iC}\ddot{\delta}_R \quad (19)$$

where the constant coefficients  $a_{ij}$ ,  $b_{ij}$ , etc. were determined by performing a curve fit of the frequency functions  $\bar{A}_{ij}$  and  $\bar{A}_{iR}$  (or  $\bar{A}_{iC}$  for a different control). This is accomplished by a least-squares calculation in the frequency domain.

The second step was to develop a model of the rudder actuator which relates the physical rudder angle  $\delta_R$  and the value  $\delta_{RC}$  commanded by the control law. The latter is an electrical signal driving the hydraulic servo which applies moments about the hingeline. Strictly speaking, this relation should be based on an equation of dynamic torque equilibrium about the hinges, with inertia and aerodynamic terms balancing the applied torque. At the suggestion of the manufacturer, there was adopted for both F/A-18 and F-15 an approximate transfer function constructed from the second-order equation

$$\left[ \frac{d}{dt} + \omega_R \right]^2 \delta_R = \omega_R^2 \delta_{RC} \quad (20)$$

This has the Laplace transformation\*

$$\delta_R(s) / \delta_{RC}(s) = \omega_R^2 / (s + \omega_R)^2, \quad (21)$$

with  $\omega_R \cong 30\pi$  rad/sec (15 Hz) for each aircraft. The value of  $\omega_R$  is determined primarily by compressibility of hydraulic fluid, finite stiffness of the supporting structure and sources of lag in the servo.

The third step is to note that the motion at any location on the fin can be expressed as a linear combination of the generalized coordinates weighted by the mode shapes as

---

\*See Chap. 2 & Appendix A, Ref. 13, for details.

$$y(x_a, z_a, t) = \sum_{i=1}^N q_i(t) \phi_i(x_a, z_a) \quad (22)$$

or for accelerations

$$a = \ddot{y}(x_a, z_a, t) = \sum_{i=1}^N \ddot{q}_i(t) \phi_i(x_a, z_a) \quad (23)$$

Here  $x_a, z_a$  are coordinates of the instrument location.

Finally, Eqs. (17) through (21) and (23) are a set of linear equations that relate the modal displacements,  $q_i$ , velocities,  $\dot{q}_i$ , and accelerations,  $\ddot{q}_i$ , with the actuator quantities  $\delta_R$  and  $\dot{\delta}_R$ . It is straightforward to combine them into the matrix form

$$\dot{x} = Ax + B\delta_R \quad (24)$$

$$\bar{y} = Hx + D\delta_R \quad (25)$$

where

$$x = [q_1, q_2, \dots, q_N, \dot{q}_1, \dot{q}_2, \dots, \dot{q}_N, \delta_R, \dot{\delta}_R]$$

and  $\bar{y}$  is a set of outputs of interest (e.g., displacements, accelerations, bending moments, etc.) that can be expressed as linear combinations of state variables,  $x$ .

When the disturbance term,  $Q_{DIST}$ , is added, the result becomes

$$\dot{\bar{x}} = A\bar{x} + B\delta_R + \Gamma \Delta C_p \quad (26)$$

$$\bar{y} = H\bar{x} + D\delta_R + \Theta \Delta C_p \quad (27)$$

The "distribution matrices"  $\Gamma$  and  $\Theta$  require further discussion since the input pressure loading is known only in power-spectral form. The control system designer sees terms  $\Gamma \Delta C_p$  &  $\Theta \Delta C_p$  as random disturbances which enter Eqs. (26) & (27) linearly. It is helpful if  $\Delta C_p(t)$  can be assumed a single scalar function of time.

The issue of how matrices like  $\Gamma$  are constructed is answered by reference to Eqs. like (15) and (16). The  $N \times N$  matrix called  $[S_Q]$  contains their left-hand sides for  $i, j$  running from 1 to  $N$ . At least in the case of Eq. (15),  $[CSD(Q_i Q_j)]$  consists of a scalar factor  $q_\infty^2$   $[PSD_{\Delta C_p}(F)]$  multiplied by the transpose of a vector times that vector itself. If the vector is called, say,  $[V]$ , then the nonzero terms in  $\Gamma \Delta C_p$  can be associated with terms in

$$[\text{Input Vector}] = q_\infty \sqrt{PSD_{\Delta C_p}(F)} [V] \quad (28)$$

Given the equations defined above, the specific goal of the control law is to feed back a signal to the control input,  $\delta_{RC}$ , that is based on the measured outputs, with the purpose of modifying the effective transfer function from the buffet pressure distribution to the critical system output (bending moment or other quantity of interest). That is, if the transfer function

can be modified, then the spectrum of the output signal that results in response to the stochastic input ( $\Delta C_p$ ) can be reduced. If the transfer function is defined as something such as

$$\frac{\text{Bending Moment}(s)}{\Delta C_p(s)} = H(s) \quad (29)$$

Then the well-known relationship is (cf. Eq. (8))

$$\frac{\text{PSD}(\text{Bending Moment})}{\text{PSD}(\Delta C_p)} = |H(s)|^2 \quad (30)$$

The goal is therefore to reduce the bending moment spectrum and hence to increase the fatigue life by modifying the transfer function  $H(s)$ .

The development and application of candidate, proof-of-concept control laws are presented in Section 4 for the F/A-18 and F15 aircraft.

### 3.3 FATIGUE LIFE ESTIMATION

In order to determine the influence of active control on fatigue life of the fin, a metric or "surrogate" quantity must be found. It is believed that a single scalar can serve present purposes, but very different quantities have been chosen for F-15 and F/A-18. Since more effort has been spent on quantifying these results for the latter aircraft, it will be used as an example. Prior to installation of the LEX fence, composite skin reinforcement and other structural improvements, the F/A-18 fins suffered cracking in the primary Aluminum structure -- especially

near the base attachment to the aft fuselage. Figure 4 was supplied by the manufacturer to illustrate the arrangement of spars and ribs, with the graphite/epoxy skin removed. At their suggestion, the bending moment and resulting stress were selected at the root of spar #7, which lies just ahead of the rudder hinges.

If the fin response is known in terms of the three modal coordinates  $q_i(t)$ , loads/stresses can be calculated by means of the mode-displacement or mode-acceleration methods (e.g., Chap. 10, Ref. 6). For purposes of finite-element structural analysis, an approximation to the F/A-18 mass distribution has been developed in terms of concentrated masses and rotary inertias at discrete locations (cf. Subsection 4.1). One version of the mode-displacement scheme for linear structures (see pp. 471-2, Ref. 14) states that the internal loads are the same as they would be if the system were vibrating freely at the calculated amplitudes as they appear in Eq. (1)..

Quantitatively for bending moment at  $x_v, z_v$ ,

$$M(x_v, z_v, t) = \sum_{i=1}^N A_{Mi}(x_v, z_v) q_i(t), \quad (31)$$

where

$$A_{Mi}(x_v, z_v) = \omega_i^2 \left[ \sum_j z_{vj} M_j \phi_i(x_j, z_j) + \sum_k I_{\theta k} \frac{\partial \phi_i}{\partial z}(x_k, z_k) \right] \quad (32)$$

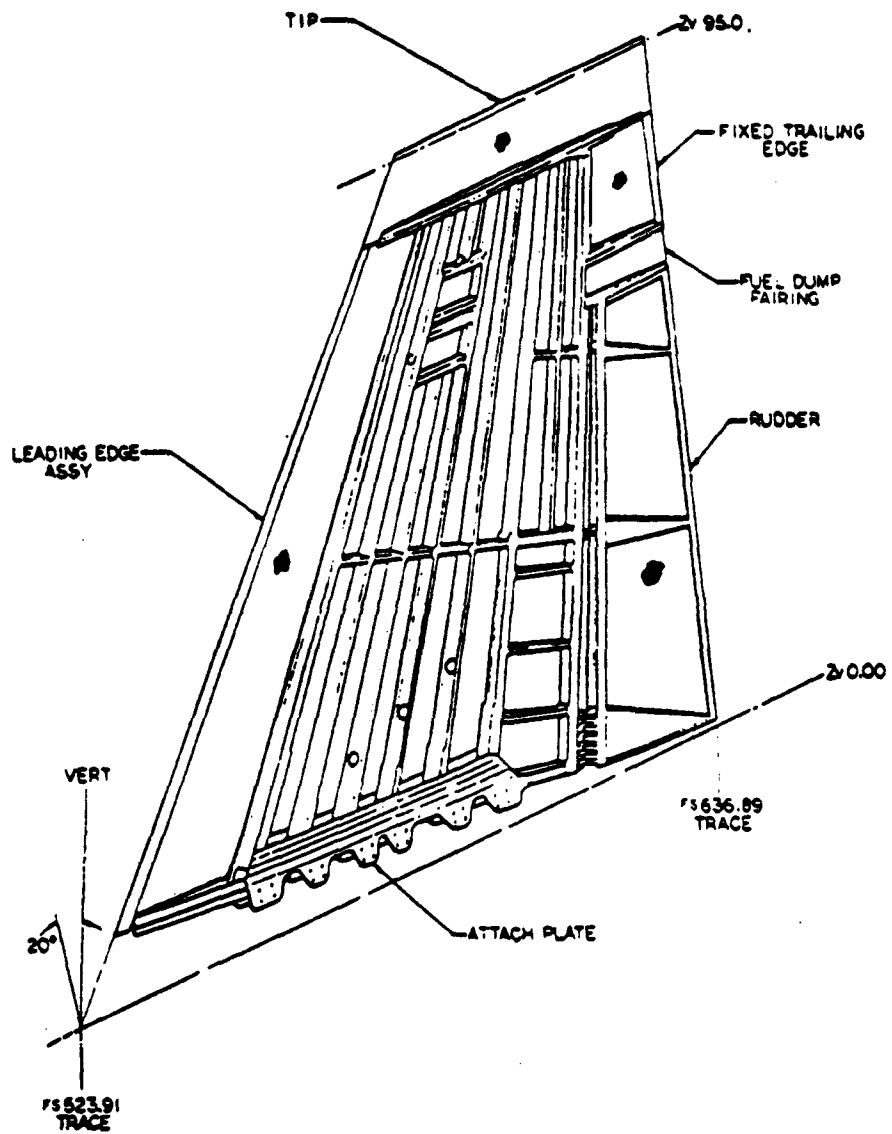


Figure 4. Vertical tail structure of F/A-18 with skin removed.

is the inertia moment about the x-direction per unit amplitude of the  $i^{\text{th}}$  mode. Index  $j$  runs over the locations of all concentrated masses  $M_j$ , and  $z_{vj} = (z_j - z_v)$  is the inertia force's moment arm. Index  $k$  runs over the locations of rotary inertias (about x)  $I_{\theta k}$ , whose inertia couples are proportional to the modal slopes  $\partial\phi_i/\partial z$ .

The actual technique for estimating fatigue life is a highly simplified version of that presented in Ref. 15. It is based on the Palmgren-Miner theory of cumulative damage under cyclic stress (Ref. 16). Subsection 4.1 provides greater detail.



## 4.0 RESULTS OF CONTROL SYSTEM ANALYSIS

### 4.1 THE F/A-18 AIRCRAFT

Figure 5 shows two views of the F/A-18 fin and rudder, with all linear dimensions in inches. The origin of coordinates  $x_v$ ,  $y_v$ ,  $z_v$  is at the root of the leading edge; for the right fin, which is tilted outboard at  $20^\circ$ , these correspond to coordinates  $x$ ,  $y$ ,  $z$  used in Subsection 2.1 and elsewhere. Structurally this is essentially a cantilever from the base, except that the small root flexibility is simulated by connecting the elastic axis (E.A.) to ground with a torsion spring (about the  $x$ -direction) with a constant of  $50 \times 10^6$  in-lb/radian. The E.A. is straight and along the 45%-chordline. Figure 6 is typical of data supplied by the manufacturer, showing the variations of flexural rigidity  $EI$  and torsional rigidity  $GJ$  from root to tip. There are similar data for the rudder, including another torsional spring near  $x_v = 90$  in,  $z_v = 2.35$  in, to reproduce restraint applied by the hydraulic actuator and its backup structure when  $\delta_{RC} = 0$ .

Figure 7 shows the locations of centers of gravity for seven chordwise strips on the fixed fin and four strips along the rudder. For each C.G., there were supplied three equivalent concentrated inertias: a mass, and two rotary moments of inertia about  $x$ - and  $z$ -directions through that C.G.

Based on all the foregoing information, a "stick model" was

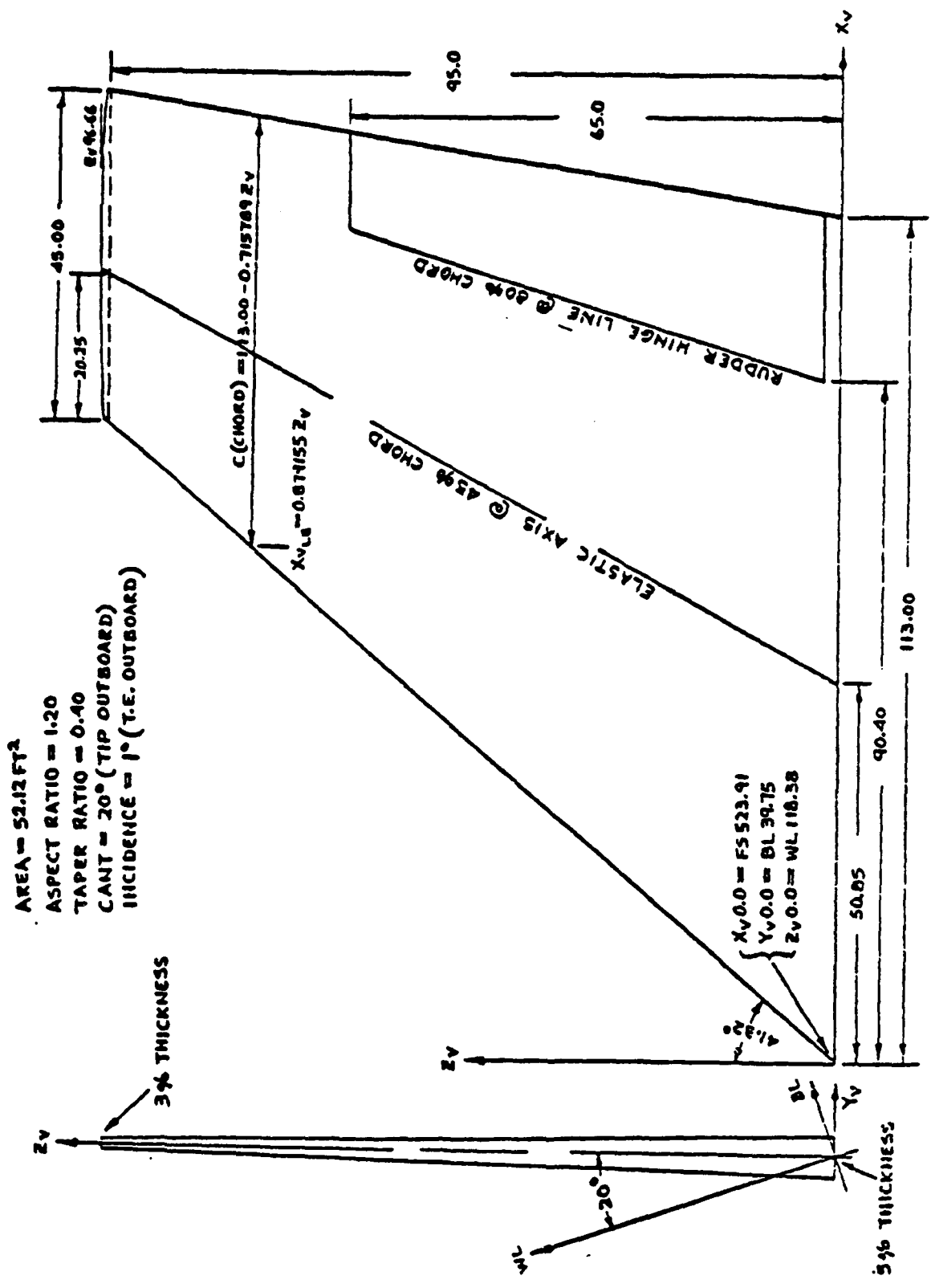


Figure 5. Geometry and dimensions of an F/A-18 fin and rudder.

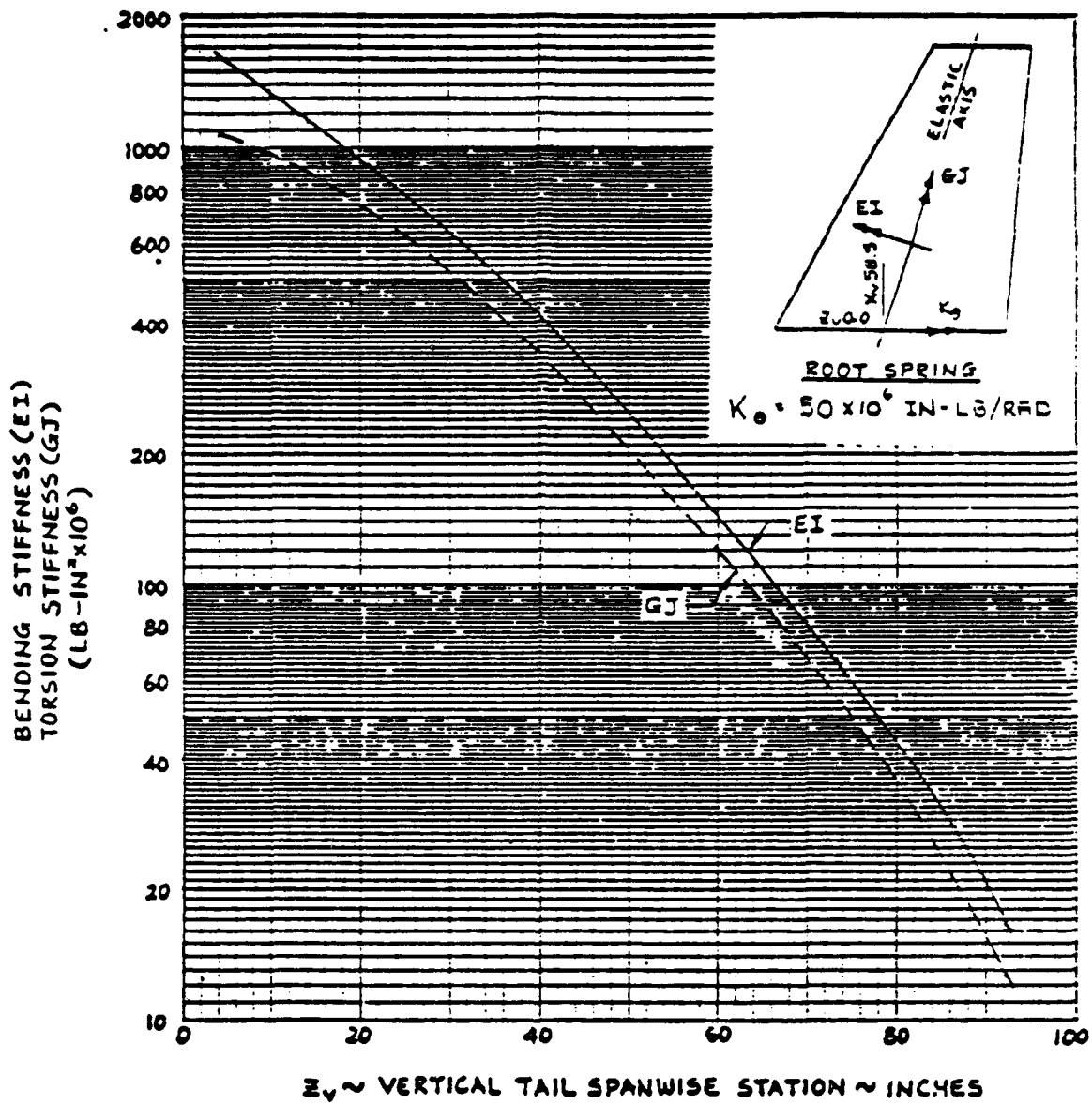


Figure 6. Distributions of flexural and torsional stiffnesses along the E.A. of fixed portion of an F/A-18 fin.

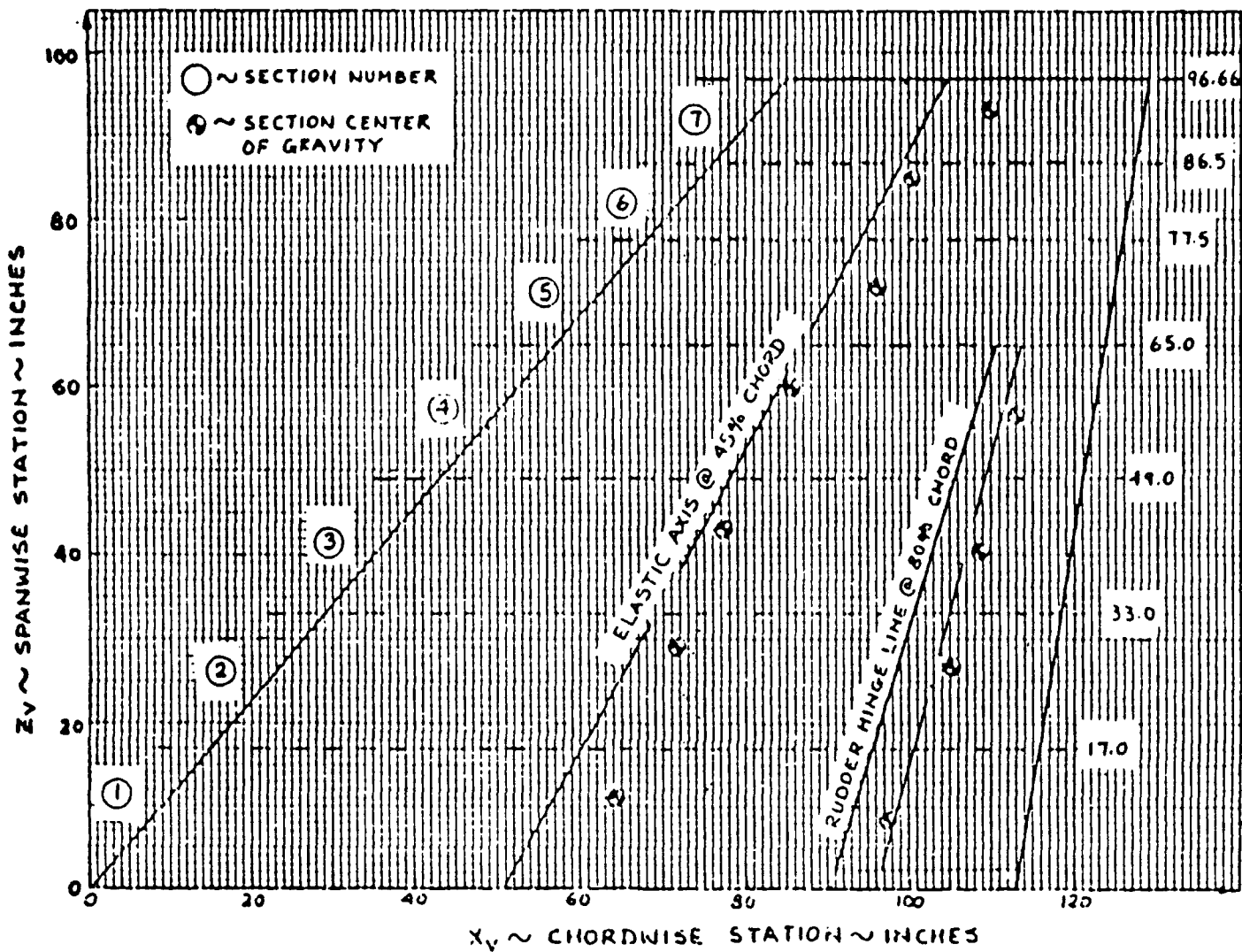


Figure 7. Dimensions and C.G. locations for a sectional approximation to F/A-18 fin and rudder.

constructed by means of the ALGOR finite-element software installed in an HD Systems, Inc., 486DX2 personal computer. There were 40 nodes, doubled in Fig. 8 at six hinge-points along the rudder leading edge. These nodes were connected by beam elements, as illustrated in Fig. 8. Structural stiffnesses were assigned to the elements along the fin E.A. and the rudder hinge-line, which approximates its E.A. fairly closely. Horizontal beam elements were very stiff, simulating the actual chordwise rigidity. Short elements connecting the adjacent fin and rudder nodes were made very flexible to act as hinges, except for the bottom pair which carried the actuator stiffness. Concentrated masses and rotary inertias were placed at each circled node so as

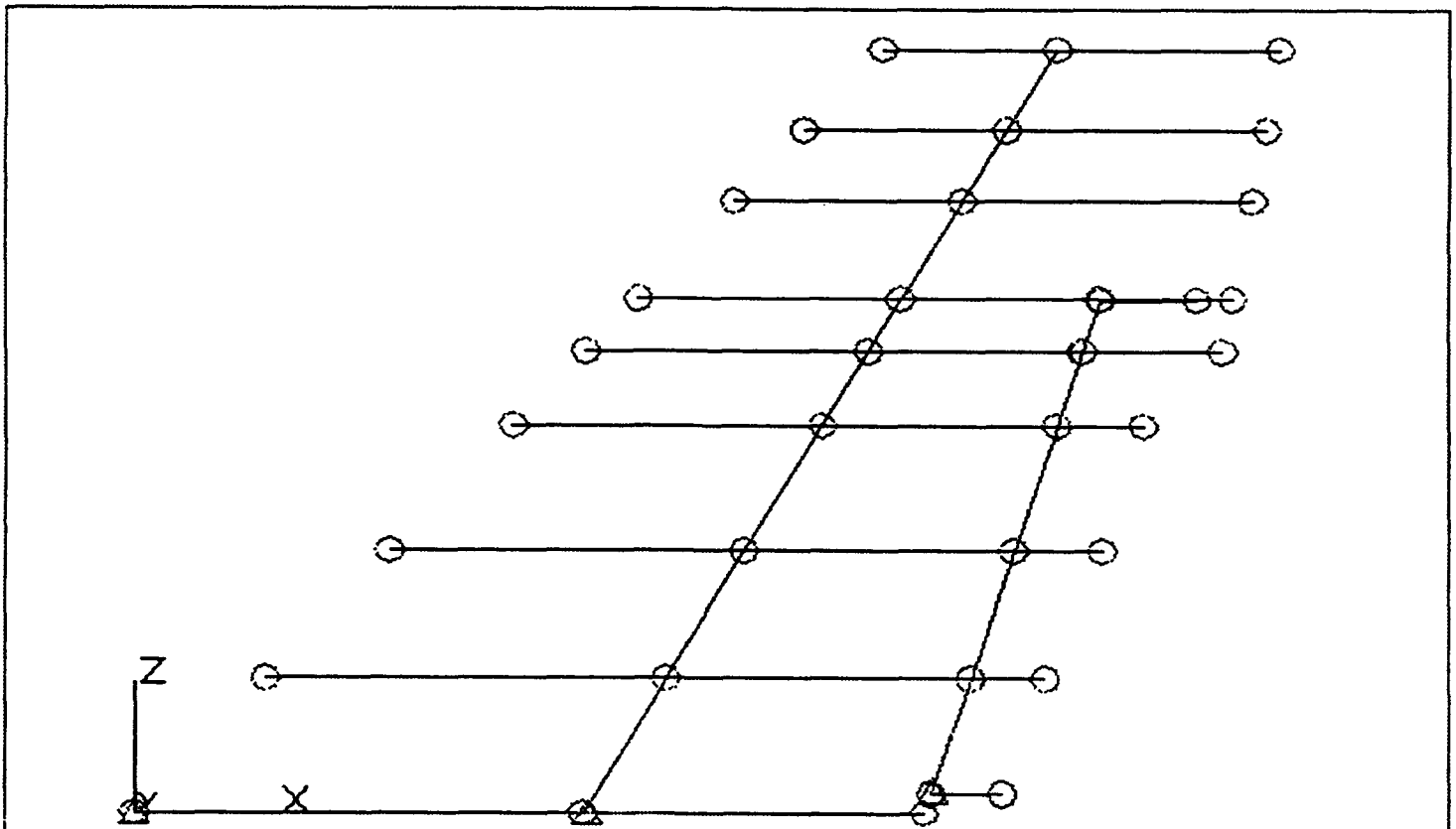


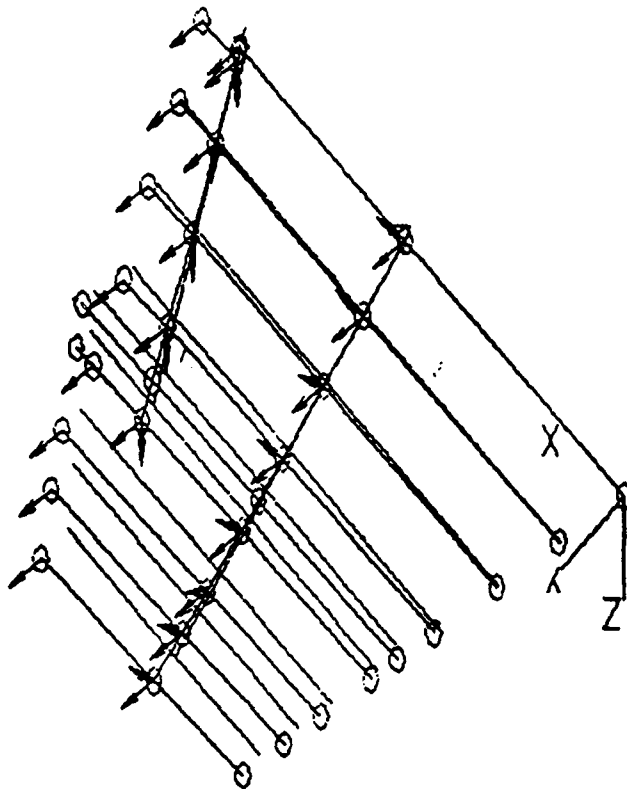
Figure 8. Nodes and beam elements for the ALGOR model approximating an F/A-18 fin and rudder.

to replicate accurately the data associated with Fig. 7. All beam elements were therefore massless.

ALGOR was then used to calculate the first four natural frequencies and mode shapes of the fin-rudder. By reducing the given fin-root spring stiffness from  $50 \times 10^6$  to  $31 \times 10^6$  in-lb/radian, it proved possible to "tune" the fundamental (first bending) frequency close to the given 16.73 Hz. The second and third frequencies of 48.66 and 52.12 Hz were then regarded as near enough to McDonnell's measured values of 46.77 and 49.16 Hz, especially since the corresponding mode shapes agree well with those supplied. The three aforementioned modes form the basis of inertia-elastic terms in the modal equations of motion.

Figures 9a, b, c, d illustrate these three and the fourth predicted modes in order of ascending frequency  $f$  Hz. Each graphic depicts the undeformed "stick" idealization adjacent to its position at maximum amplitude, with small ovals marking the finite-element nodes in the latter case. Arrows appear only at those nodes where non-zero masses and rotary inertias were placed, the length of each arrow being roughly proportional to the associated inertia force or torque. Clearly Mode 1 is primarily bending or flexure, whereas Mode 2 displays both torsion & flexure and Mode 3 has large rotation of the rudder, restrained by the stiffness of actuator and backup structure. As it appears in differential equations like (2), each generalized mass  $M_i$  is made equal to one unit by ALGOR's normalization of the eigenvalue calculation. Since all data are supplied in pounds of force and

9 a).  $f_1$  = 16.74 Hz.  
 $f_{1exp.}$  = 16.73 Hz.



9 b).  $f_2$  = 48.66 Hz.  
 $f_{2exp.}$  = 46.77 Hz.

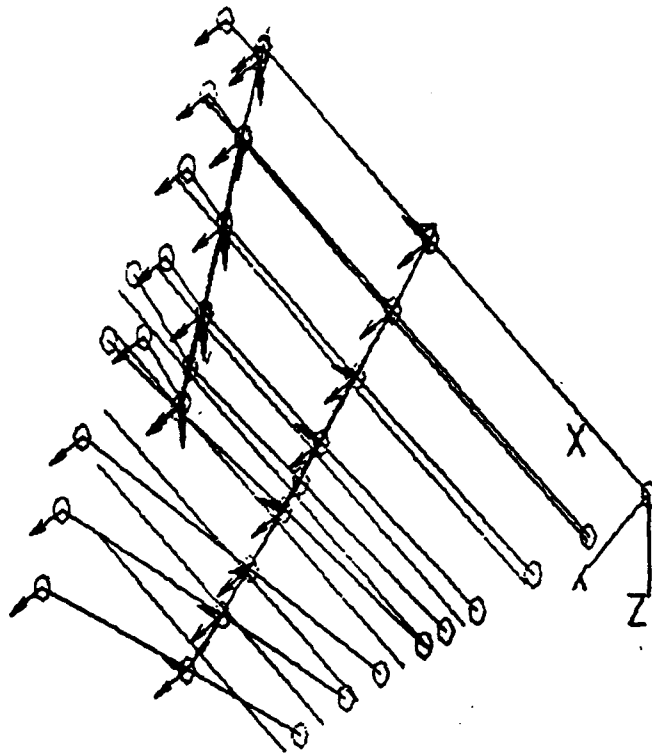


Figure 9. Three-quarter views of the four lowest-frequency natural modes of the F/A-18 fin/rudder. Circles identify nodes in the deflected positions. Each part compares the predicted frequency with laboratory measurement.

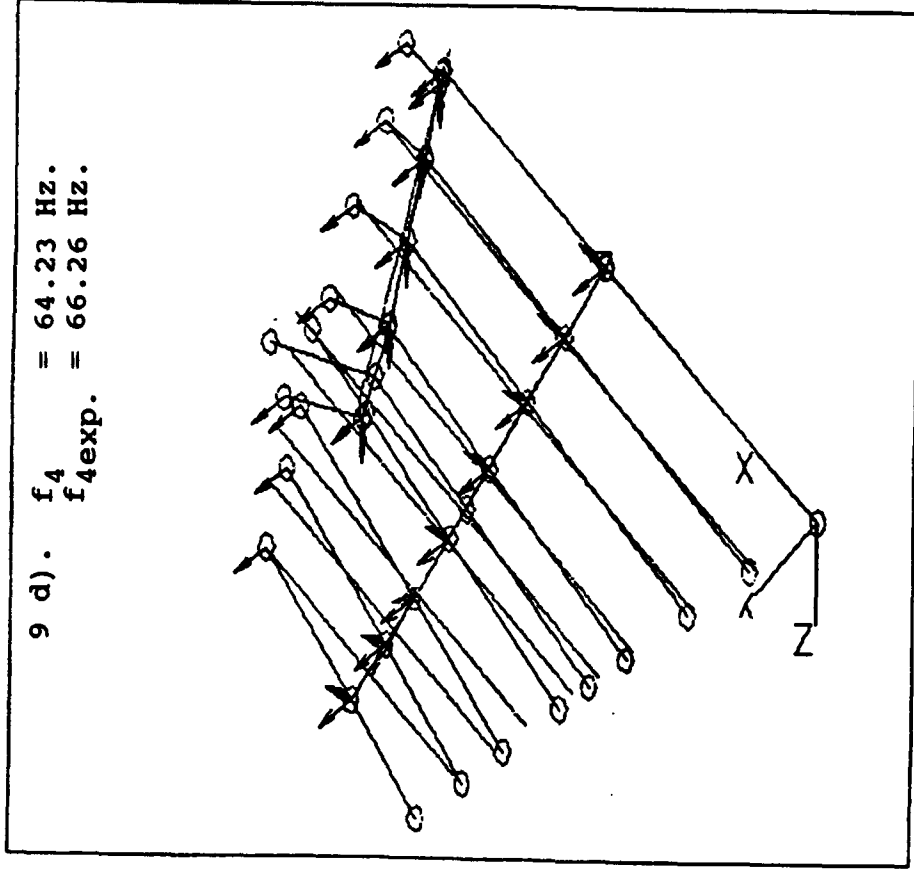
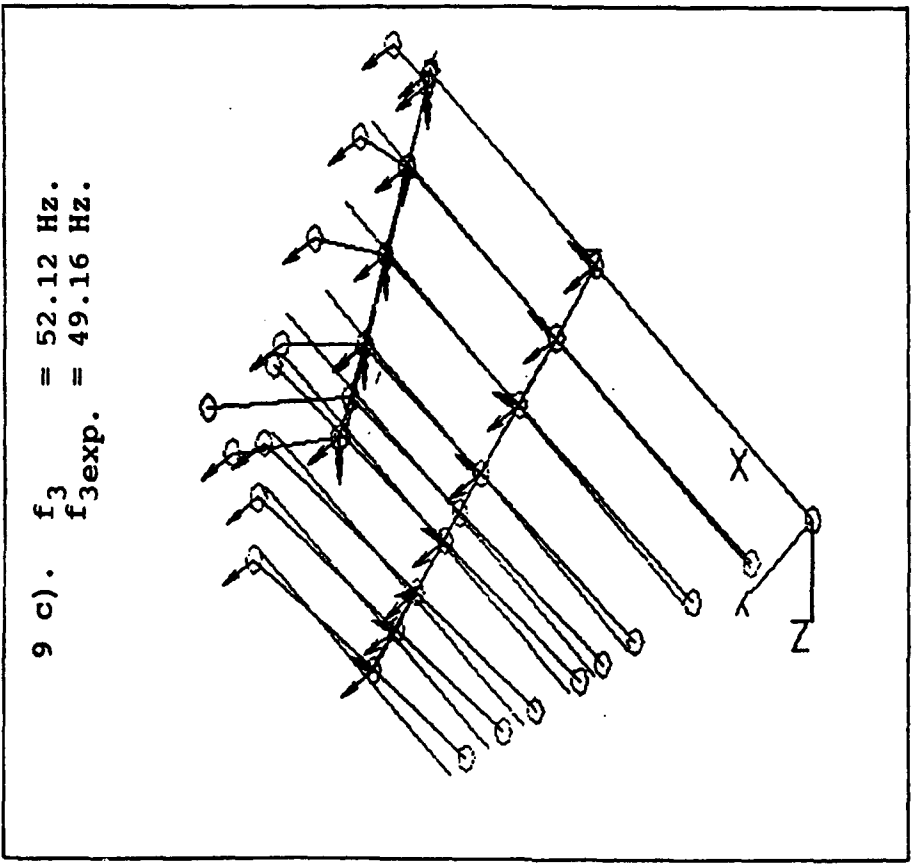


Figure 9, contd.



inches, it is convenient for dynamic purposes to use mass in 12x slugs (386 lbm).

It should be mentioned that, even for the fundamental, experimental frequencies and mode shapes from various sources can differ by 10% or more. Accordingly, one believes that the precision of the ALGOR calculations is more than satisfactory for the purposes of this effort.

For  $N = 3$ , the aerodynamic coefficients  $\bar{A}_{ij}$  of Eq. (5) were computed by the doublet-lattice program LATIS1, as discussed in Subsection 2.2. Figure 10 depicts the pattern of trapezoidal

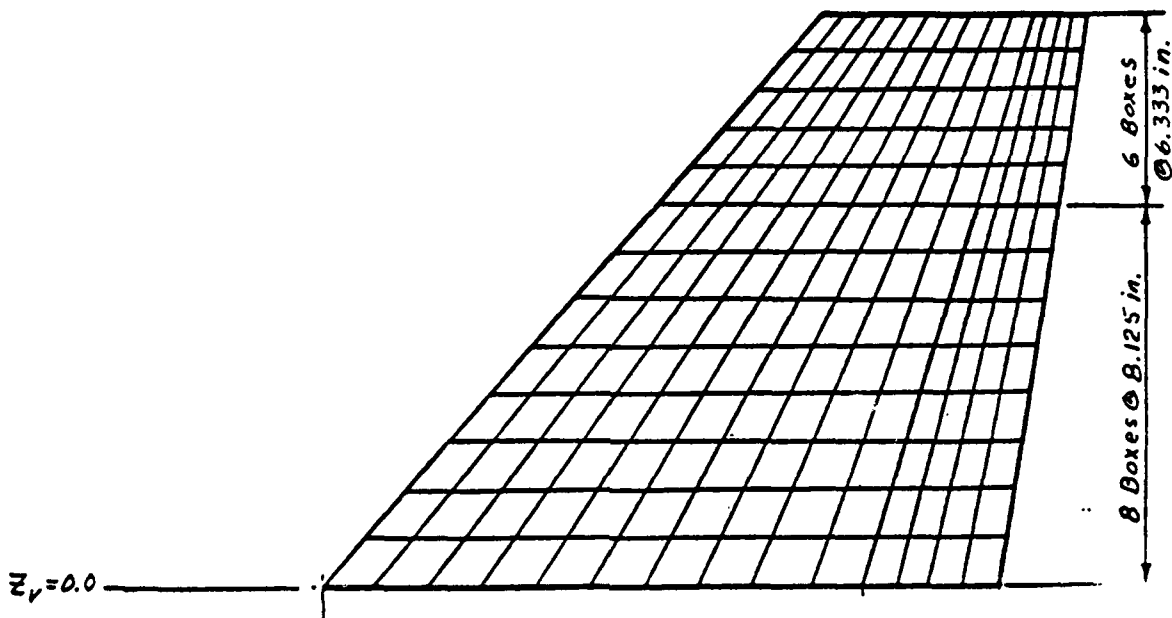


Figure 10. Trapezoidal area elements used by LATIS1 in calculating air loads on F/A-18 fin & rudder.

area elements on whose quarter-chordlines the program places concentrated vortices. For use in modal equations, the product is a  $3 \times 3$  matrix of complex generalized forces. LATIS1 requires, as inputs, polynomial curve-fits to the natural modes, although it was necessary to revise the code so that different polynomials represented the fin and rudder motions. Each dimensionless  $\bar{A}_{ij}$  is a function of reduced frequency (or Strouhal No.)  $fb_r/U_\infty$  and Mach number, the latter parameter being set close to zero.

Zero-frequency comparisons were made between LATIS1 predictions and other data for the fin lift-curve slope and aerodynamic center location. Agreement was within experimental accuracy. LATIS1 was also adapted to calculate the various contributions  $\bar{A}_{iR}$  in Eq. (6) to generalized forces due to prescribed rudder oscillations. Figures 11 and 12 show typical results, along with (dashed) curve-fits needed for state-vector analysis at a particular flight condition (cf. Eqs. (18) & (19)). The process is regarded as generally very accurate.

The problem of reduction in effective dynamic pressure due to large  $\alpha$  was discussed briefly in Subsection 2.3. For F/A-18, this was first estimated from HARV flight-test data. Figure 13 reproduces a plot of the  $\alpha$ -influence on an important control derivative -- yawing moment coefficient per unit rudder angle. If values of  $q/q_\infty$  are taken equal to the ratio of this derivative to its value at  $\alpha = 0^\circ$ , there is seen to be a reduction of more than 50% in the significant range  $\alpha = 25-40^\circ$ . Although other unpublished evidence suggests that the effect is probably not

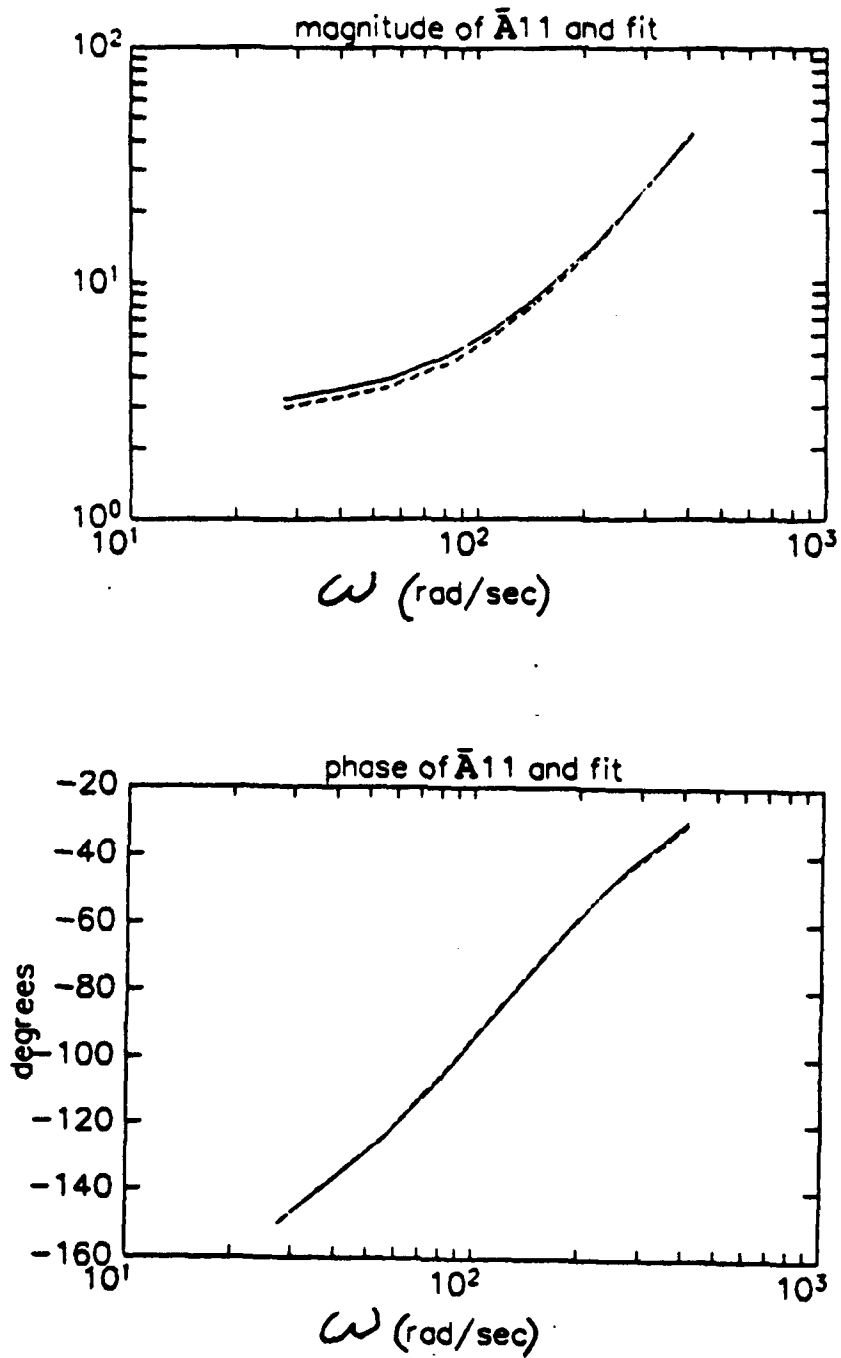


Figure 11. Curve-fit to the aerodynamic coefficient  $\bar{A}_{11}$  for F/A-18 fin in form of Eq. (18).

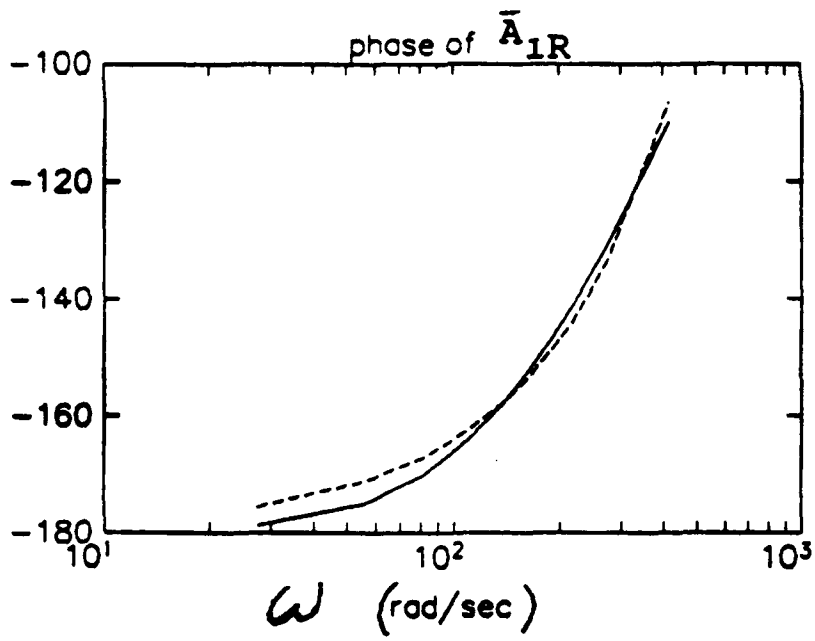
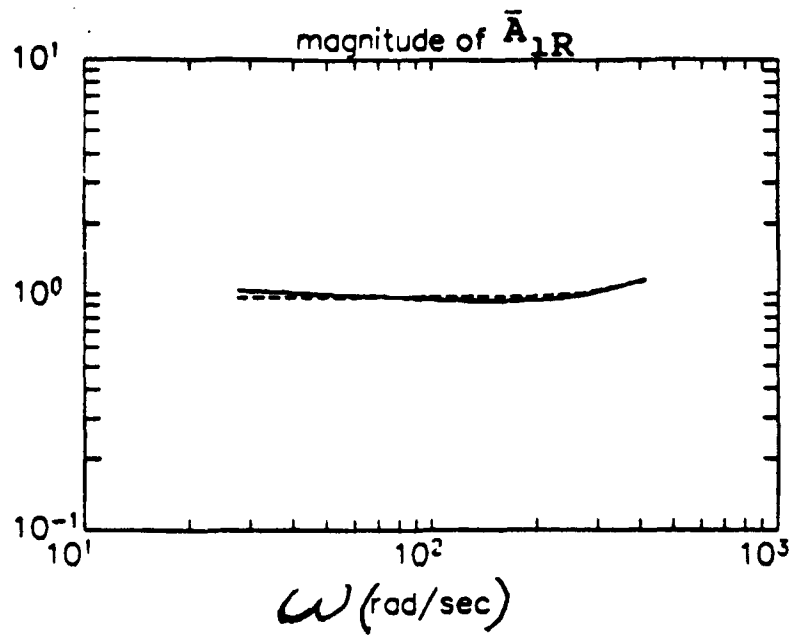


Figure 12. Curve-fit to the aerodynamic coefficient  $\bar{A}_{1R}$  for F/A-18 fin in form of Eq. (19) with  $u = \delta_R$ .

this large, reductions in  $q$  based on Fig. 13 were used during the control investigation. The same corrections apply both open-loop and closed-loop, however, so that calculated effects of active control are not significantly compromised.

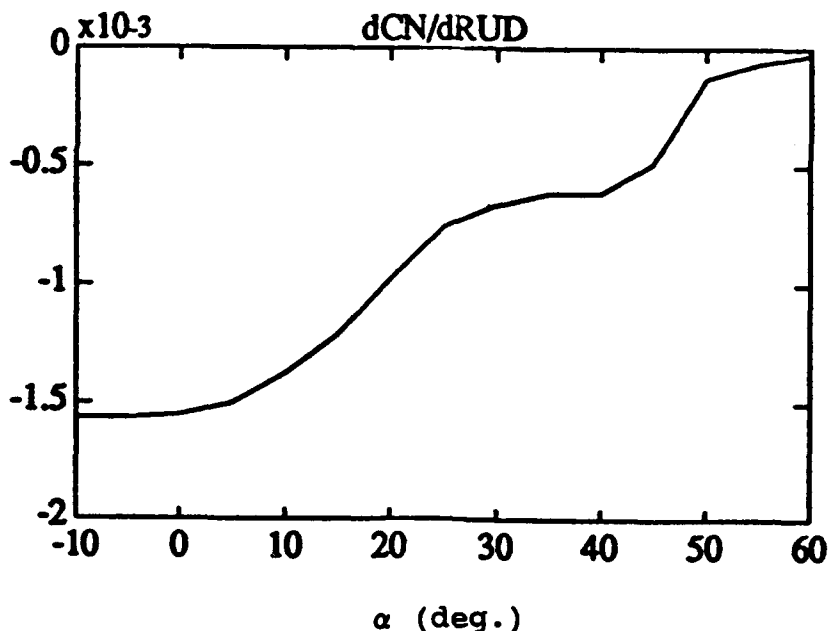


Figure 13. Effect of angle of attack on the yawing moment derivative  $dC_N/d\delta$  due to rudder, as measured in flight on the High- $\alpha$  Research Vehicle.

As discussed in Subsection 2.4, the PSD's and CSD's of buffet pressure loading on the F/A-18 fin/rudder, being quadratic functions, are directly proportional to  $q_\infty^2$ . In view of this scaling law, it was decided to conduct initial studies at one flight condition: the severe  $\alpha = 32^\circ$  and 300 psf dynamic pressure. Other conditions are introduced below when structural life estimation is carried out. To repeat the previous discussion, based on wind-tunnel measurements reported by McDonnell (Ref. 11) and by Canadian National Research Council (e.g., Ref. 5), a power spectrum was constructed for  $\Delta p$  in the form of an augmented

Rayleigh distribution. This depends on a single parameter: reduced frequency based on flight speed  $U_\infty$  and an arbitrary reference length -- actually the wing mean aerodynamic chord, 11.5 ft. Thus the influence of airspeed (or Mach No.) also enters through a simple scaling. The result is illustrated by Fig. 2, where the normalized PSD of pressure coefficient  $C_p = \Delta p/q_\infty$  is plotted vs.  $b_r f/U_\infty$  at  $\alpha = 32^\circ$ .

From measurements in Refs. 11, 17 and elsewhere, there is evidence to support the approximation that, although the level & RMS of the pressure spectrum vary from point to point over the fin, its dimensionless shape at a given  $\alpha$  can be assumed constant. Figure 14, which duplicates Fig. 9, Vol. II, Ref. 11, suggests the accuracy of this assumption and also identifies the data stations used on the McDonnell 12%-scale model. From the same source, for the station at 45%-chord and 60%-span, Fig. 15 shows how the dimensional PSD varies with  $\alpha$ . From RMS levels quoted on Fig. 15 one can see why  $\alpha = 32^\circ$  was selected as being representative of the most severe flight conditions.

For the F/A-18 analysis, the step from pressure spectra to input generalized forces was carried out under the assumption of 100% spatial correlation among the loadings at various fin stations. Hence Eq. (15) of Subsection 2.4 is the required formulation. Now it is clear from correlation functions and other data plotted in Ref. 5 and elsewhere that the  $\Delta p$ 's are only partially correlated, in both the spanwise and chordwise directions. However, it should again be remarked that the present overideali-

F/A-18 Vertical Tail  
 12% Wind Tunnel Model  
 $U_{\infty} = 81.5 \text{ ft/sec}$   
 $\alpha = 32^{\circ}$

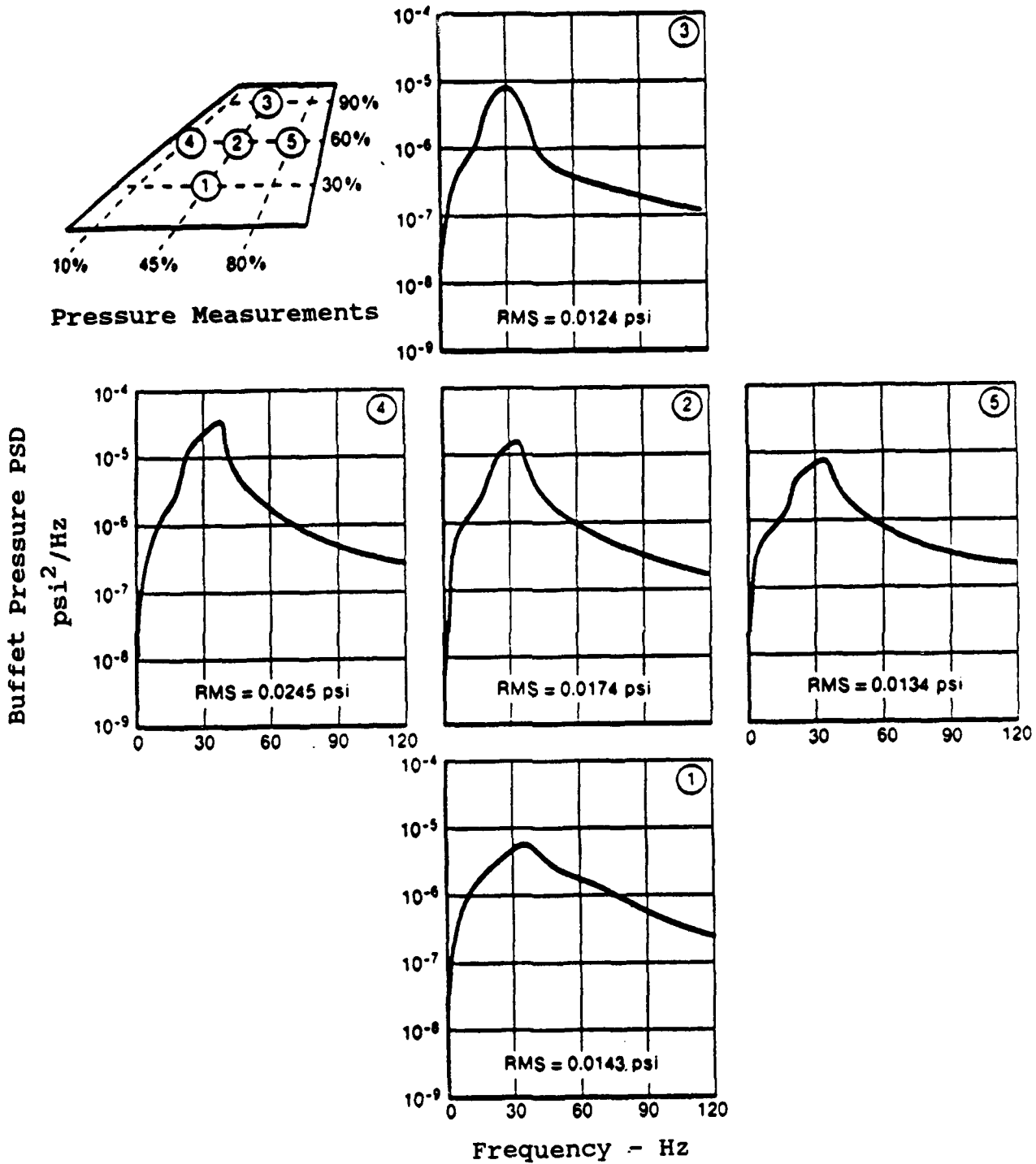


Figure 14. Spatial variation of buffet characteristics at constant air speed, angle-of-attack and density.

F-18 Vertical Tail  
 12% Wind Tunnel Model  
 $U_{\infty} = 81.5 \text{ ft/sec}$   
 $q_{\infty} = 7.5 \text{ psf}$

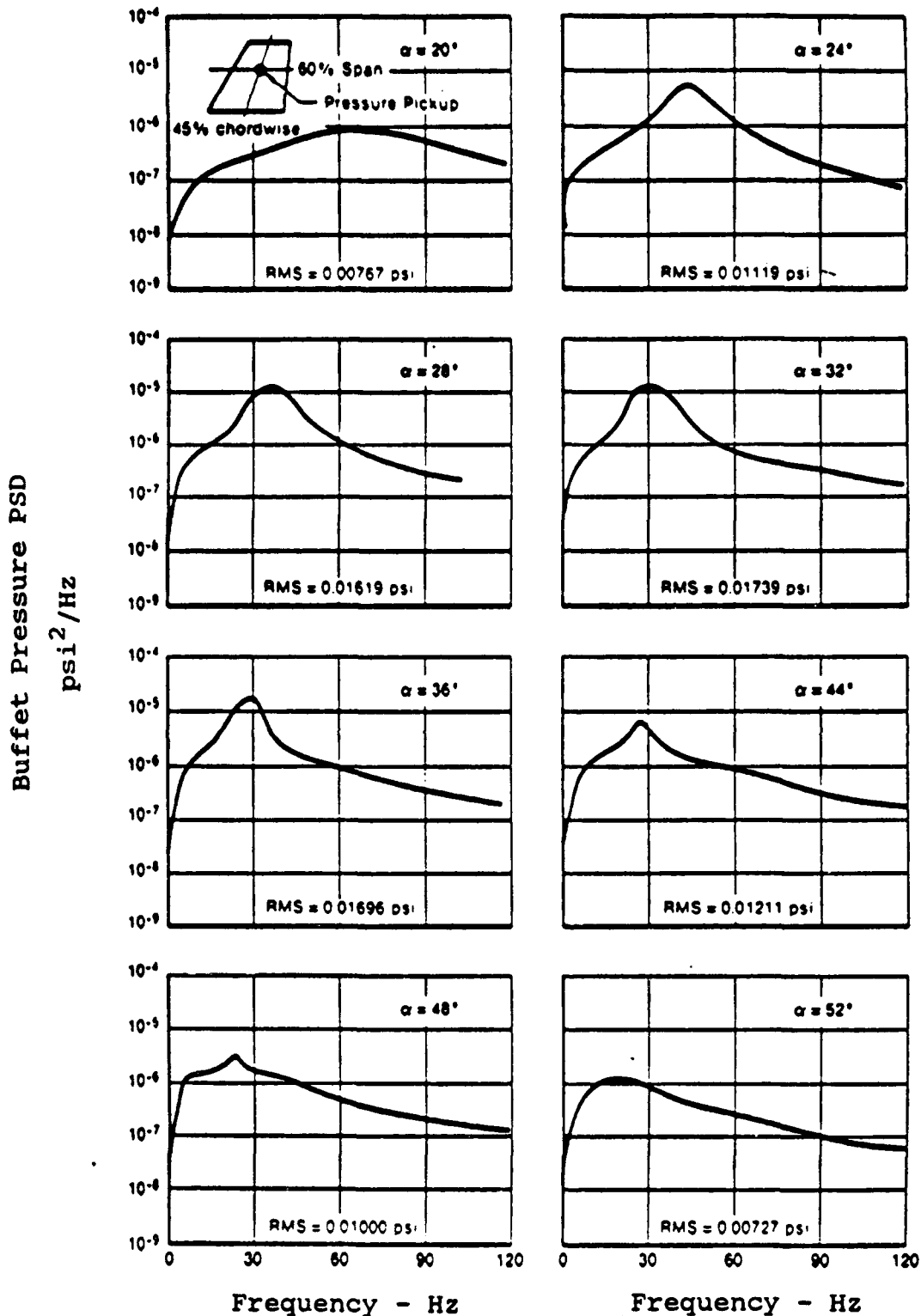


Figure 15. Variation of buffet pressure characteristics with angle-of-attack at constant air speed and density.



zation may not affect the comparison between open-loop and closed-loop response predictions. It is also worth quoting from page 60, Vol. I, Ref. 11: "We then conducted response studies ... considering the buffet PSD<sub>F</sub> and CSD<sub>F</sub>. For our cases, we found the influences of the CSD<sub>F</sub> to be quite small and consequently dropped their use after a few runs." Accordingly, it may matter only a little which limiting case is used.

The actual numerical realization of terms in Eq. (15) was performed with PSD<sub>ΔCp</sub>(F) functions from Fig. 2 for α = 32° and from (nondimensionalized) Fig. 15 at other α's. The factors K<sub>k</sub> were found from RMS pressure data (LEX fence on) for the 24 fin/rudder stations tested in Ref. 5, with the assumption that instantaneous pressures on the two sides were 180° out of phase. For α near 32°, it is of interest to set down typical numerical results:

$$\begin{aligned}
 [S_Q] &\equiv [CSD(Q_i Q_j)] && (34) \\
 &= q_\infty^2 S_F^2 [PSD_{\Delta C_p}(F)][V]^T [V],
 \end{aligned}$$

where

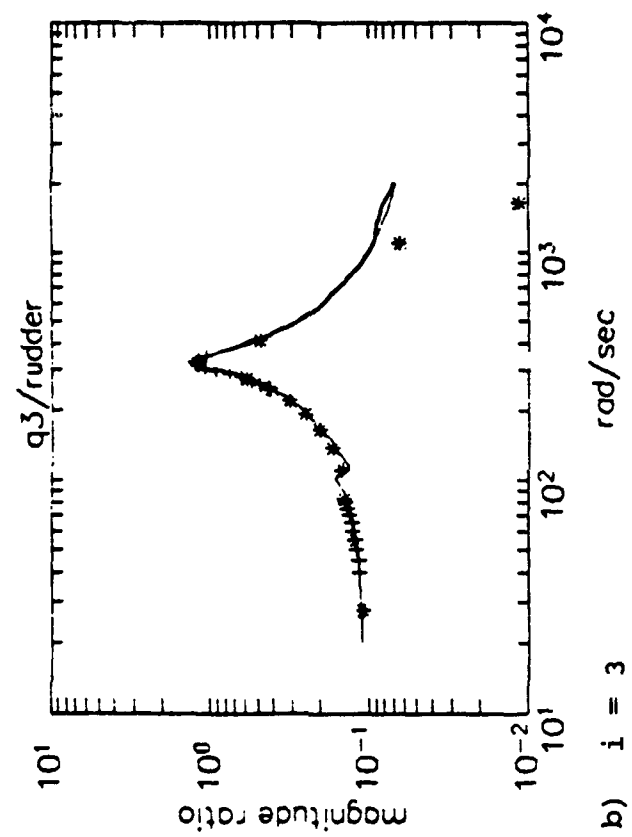
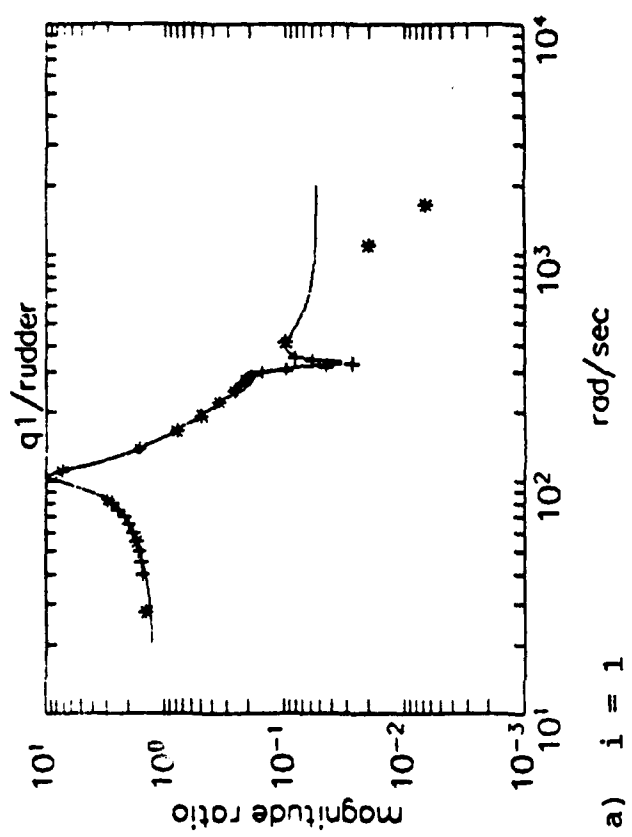
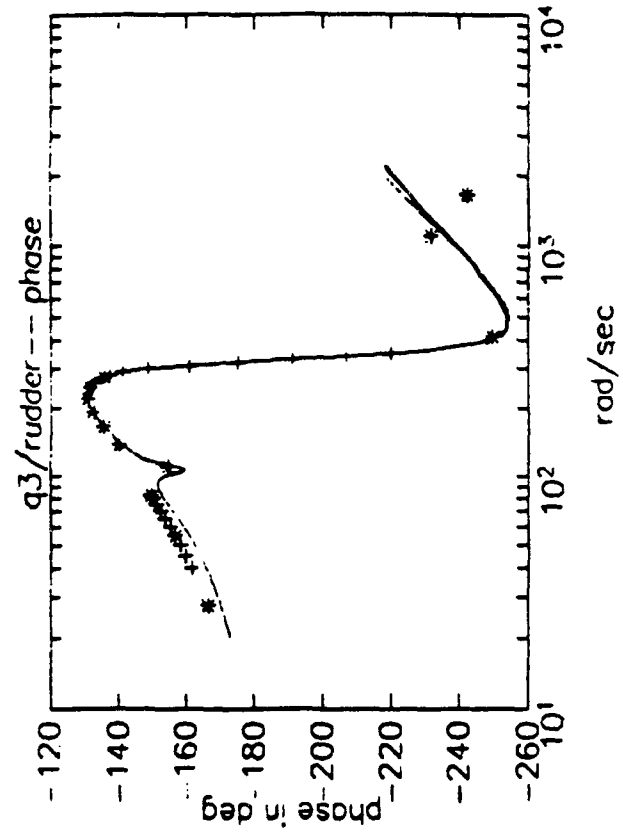
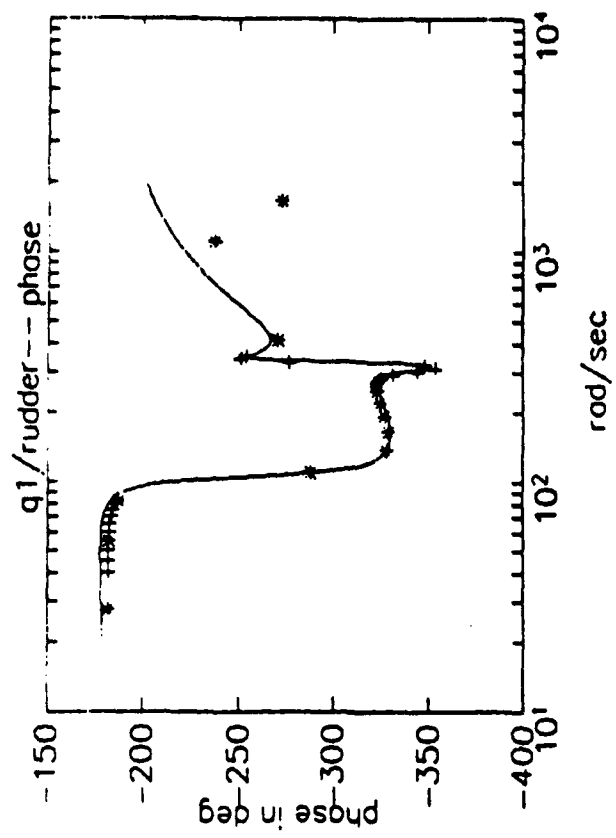
$$[V] = \begin{bmatrix} 0.4886 \\ -0.3653 \\ 0.3194 \end{bmatrix} \quad (35)$$

The foregoing information was assembled and translated into state-vector form as described in Subsection 3.2. Prior to the introduction of active control, various comparisons were made for the purpose of validating the required approximations. Already

in Figs. 11 and 12 was demonstrated the accuracy with which the aerodynamic quantities  $\bar{A}_{ij}$  and  $\bar{A}_{iC} = \bar{A}_{iR}$  can be curve-fit as functions of frequency. More comprehensively, open-loop response calculations were made with the original data, then compared to counterparts in state space. Figures 16 a), b) are a typical example, showing response in the modal coordinates  $q_1(t)$  and  $q_3(t)$  to sinusoidal excitation by rudder-actuator commands. The asterisks give "exact" results, whereas the solid lines are the equivalent approximations. Except at frequencies far above the range of interest, this example and several others achieve a detailed level of agreement which exceeded expectations.

As a final attempt at model validation, Fig. 17 presents the predicted and flight-measured PSD's on a Canadian CF-18 (Ref. 5). The instruments are in identical locations near the right and left fin tips, so that with perfect symmetry the upper solid and dashed curves should coincide. The flight condition -- identified on the figure -- is well below the worst case. But its parameters were incorporated into the analysis embodied in the lower plot. Incidentally, the senior author of Ref. 5 has verified that the units "MAG<sup>2</sup>/Hz" on the upper ordinate are actually g<sup>2</sup>/Hz.

Clearly there are differences between the plots. The predicted 40-50 Hz peak is lower and the 15.9 Hz peak substantially higher than measured. Most of the response "power" exists in these peaks, so that the disagreement in the curve shapes between them is not of great significance. To examine further the degree



a)  $i = 1$

b)  $i = 3$

Figure 16. Dimensionless amplitude and phase angle of transfer function from rudder command  $\delta_{RC}$  to first- and third-mode amplitudes  $q_i$ , plotted vs. input frequency for the reference F/A-18 flight condition.

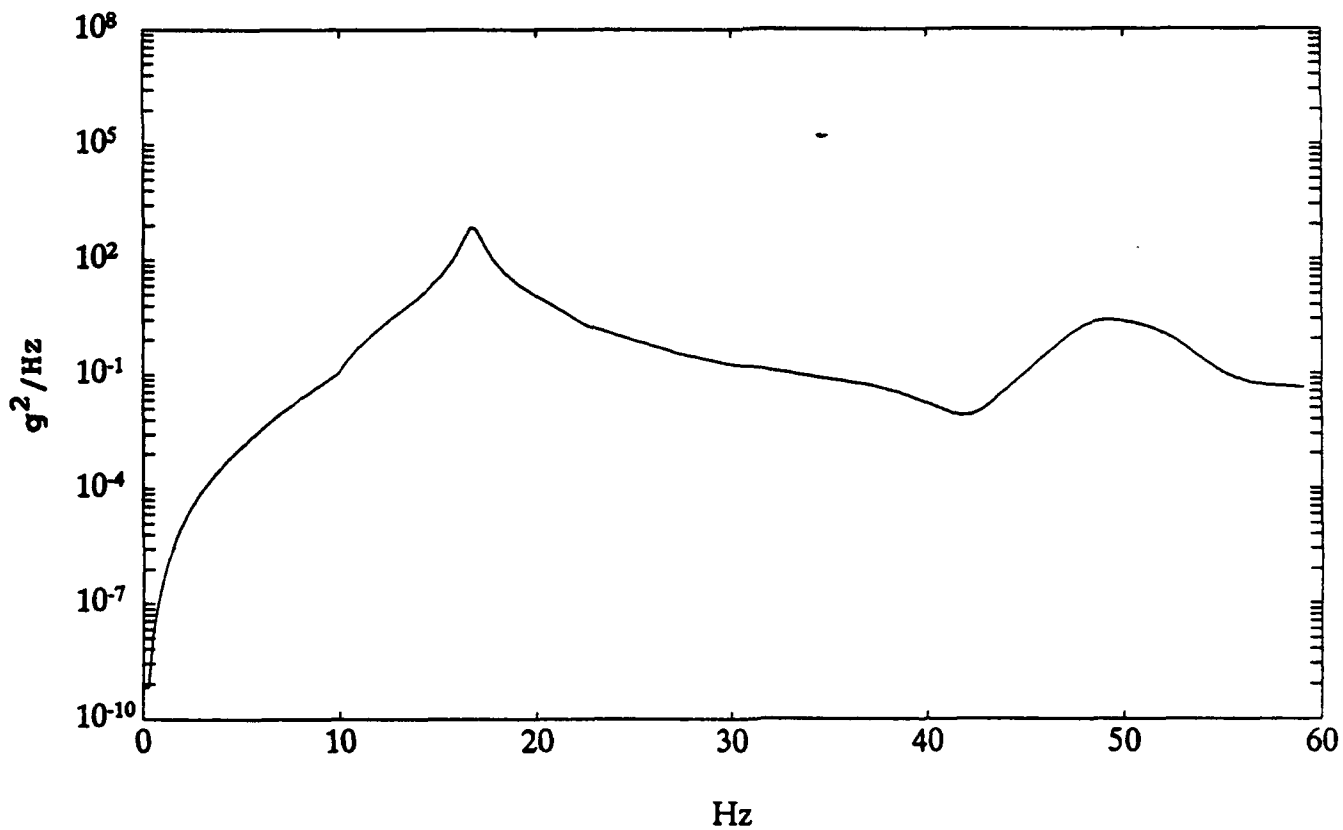
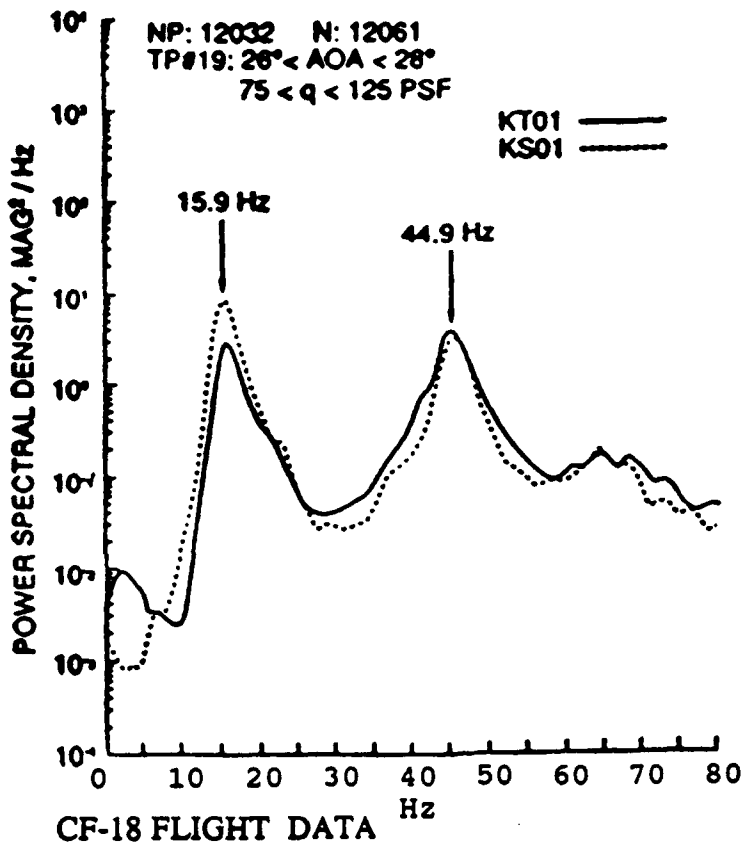


Figure 17. Predicted PSD (lower curve) vs. flight-measured PSD's (upper curves) for acceleration at instruments near the CF-18 fin tips. LEX fence was on. Altitude 10,000 ft.

of comparison, the areas under the three curves have been integrated and RMS accelerations computed. The results are as follows:

Instrument KT01:	5.99 g RMS
Instrument KS02:	7.71 g RMS
Prediction:	29.76 g RMS

These numbers speak for themselves. Although the measured RMS g's in the range 5-8 seem somewhat low when set against the accelerometer traces on Figs. 42 and 43 of Ref. 5, the difference is believed accounted for by the lower flight dynamic pressure. The fact that the prediction is so much higher is harder to explain, but at least two factors are involved: the conservative assumption that the buffeting pressures are 100% correlated and the neglect of structural damping in the presence of a strong resonance near 16 Hz.

The research on active control of this fighter focussed on the rudder as the "effector." An early attempt to use a small vane extending above the fin tip was abandoned. It turns out that such a device would be unacceptable because of already close clearances between the fin and elevators on aircraft carriers. As introduced in Subsection 3.3, bending moment and stress at the root of an Aluminum spar served as the "surrogate" for estimating fatigue life.

Various accelerometers located near the fin tip were studied as candidate instruments for response measurement. Not only can these provide high observability of the vibration modes, but similar locations have been employed in both wind-tunnel and flight testing. The instrument finally selected for feedback purposes was designated KS01 in Ref. 5; its position is 10.5 in inboard from the tip and 10.93 in aft of the leading edge.

In the first attempt at response reduction, a relatively simple control algorithm was tried which fed back velocity (i.e., the integral of the accelerometer signal) to rudder command  $\delta_{RC}$ , phased so as to provide damping to the structure. When the transfer function of the existing F/A-18 actuator and rudder is incorporated into the "closed loop," such control is relatively ineffective. Thus, with PSD of fin-root bending moment as a surrogate for structural damage accumulation, one calculates that spectral peaks associated with the first two vibration modes are moved to higher frequency but slightly increased in height. By contrast, when a "perfect rudder" without frequency roll-off is hypothesized\*, a dramatic reduction of order 100:1 is applied to the first peak and considerable power is also removed from the second peak and the entire spectrum:

With encouragement from the latter finding, control investigations proceeded to more refined algorithms. After a number of trials, it is believed that the most significant dis-

---

\*This strategy replaces Eqs. (20)-(21) with the identity  $\delta_R = \delta_{RC}$ , which is quite impractical.

covery was that direct feedback of acceleration itself to  $\delta_{RC}$  is much more powerful than velocity for reducing the RMS level of bending moment. This appears to be the case because, in the process of passing signals through the transfer function Eq. (21), phase shifts occur which actually cause the rudder to damp significant modes.

One specific example involving active control at the severe flight condition  $\alpha = 32^\circ$ ,  $q_\infty = 300$  psf, at sea level, is first presented. Figure 18 compares the open-loop PSD of fin-root bending moment (solid curve) with what is produced by acceleration feedback at quite a modest level -- such that the RMS amplitude of rudder displacement  $\delta_R$  was about  $3.2^\circ$ . Although the difference does not appear dramatic, one should note that the ordinate scale is logarithmic and that power is reduced significantly near the "resonance" peaks of the first two modes. It actually turns out that the RMS moment is diminished by 33%. The PSD of rudder angle required in this example is plotted in Fig. 19. Rough estimates of the amount of hydraulic power absorbed in this case and of the effects on structure in the vicinity of the actuator suggest that both are quite limited.

Figures 20 through 22 give the sort of predicted performance one is able to achieve with the same algorithm. The figure captions try to explain what is involved. But in all cases the ordinate is the relative reduction in RMS bending moment achievable as the gain of feedback to the rudder actuator is increased. This gain results, of course, in increasing the RMS level of

bending moment

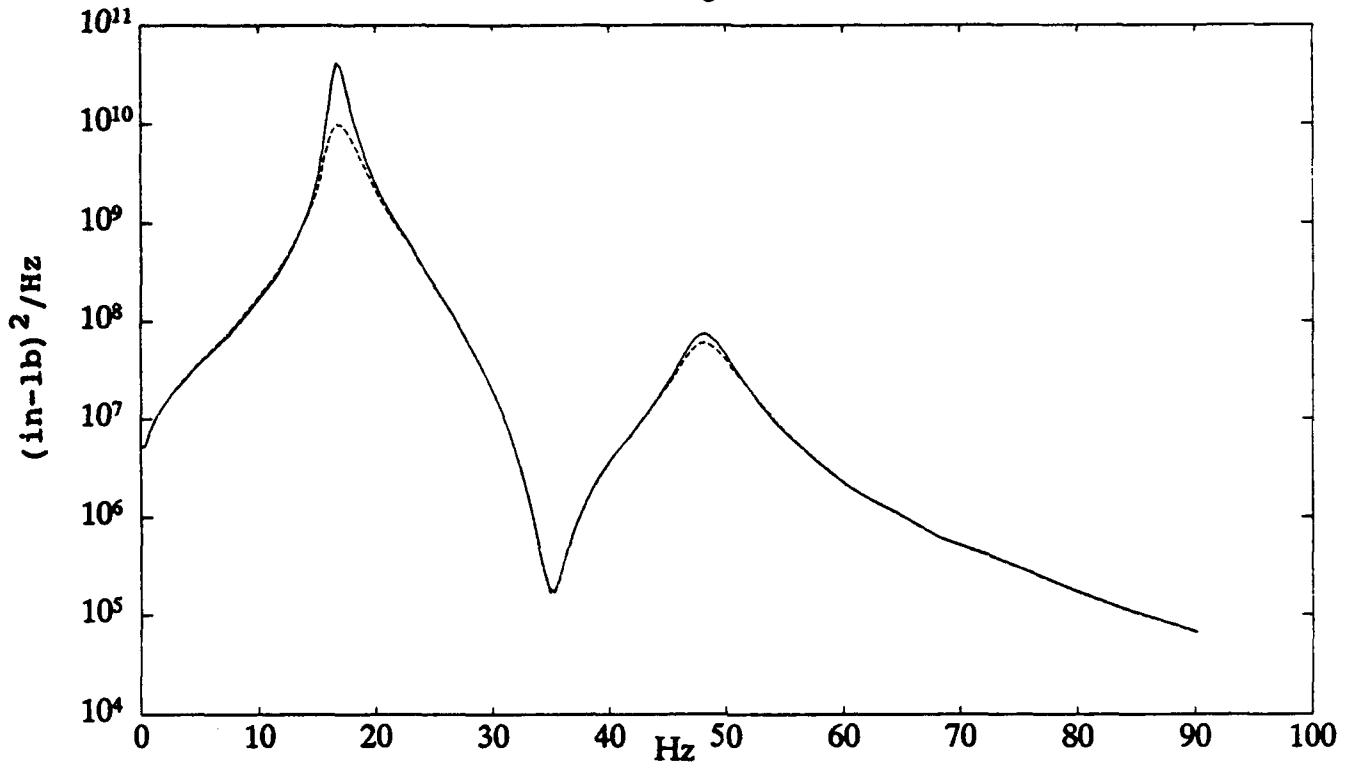


Figure 18. PSD of F/A-18 fin root bending moment due to buffeting at  $\alpha = 32^\circ$ ,  $q_\infty = 300$  psf, sea level. Solid curve is open-loop; dashed curve for fin-tip acceleration feedback to cause  $\text{RMS } \delta_R \approx 3.2^\circ$ .

rudder PSD (RMS=3.2deg)

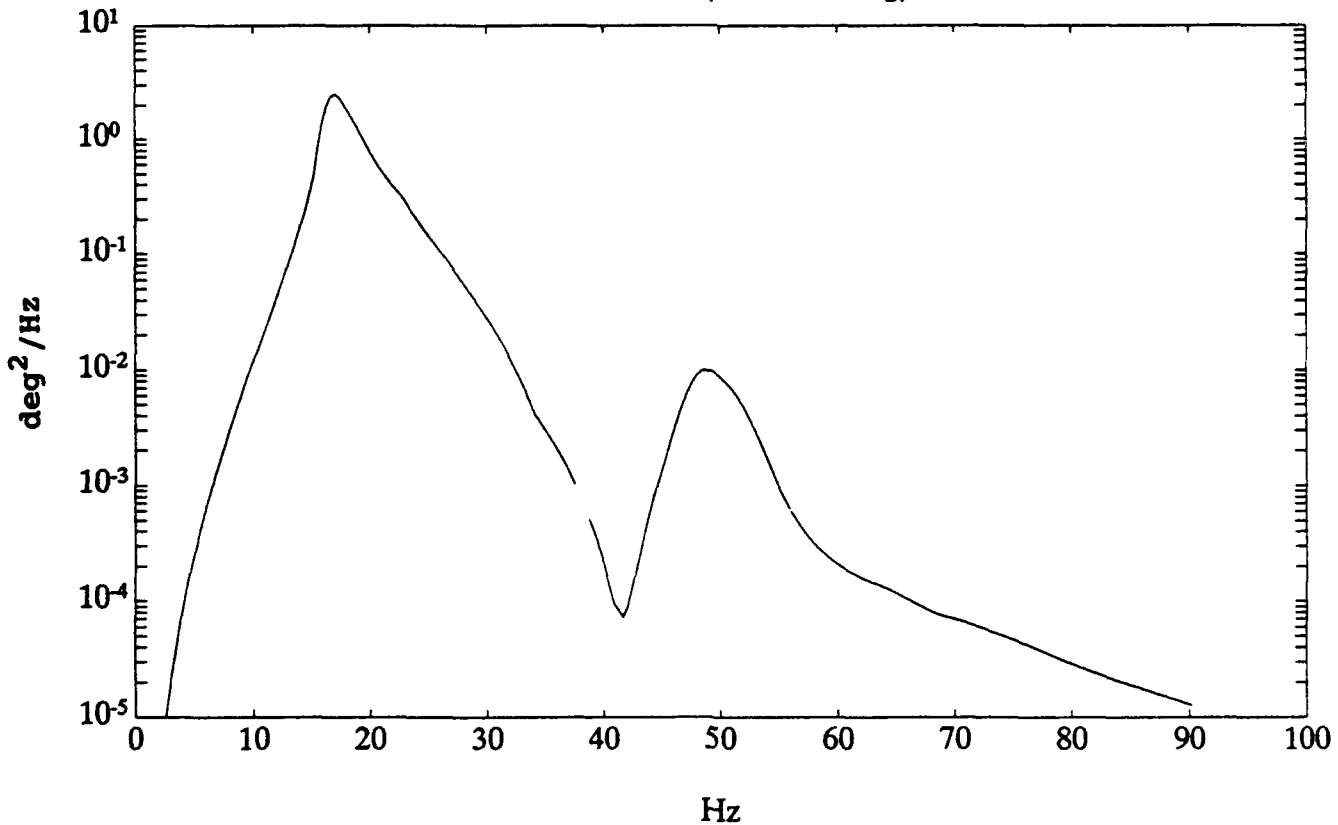


Figure 19. PSD of rudder angle required to reduce RMS fin-root bending moment by 33%.



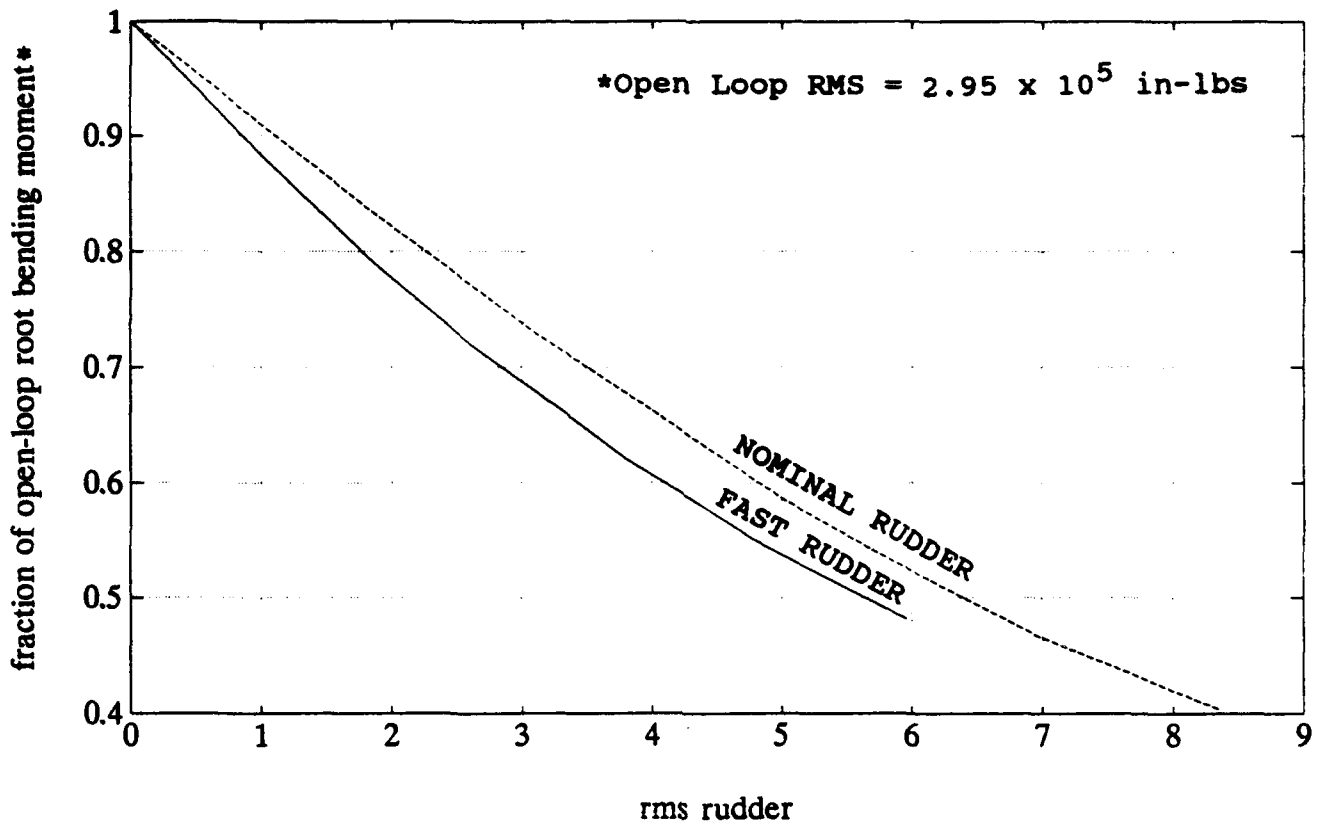


Figure 20. Effect of increasing RMS rudder displacement in degrees on relative RMS bending moment at root of F/A-18. (Same flight condition as Fig. 18.)

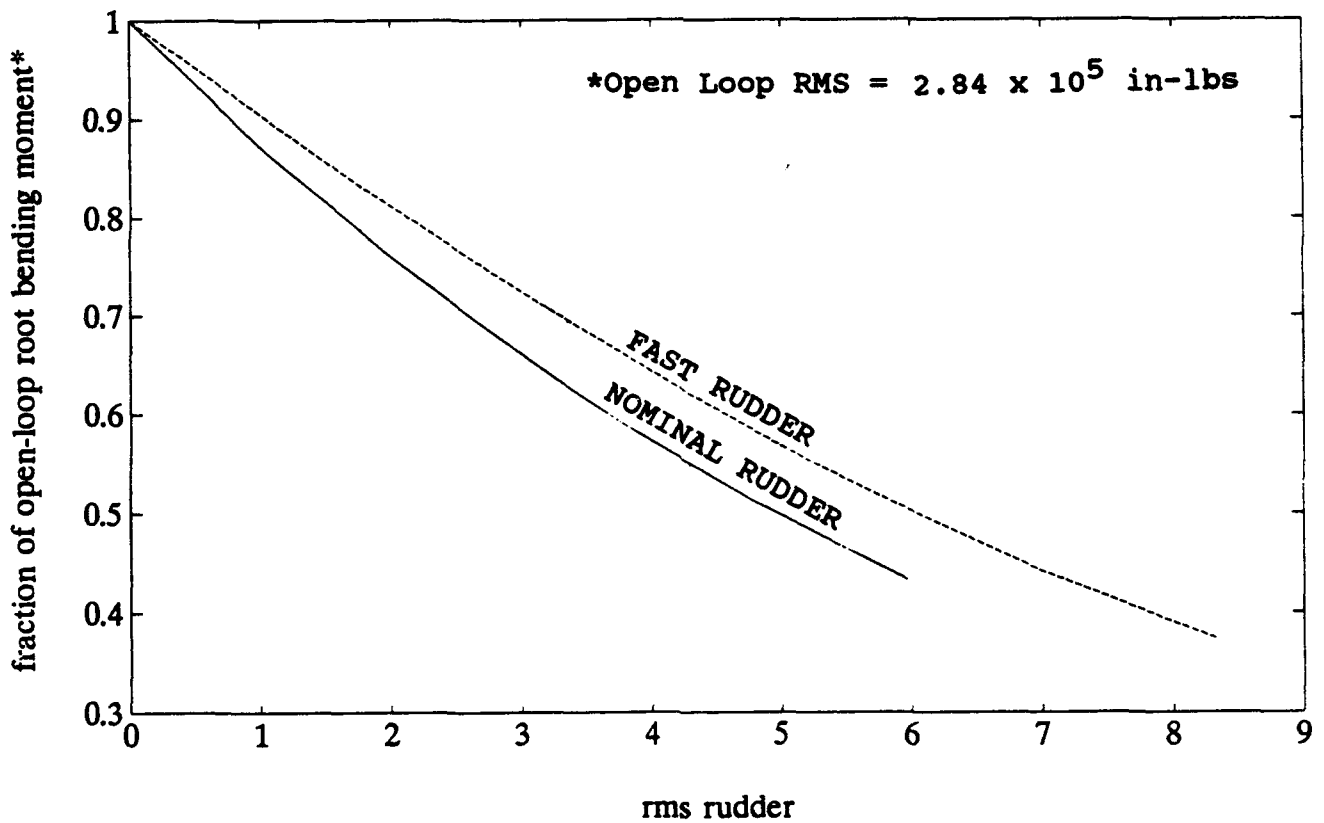


Figure 21. Same as Fig. 20, except only for frequencies in the range 10-20 Hz.

rudder displacement  $\delta_R$ , as shown on the abscissas. It is believed, from the standpoints of hydraulic power absorbed and of

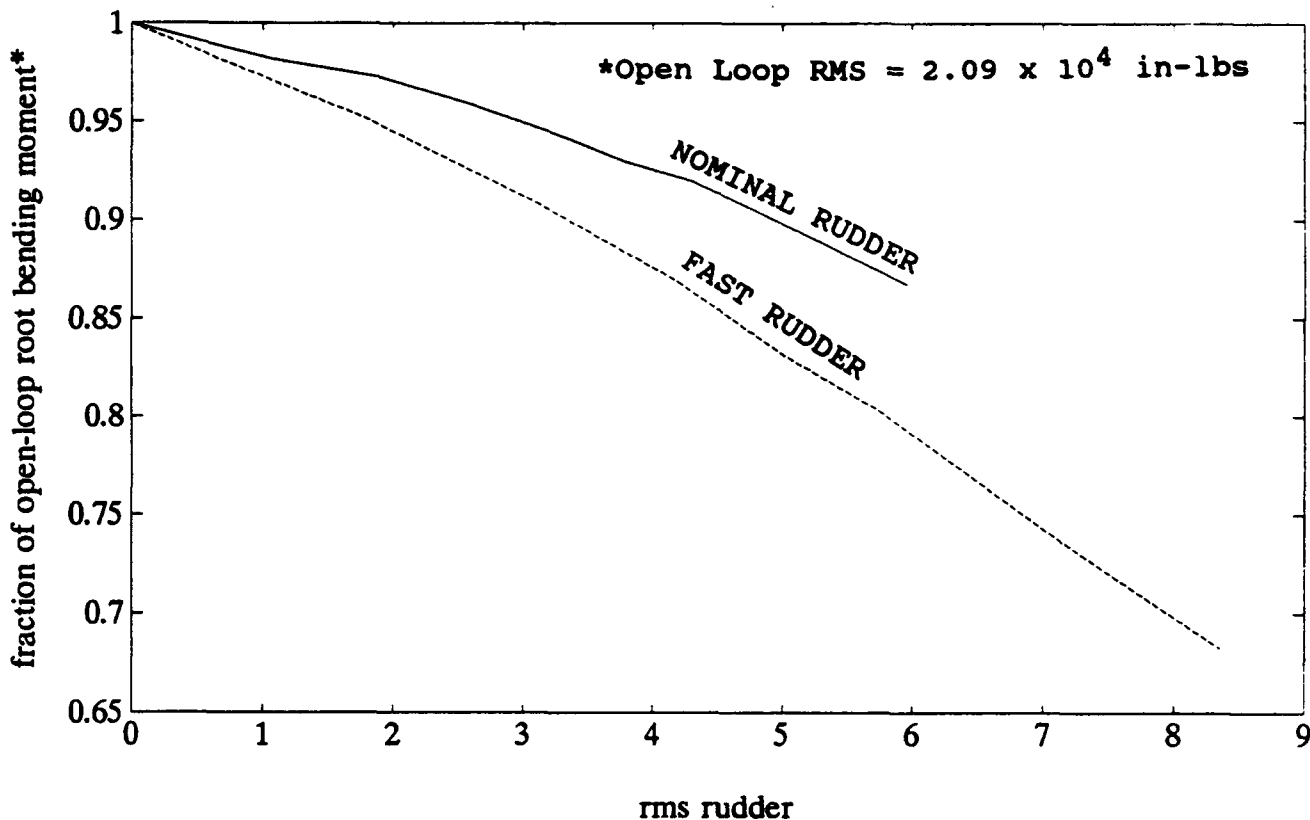


Figure 22. Same as Fig. 20, except only for frequencies in the range 32-55 Hz.

structural capability, that 3 to 5 degrees RMS are probably acceptable. The rudder model labeled "nominal" in Fig. 20 is quite close to the existing F/A-18. To be specific, the relationship between the "command" and actual rudder angles, as suggested by the manufacturer, is given by Eq. (20). The "fast" rudder has these two angles equal -- a desirable ideal but impractical on physical grounds. One sees that at 3 degrees, a 25% reduction in RMS moment is possible with the existing system.

As above, these results were calculated for the flight condition  $\alpha = 32^\circ$ ,  $q_\infty = 300$  psf. For each plot, the open-loop

RMS moment is noted in the upper right corner. Figure 20 covers the entire frequency spectrum of interest. Figs. 21 and 22 relate, respectively, to relatively low frequencies and to a higher range bracketing the second mode. Each was constructed by integrating area under the PSD in the indicated interval of  $f$ . From Fig. 21, the "fast" rudder is seen in this range not to do as well as the nominal, whereas overall and at higher  $f$  their effectiveness is reversed. This is because the direct acceleration feedback in the 10-20-Hz range is modified relatively little by rudder transfer function Eq. (21); there is therefore less direct damping and less energy reduction than at higher frequencies.

For purposes of fatigue life estimation, as introduced in Subsection 3.3, bending stress was used at the root of spar #7 shown in Fig. 4. This lies just ahead of the rudder hinges and has coordinates  $x_v = 89.7$  in,  $z_v = 0$  in the frame used for fin structural analysis. Fatigue data for the 7075 T651 Aluminum alloy was taken from Fig. 5.2.1, Vol. I of Ref. 15 and other sources.

Figure 1.4 of Ref. 15 tabulates the number of seconds, per typical 1000 flying hours of the F/A-18 fleet, spent at each of many combinations of  $\alpha$  and dynamic pressure  $q_\infty$ . Response PSD matrices  $[S_q]$  were calculated only for  $\alpha = 20, 24, 28, 32, 36$  and  $44$  degrees, so the flight times for the rows near each of those angles were combined to give a  $6 \times 9$  time-usage matrix. No significant damage has been reported for  $\alpha \leq 16^\circ$  or  $\geq 46^\circ$ , and

these ranges were, therefore, neglected. At each  $\alpha - q_{\infty}$  combination, the PSD's of moment and stress were determined from Eqs. (31-32), neglecting the CSD's in matrix  $[S_q]$ . The stress was assumed to be a zero-mean Gaussian process, which permitted a table of stress exceedances per unit flight time to be estimated by methods described, e.g., in Ref. 18 or Chap. 11, Ref. 10. After cumulating the stress exceedances and dividing them by the corresponding number of cycles to failure from the "S-N curve," it was possible to estimate the fraction of damage to failure used up in 1000 flight hours. The inverse of this fraction is the probable number of hours to failure.

For two levels of feedback gain plus open-loop, and at these six values of  $\alpha$  with input PSD's from Fig. 15, buffet responses similar to the foregoing were calculated. When converted to statistics of fin-root stress by the method described above and in Subsection 3.3, these led to fatigue-life estimates.

In view of the well-known presence of "stress raisers" in any such structure, stresses were adjusted by multiplication with\* "K-factors." Values  $K = 1, 3$  and  $5$  were chosen; for comparison,  $K = 3$  would be appropriate for an open circular hole. Plots of the relative damage were prepared at each  $q_{\infty}$ - $\alpha$  combination. Although the levels vary dramatically, at each condition the damage tends to peak around  $q_{\infty} = 150$  psf and at  $\alpha$ 's of  $32^{\circ}$  and  $36^{\circ}$ . This fact is apparently connected with the relatively large times of flight in these portions of the  $\alpha - q_{\infty}$  matrix.

\*Called "Stress Factors" on Figures 33 a) and b).

Only one to five seconds per 1,000 hours are flown at higher  $\alpha - q_{\infty}$  combinations. Small changes to those times will greatly affect predicted life. Some quantitative cumulative results are shown in Table 1.

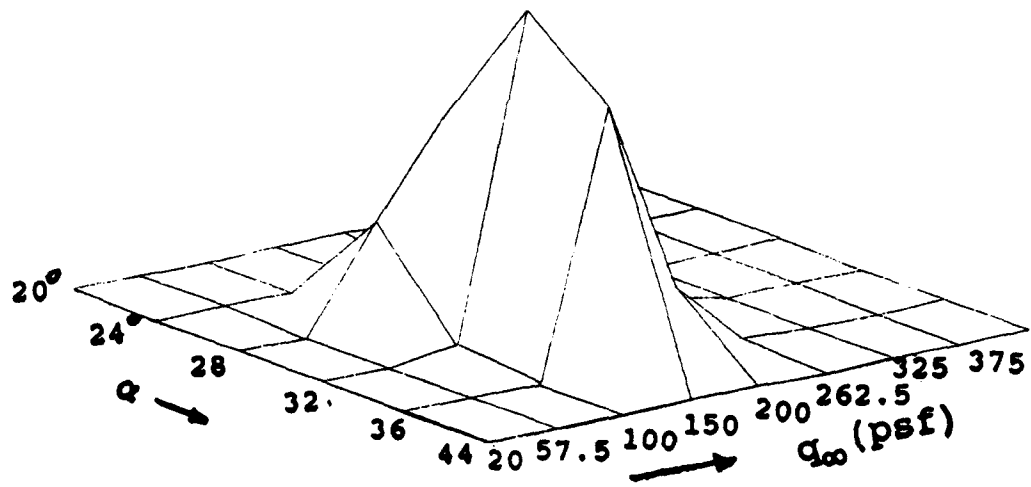
Table 1  
Relative fatigue damage with and without active control.

Feedback Factor (Gain)	Stress Factor K	Life Used in 1,000 Hr. (1.0 indicates failure)
0.0 (Open Loop)	1.0	$6.78 \times 10^{-11}$
	3.0	0.0178
	5.0	0.664
0.4	1.0	$2.08 \times 10^{-17}$
	3.0	$7.10 \times 10^{-4}$
	5.0	0.0952
0.8	1.0	$1.58 \times 10^{-24}$
	3.0	$4.09 \times 10^{-5}$
	5.0	0.0192

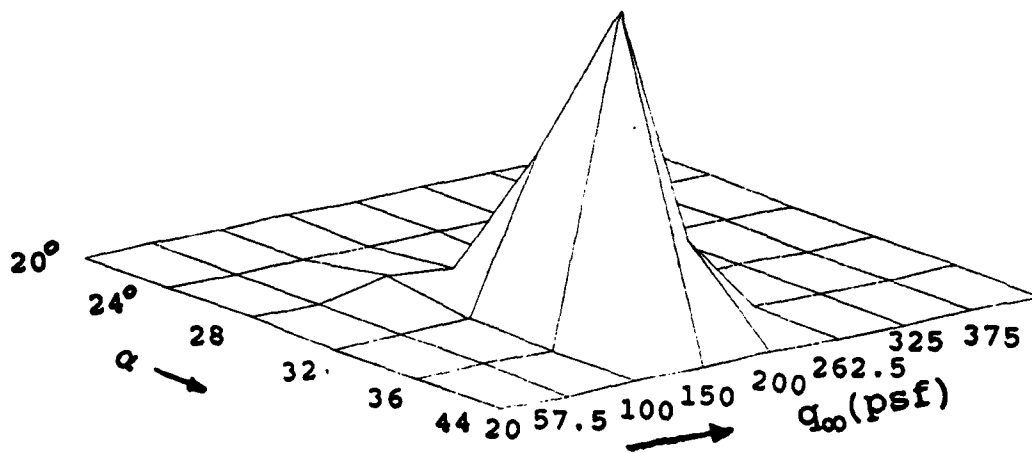
The predicted lives, as anticipated, are larger than what probably applies to the actual F/A-18. It is the relative magnitudes that are believed important, since they measure what can be accomplished with realistic active rudder control. The open-loop figure of 0.0178 at  $K = 3$  corresponds to about 56,000 hours of operational flying before failure and is not inconsistent with estimates for the redesigned tail with LEX fence installed. F/A-18 project personnel agree that a gain of 0.4 is "feasible," and its realization is seen to increase predicted life by a factor of about 7 at  $K = 5$  and 25 at  $K = 3$ .

Although no graphs of spectra are included herein, the stress responses to the very smooth input-pressure PSD's show sharp peaks in the vicinity of the expected 17 and 48 Hz. Their relative heights depend on flight speed, with 48 Hz becoming more prominent as speed is increased. Figures 23 a) and b) are typical rough plots of relative structural damage (plotted upward), as it occurs for various ranges in the  $\alpha$ - $q_\infty$  matrix. Both are for  $K = 3$ , but Fig. 23 a) describes the uncontrolled system and Fig. 23 b) a feedback gain of 0.8. In both cases, most damage is seen to fall only in a relatively few locations, but active control tends to push these toward higher  $\alpha$ .

In conclusion for the F/A-18, it is felt that a satisfactory representation of the buffeting fin/rudder has been constructed, despite its simplicity. Feedback control to the existing rudder is shown to have potential for significant improvements to structural fatigue life.



a) Open Loop, Stress Factor = 3.0



b) Feedback Factor = 0.8, Stress Factor = 3.0

Figure 23. Relative damage to F/A-18 fin root.

## 4.2 THE F-15 AIRCRAFT

Figure 1 is a general plan view of the vehicle, and Fig. 24 is added here to provide details on the fin/rudders and all-movable stabilators. Both surfaces play important roles, both aerodynamically and structural-dynamically, in buffet response. Elastic and inertial properties were supplied by the manufacturer in forms similar to those for F/A-18. The finite-element (F.E.) "stick model" constructed by ALGOR had to be much more complicated, however, in view of the coupling role of the aft-fuselage boom. It should also be mentioned that, although some of the following figures depict a right empennage, the left-hand (port) fin was the object of interest. Because it carries a 6-lb tip pod vs. 2-lb on the right (cf. Fig. 24), it was the one which experienced fatigue damage prior to the reinforcement program.

Figures 25 and 26 show the undeflected "stick models" for one fin-rudder and stabilator supported by the aft fuselage boom. Since this last structural member is assumed to be cantilevered from a frame which simulates the aft heavy engine mount, the predicted modes and frequencies cannot exactly match test data taken on a complete airplane or even on a more extensive version of the rear fuselage.

It will be recalled that, on the F/A-18 model, it was necessary to reduce the constant of the fin-root roll spring (supplied as part of the "stick model") by about 1/3 in order to



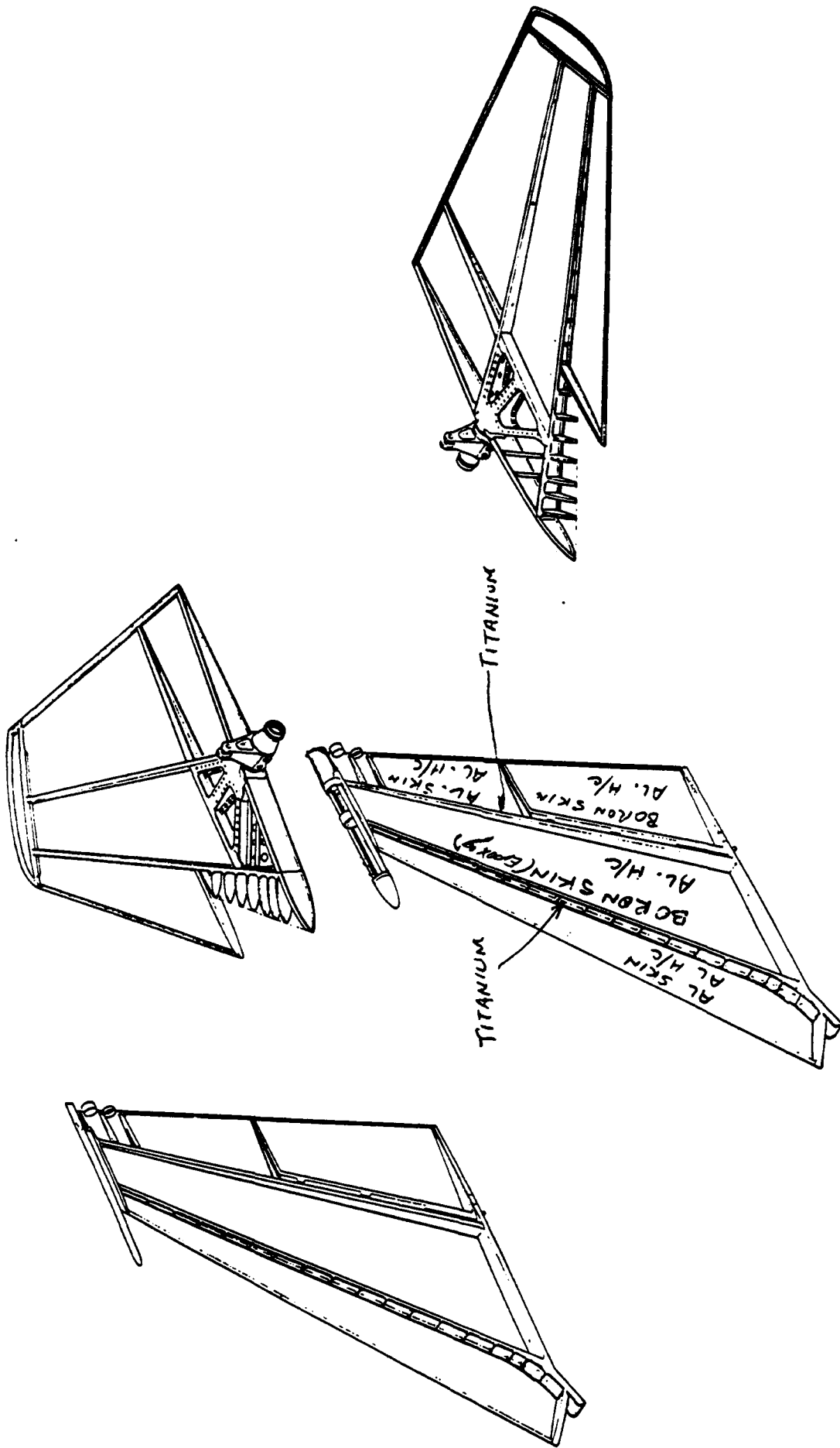


Figure 24. Exploded view of right- & left-hand F-15 fins and stabilators, with details of structural layout and fin materials.

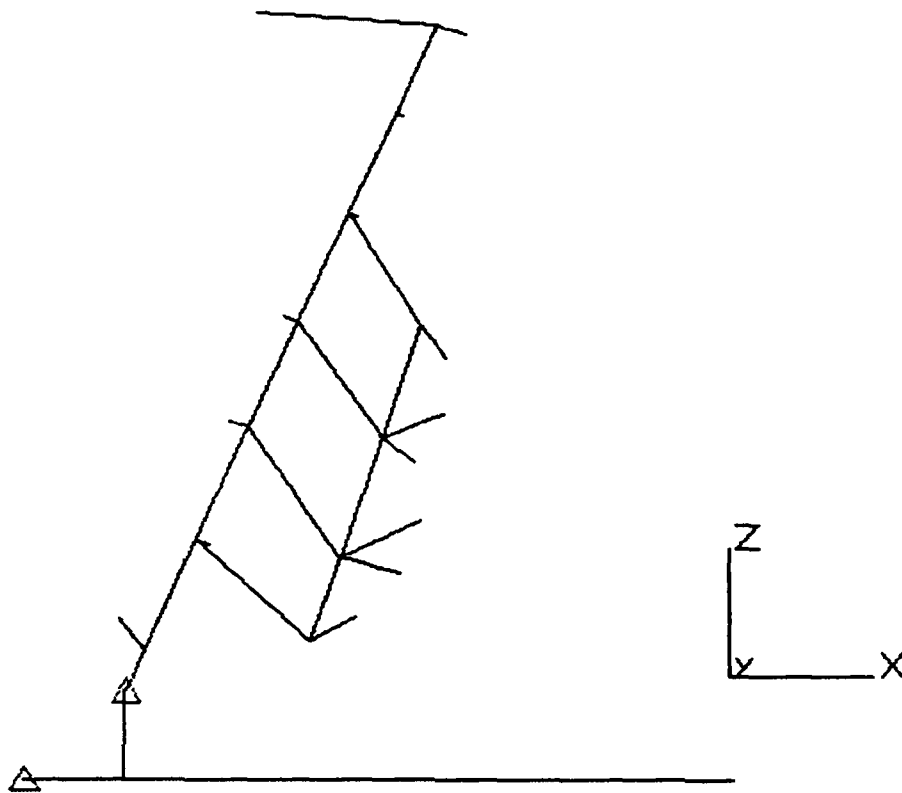


Figure 25. Nodes and elements for F.E. model of F-15 fin and rudder. Concentrated inertias are assigned to each node, but only the elements along the E.A.'s have finite beam-rod elasticities.

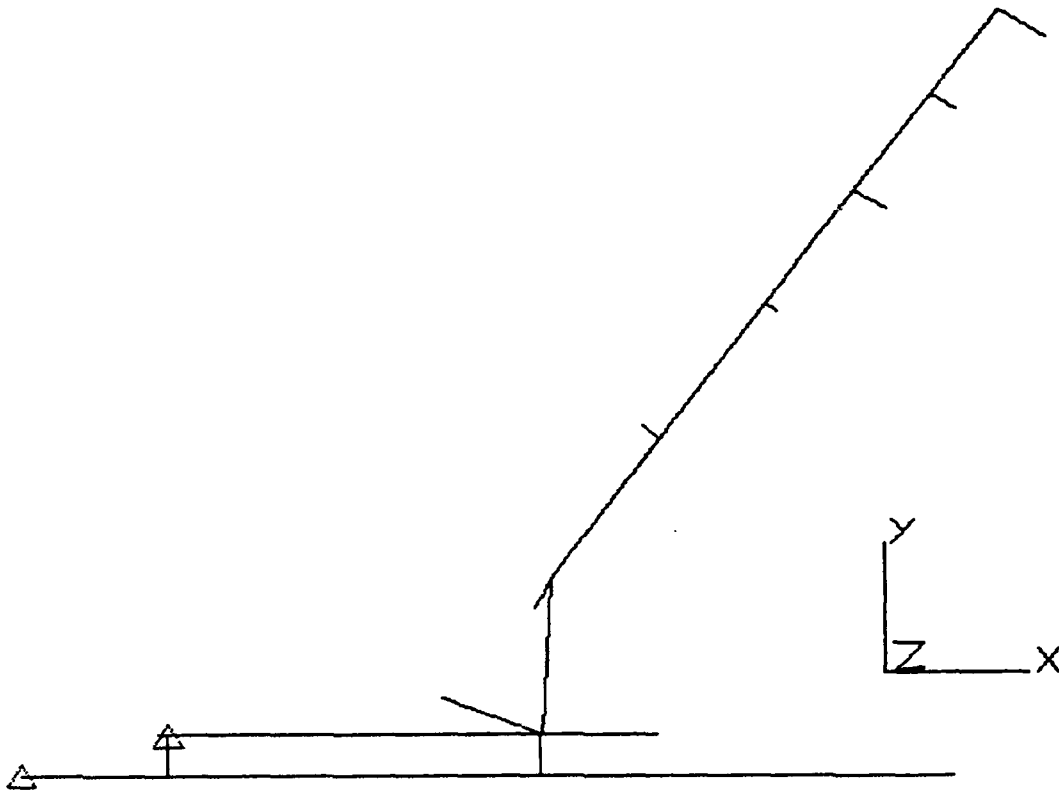


Figure 26. Nodes and elements for F.E. model of F-15 all-movable stabilator and aft-fuselage boom. (Property assignments similar to Fig. 25.)

get close agreement with tests on the fin first bending frequency. The same sort of adjustment -- but by a factor of 1/10 -- has been made for the F-15 fin root. This is, however, the only "tuning" applied to the McDonnell data. The rather substantial decrease to the relevant spring constant brought the fundamental F-15 frequency down to 10.78 Hz, vs values in the range 9.2 - 9.8 Hz from various ground vibration tests. Figures 27 through 30 present sketches and frequencies for the first four boom/stabilator/fin modes, the shapes being predicted by the ALGOR code. As

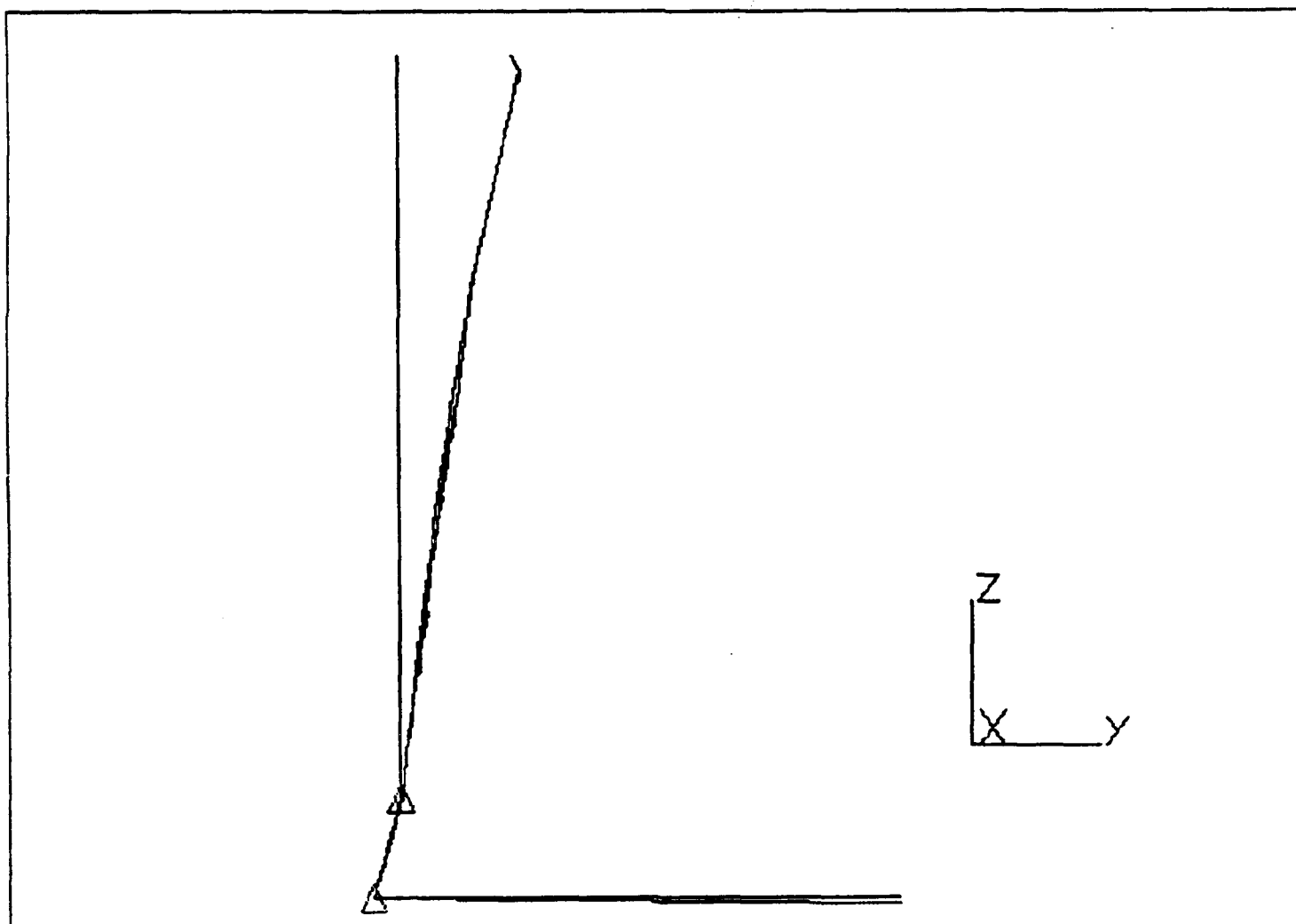


Figure 27. F-15 first bending mode, as seen from rear.  
 $F_1 = 10.87$  Hz vs. measured 9.2 - 9.8 Hz.

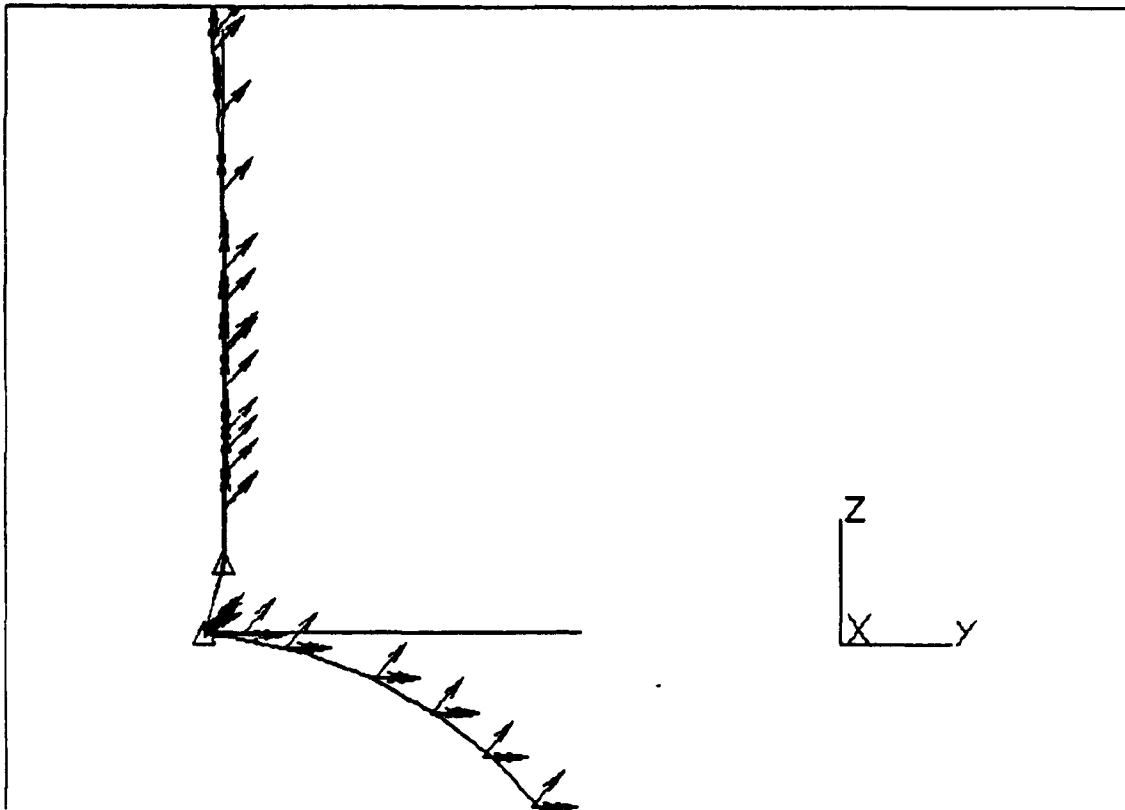


Figure 28 a). F-15 second combined mode, as seen from rear.  
 $F_2 = 27.06 \text{ Hz}$  vs. measured 30 Hz.

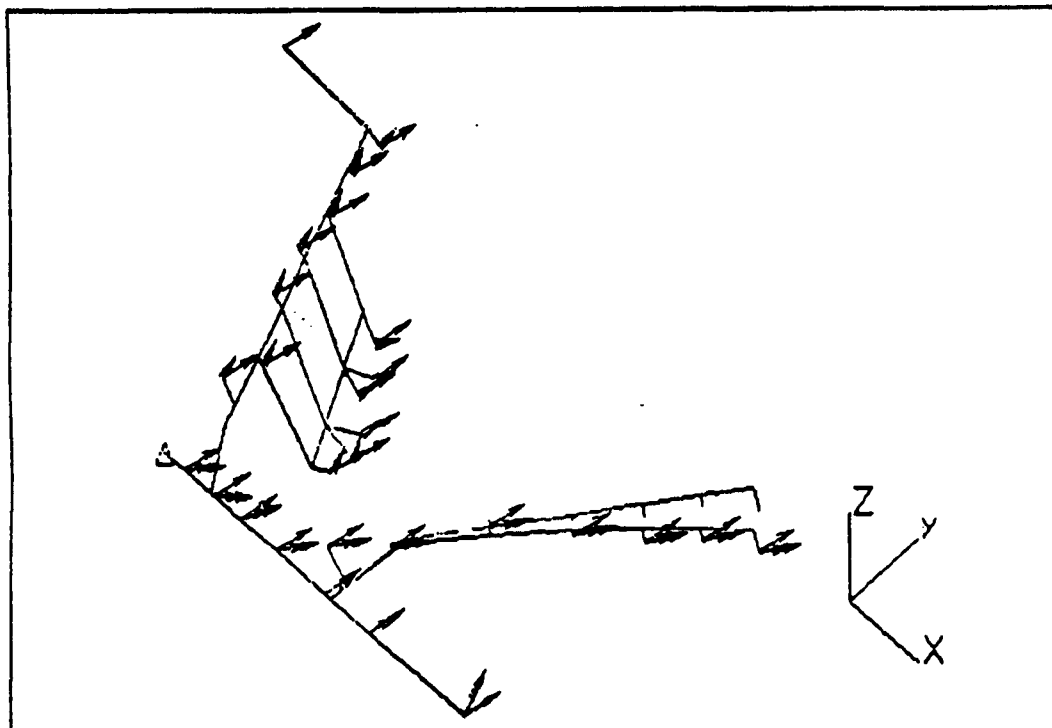


Figure 28 b). F-15 second combined mode ("Stick-Figure" fin, rudder, stabilator and aft fuselage boom, seen in three-quarter view).

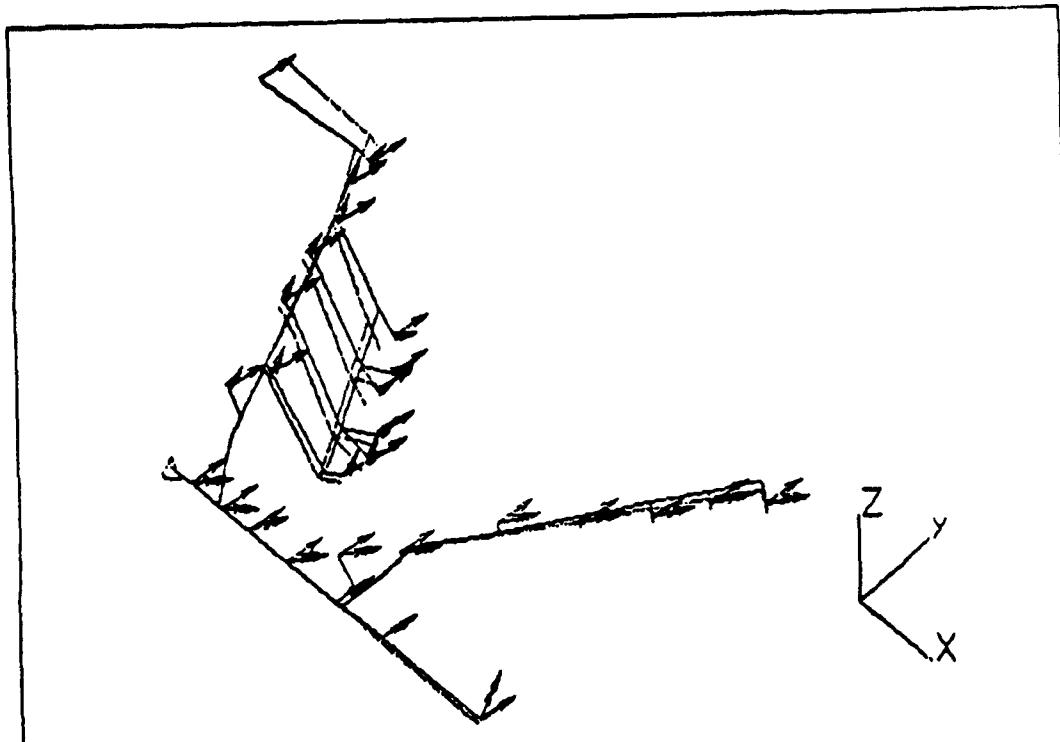


Figure 29. F-15 first fin torsion mode, seen in three-quarter view.  $F_3 = 41.23$  Hz vs. measured 32 Hz.

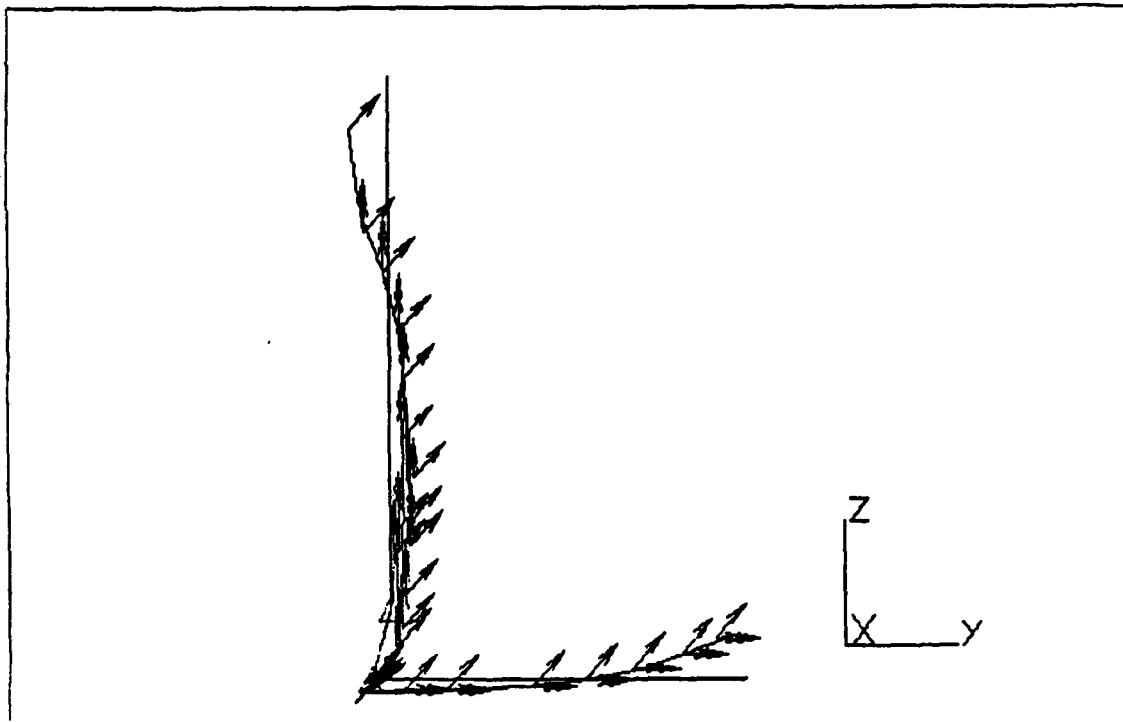


Figure 30. F-15 second bending mode (with rudder rotation, as seen from rear).  $F_4 = 44.1$  Hz vs. measured 36.5 Hz.

mentioned, the right half of the empennage has been analyzed, but with a fin-tip mass representative of the left half. The views shown in Figs. 28 b) and 29 are at a 3/4-perspective from above, inboard and aft. The "stick model" appears both in its central position and at its maximum deflected position during a vibration cycle, the latter being identified by small arrows at the nodes. In Fig. 28 a) the second mode is displayed as seen from the rear, in order to emphasize the relatively small amplitudes of fin motion. This is a problem and will be discussed further below.

The four modes illustrated are the ones converted to state-vector form for design to control actively the buffet response. Although modes 3 and 4 do not agree quantitatively with measured airplane frequencies, their shapes correspond quite closely with those reported. However, the bulk of full-scale fatigue damage, prior to fin reinforcement, was associated with mode 2 and, to a lesser extent, with mode 1. In this respect, there is incomplete agreement between the present model and flight experience. The mode 2 shape measured by McDonnell combines bending and torsion of the fin, with amplitudes much larger than appear in Figs. 28. It is believed that more details of the aft-fuselage structure will have to be included in the ALGOR model in order to attain better agreement with the actual aircraft's dynamic behavior.

A preliminary decision was made to use the fin-tip accelerometer numbered A2 during flight testing, for two very different purposes. It served as the initial input for development of active control algorithms, but its readings (PSD, RMS level,

maxima, etc.) were also judged to be a suitable measure of damage accumulation. This is because observed F-15 fatigue damage was entirely in light, secondary structure ahead and behind the main fin structural box. By reducing deformations and acceleration levels near the tip, this behavior was brought under control. Therefore -- and subject to further verification -- this was felt to furnish a "surrogate" to be subject to active feedback in the same sense that root bending moment served on the F/A-18.

The complete F-15 "plant," together with input excitation, then consisted of the following:

- 1) Four linear modal equations of motion (cf. Eq. (2)) based on the modes and frequencies previously described. Generalized masses are normalized to unity in the pound-force-inch-second system by ALGOR. Tentatively, the structural damping coefficients were set equal to zero.
- 2) Generalized aerodynamic forces  $A_{ij}$ , as calculated by LATIS1 for the aeroelastic terms in the equations. They were approximated by polynomial curve-fits for the reduced-frequency dependence of the eight real portions of the four complex  $A_{ij}$ . These achieved the same level of precision as on the F/A-18. Both fin/rudder and stabilator contributed to the forces.
- 3) Also from LATIS1, aerodynamic terms associated with prescribed rudder oscillations. Curve-fits were similarly

developed for these. From data, giving the effect of  $\alpha$  on stability derivatives due to the fin, fin lift-curve slope, etc., estimates were made of the reduction of average dynamic pressure over the fin (below free-stream values). This reduction is required as a correction to both the  $A_{ij}$  and rudder inputs. It was determined as follows. Table 2, Vol. II, of Ref. 1 lists four fin aerodynamic coefficients for several values of  $\alpha$  at sideslip angle  $\beta = 2^\circ$ , which is close enough to the assumed zero-sideslip condition. The adjoining Fig. 2 of Ref. 1 includes quantities like the side-force derivative  $\partial C_F / \partial \beta$  at  $\alpha = 22^\circ$ , and these can be used as a check on derivatives estimated from the Table 2 data. The chosen approximation was to assume that, for each  $\alpha$ ,

$$\frac{q}{q_\infty} = \frac{\partial C_F / \partial \beta}{(\partial C_F / \partial \beta)_{\alpha=0^\circ}} \quad (36)$$

All Ref. 1 measurements come from a 13%-scale model, so that one is also neglecting effects of Reynolds No. when extrapolating to the flight article. (Again, Mach No. effects are deemed insignificant.) Some overall confidence is added, however, by the observation that a roughly corresponding trend vs.  $\alpha$  is exhibited by other derivatives.

The results of this process are summarized in Table 2.



Table 2  
Influence of angle of attack on  
averaged effective dynamic pressure  
over the F-15 fin/rudder.

$\alpha$ (degrees)	$q_{\text{averaged}}/q_{\infty}$
0	1
18	1
20	0.932
22	0.815
24	0.685
26	0.540
30	0.317
35	0.3 (approx)

It is of interest that near  $\alpha = 22^\circ$ , where most of the fatigue damage is reported to have occurred, the dynamic pressure remains above 80%.

- 4) Power-spectral densities (PSD) and associated generalized forces for the buffeting pressures. These have been constructed entirely from reported measurements (Ref. 1) on a "rigid" 13%-scale model. Basically, the data consist of power spectra and RMS levels at  $\alpha = 22^\circ$  for 39 pairs of locations. From these the forcing pressure differences  $\Delta p$  were constructed by means of the assumption that pressures are nearly anti-correlated on opposite sides of the same fin station. This approximation is quite well justified by examination of cross-spectral densities between pairs of such opposing pressure sensors. The evidence is convincing for both F-15 and F/A-18.

Another idealization that appears justified by the Ref. 1, Vol. II, data is that the spectral shapes are almost the

same for all stations, although of course the RMS levels of  $\Delta p$  vary substantially over the fin. Figure 31 shows an accurate curve-fit obtained from fin station #7, near the leading edge and the tip; all that has been done here was to smooth out very high-frequency, low-level "noise" in the data. As an overall factor for input generalized forces, the station #7 PSD was normalized so that the area under it is unity, when plotted vs. the dimensionless frequency  $fb_r/U_\infty$ . Here  $f$  is in Hertz,  $b_r$  is the fin mean aerodynamic chord (81 inches, full-scale), and  $U_\infty$  is the airspeed in

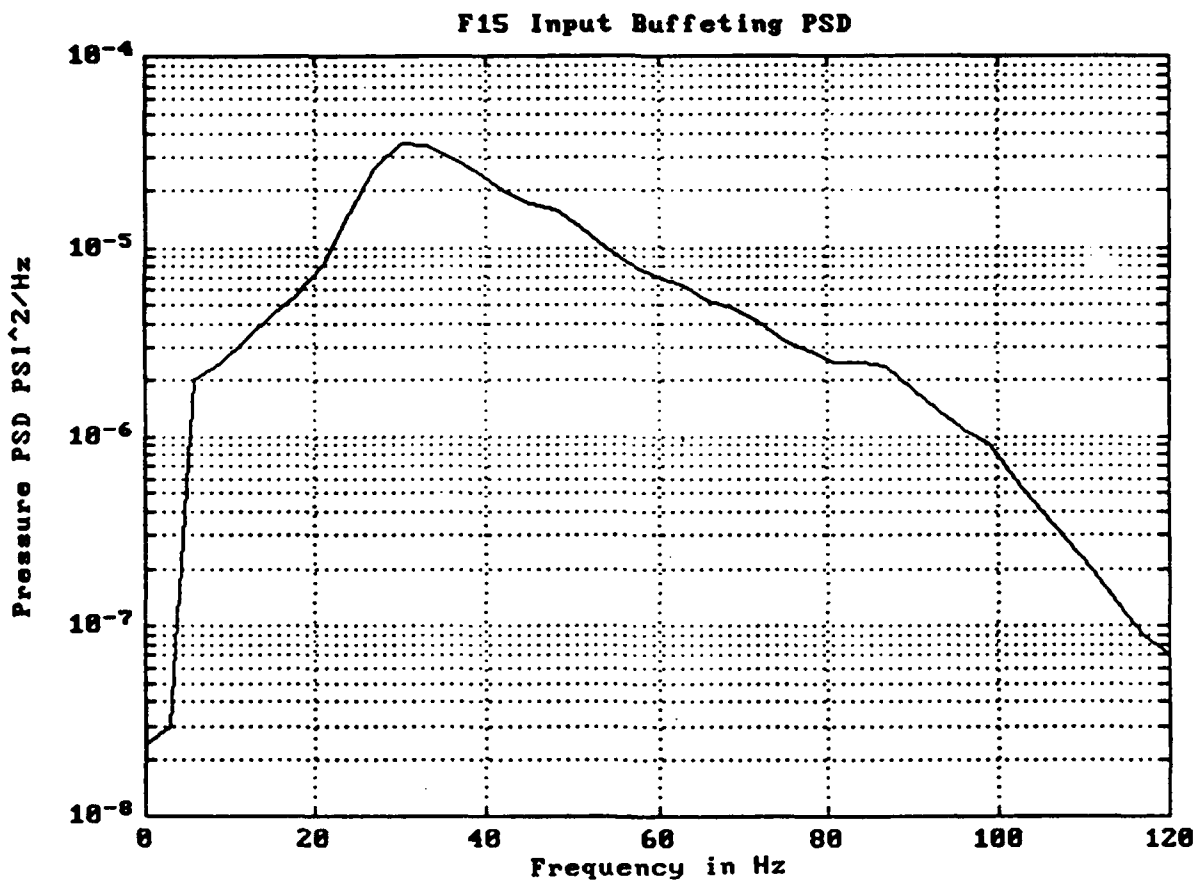


Figure 31. PSD of the pressure in psi, measured at station #7 ( $x = 17.15$  in,  $z = 94.05$  in according to system used here) on a 13%-scale model of a rigid F-15 fin (Ref. 1).  $\alpha = 22^\circ$ ;  $q_\infty = 12$  psf.

consistent units. The area normalization has the effect that each station's  $\Delta p$  contribution must be multiplied by the RMS pressure level there so that mean-square values are correct. Figure 32 repeats this normalized curve.

The buffeting inputs to the F-15 fin/rudder have been used as a vehicle for experimentation with approximations to the PSD/CSD's for the corresponding modal generalized forces. The concept is to take account of partial spatial correlations among the  $\Delta p$ 's at the 39 model stations, as well as these correlations can be inferred from the Ref. 1 data. At the same time, it was

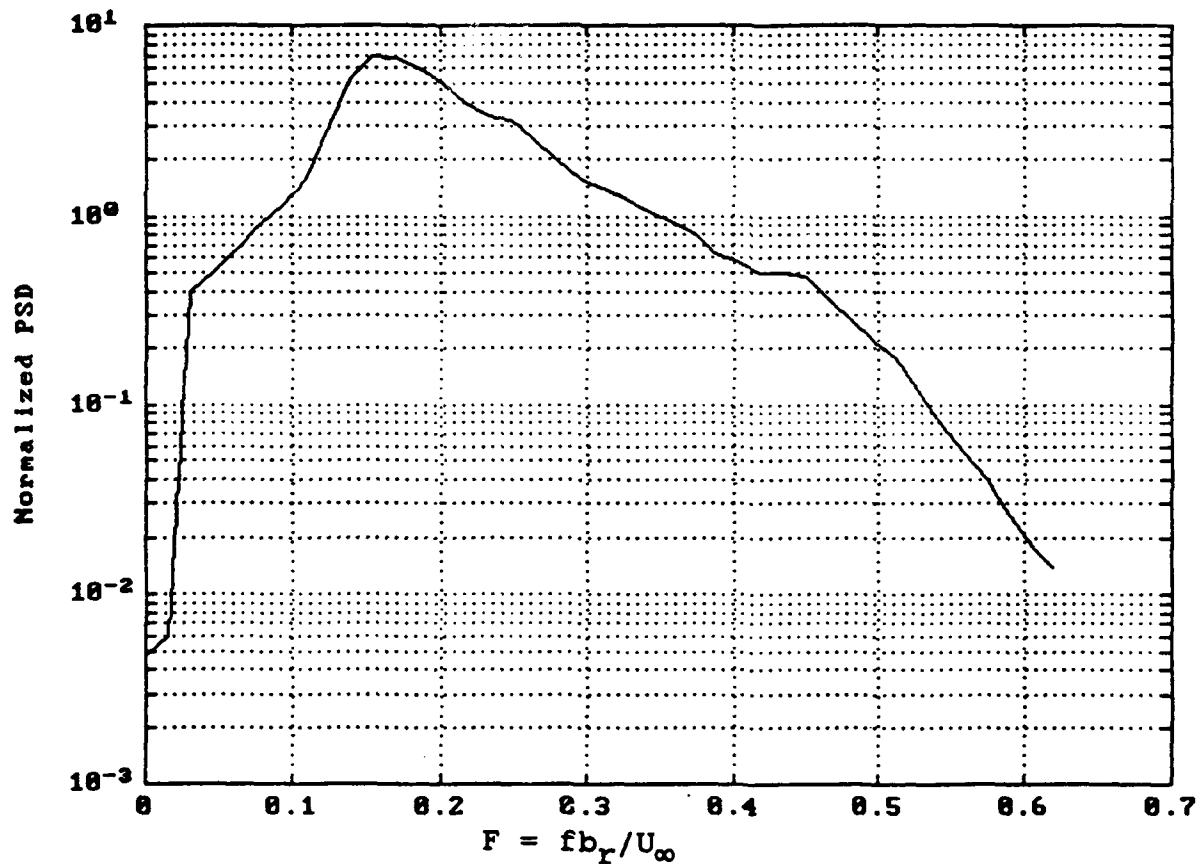


Figure 32. PSD of Fig. 31, plotted vs. dimensionless frequency and normalized to unit area under the curve.

necessary for feasible control-system design to adopt the single pressure spectrum of Fig. 32 as an overall factor on the input. In view of the complexity of these steps, the reader is referred to Appendix A for derivations and some numerical results.

Because direct feedback from a fin-tip accelerometer to command rudder displacement proved so successful for reducing the F/A-18 response, the same approach was tried initially on the F-15. Full-scale measurements in the laboratory and in flight included readings from four such accelerometers. Their locations might, therefore, be suitable for operational instruments driving an active control system. Table 3 provides coordinates in McDonnell's airplane reference frame, along with their transformation to the local frame used herein\*.

Table 3

Coordinates, in two reference frames, of four accelerometers mounted on the right F-15 fin.

Designation	WL(in)	FS(in)	x(in)	y	z(in)
A1	238.6	835(est)	70.0	0	108.6
A2	251.6	790.0	25.0	0	121.6
A3	251.6	815.0	50.0	0	121.6
A4	251.6	830.0	65.0	0	121.6

Analyses were carried out only at the one flight condition,

\*For F-15, the origin is at the root of fin E.A., which is along the 47%-chordline, with y outboard to the right (see Fig. 1).

$\alpha = 22^\circ$ ,  $q_\alpha = 245$  psf, at sea level, which was identified by the manufacturer as a representative severe buffeting region of the flight envelope. In succession, signals from each of the four accelerometers were multiplied by a gain factor (which could be varied), then applied directly as  $\delta_{RC}$  to the rudder actuator. In each case the results were unsatisfactory: not only was the response not ameliorated, but an instability set in. In order to clarify this phenomenon for the reader familiar with control theory, four root loci were prepared. They are reproduced here, with scales in  $\text{sec}^{-1}$ , as Figs. 33 through 36.

Because of the relationships between the accelerometer locations and the fin mode shapes, this turned out to be a "non-minimum-phase" system. As the figures show, the four natural frequencies, which are the crossed poles on the imaginary axes, were acted upon in the same way by each accelerometer. Modes #2 and #4 are involved in pole-zero cancellations and essentially unaffected by increasing gain. Mode #1 undergoes a reasonable amount of damping as it is driven toward the origin. This is not unexpected behavior; the frequency near 10 Hz is well within the rudder's capability, so that acceleration feedback modified by transfer function Eq. (21) can easily remove energy from the almost purely bending motion seen in Fig. 27. On the other hand, Mode #3 is immediately driven into the right half-plane, with its instability increasing rapidly as gain increases.

Accel#1 to rudder

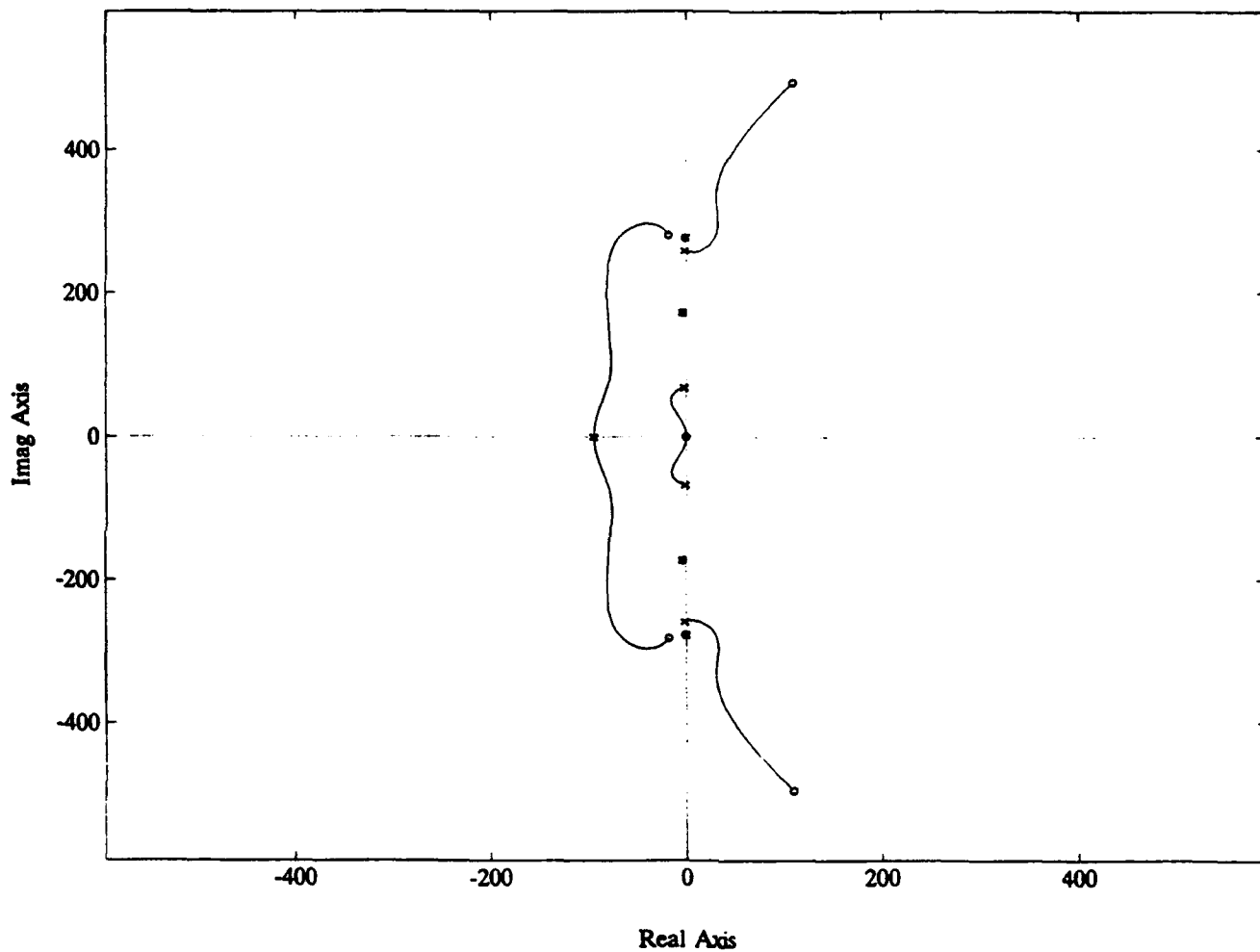


Figure 33. Root locus plot for feedback from F-15 fin accelerometer A1 to rudder command. Scales are in  $\text{sec}^{-1}$ .

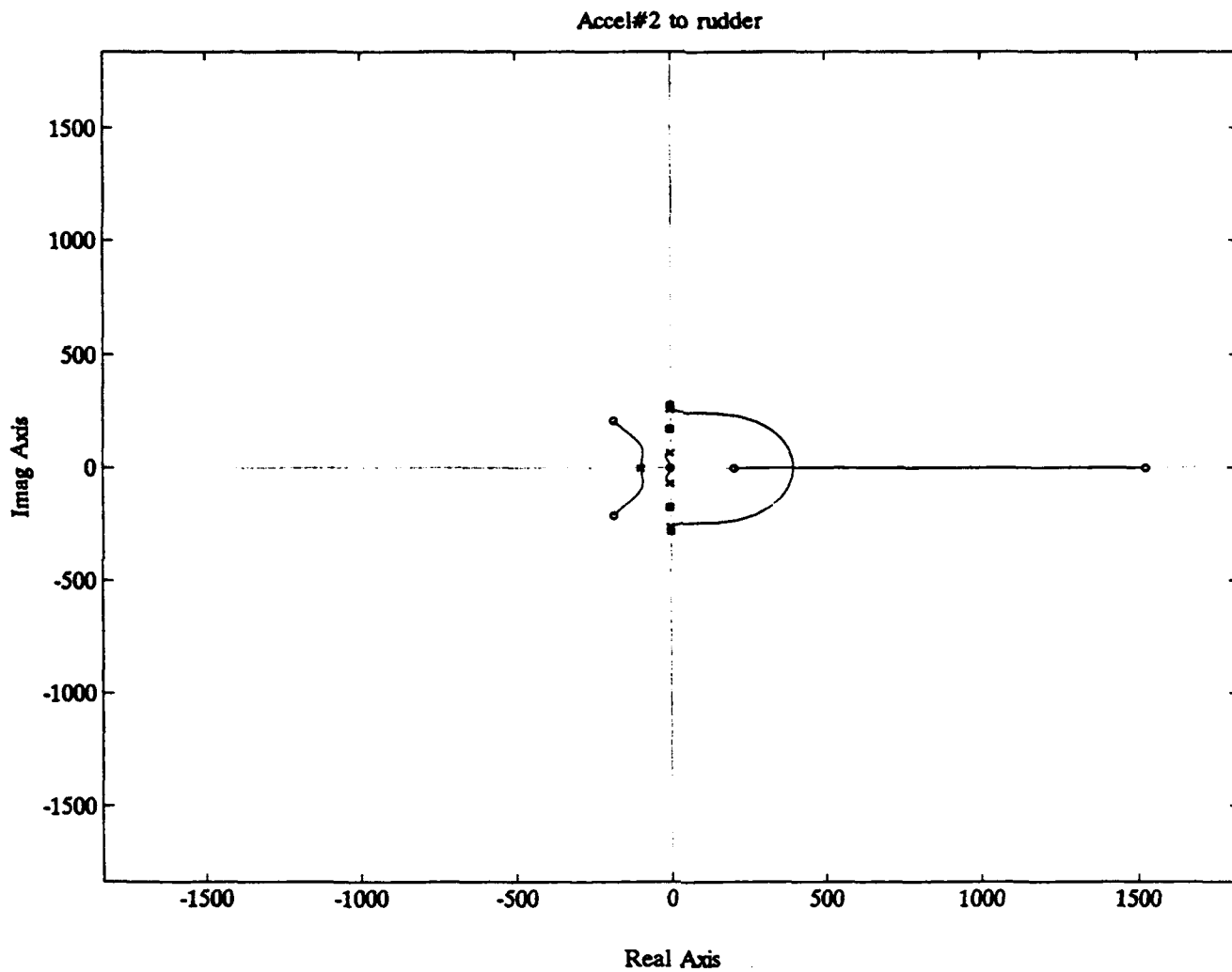


Figure 34. Root locus plot for feedback from F-15 fin accelerometer A2 to rudder command. Scales are in  $\text{sec}^{-1}$ .

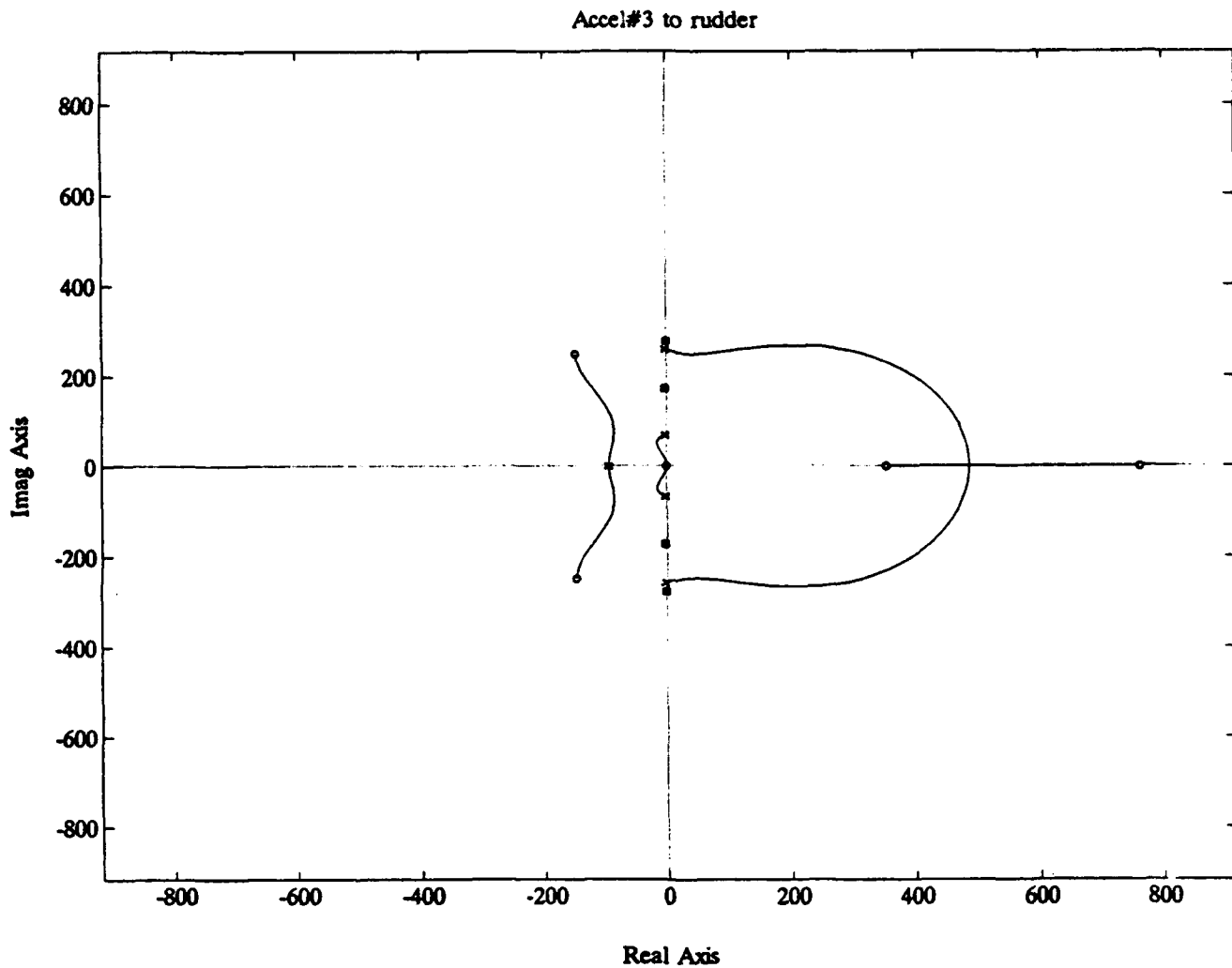


Figure 35. Root locus plot for feedback from F-15 fin accelerometer A3 to rudder command. Scales are in  $\text{sec}^{-1}$ .



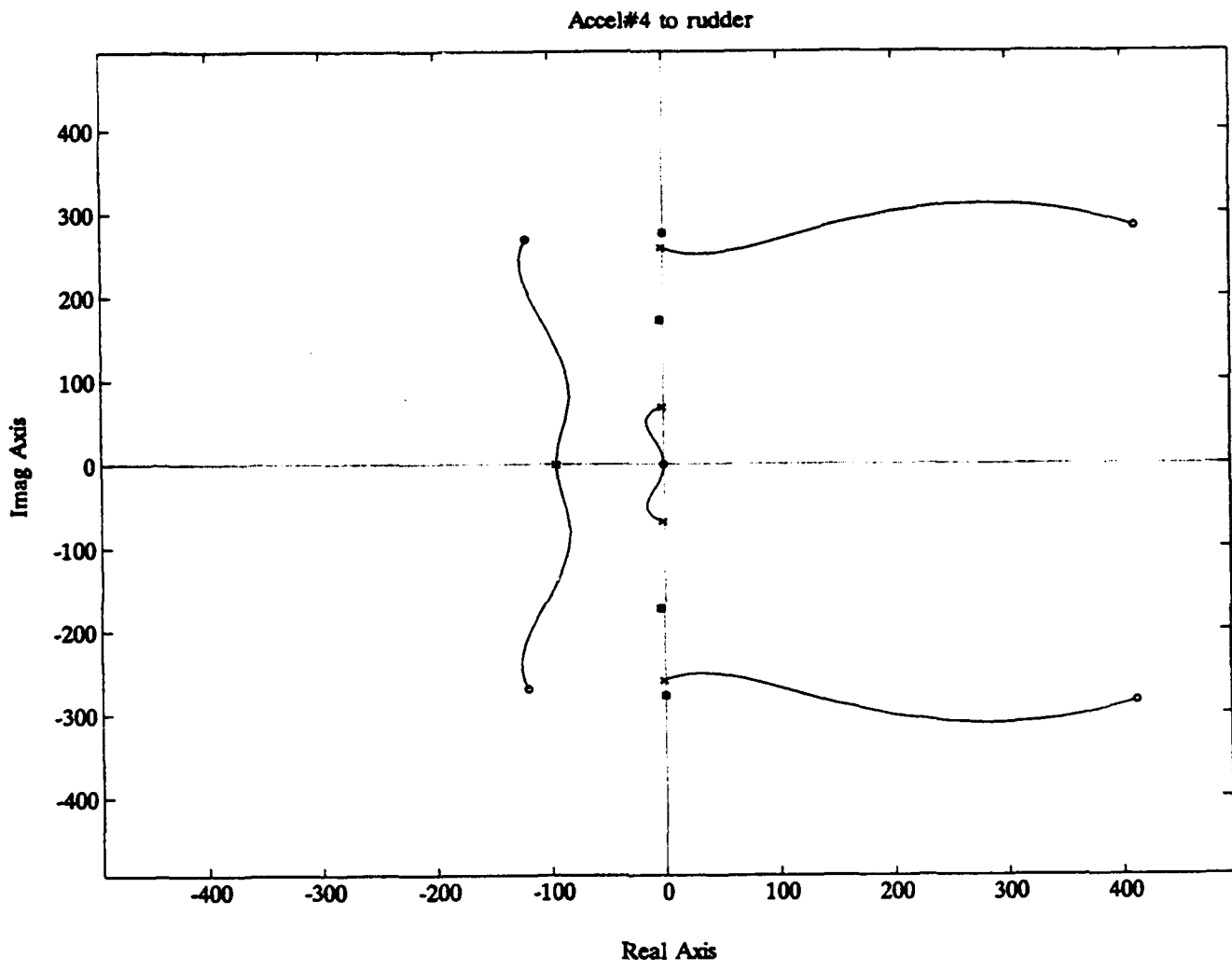
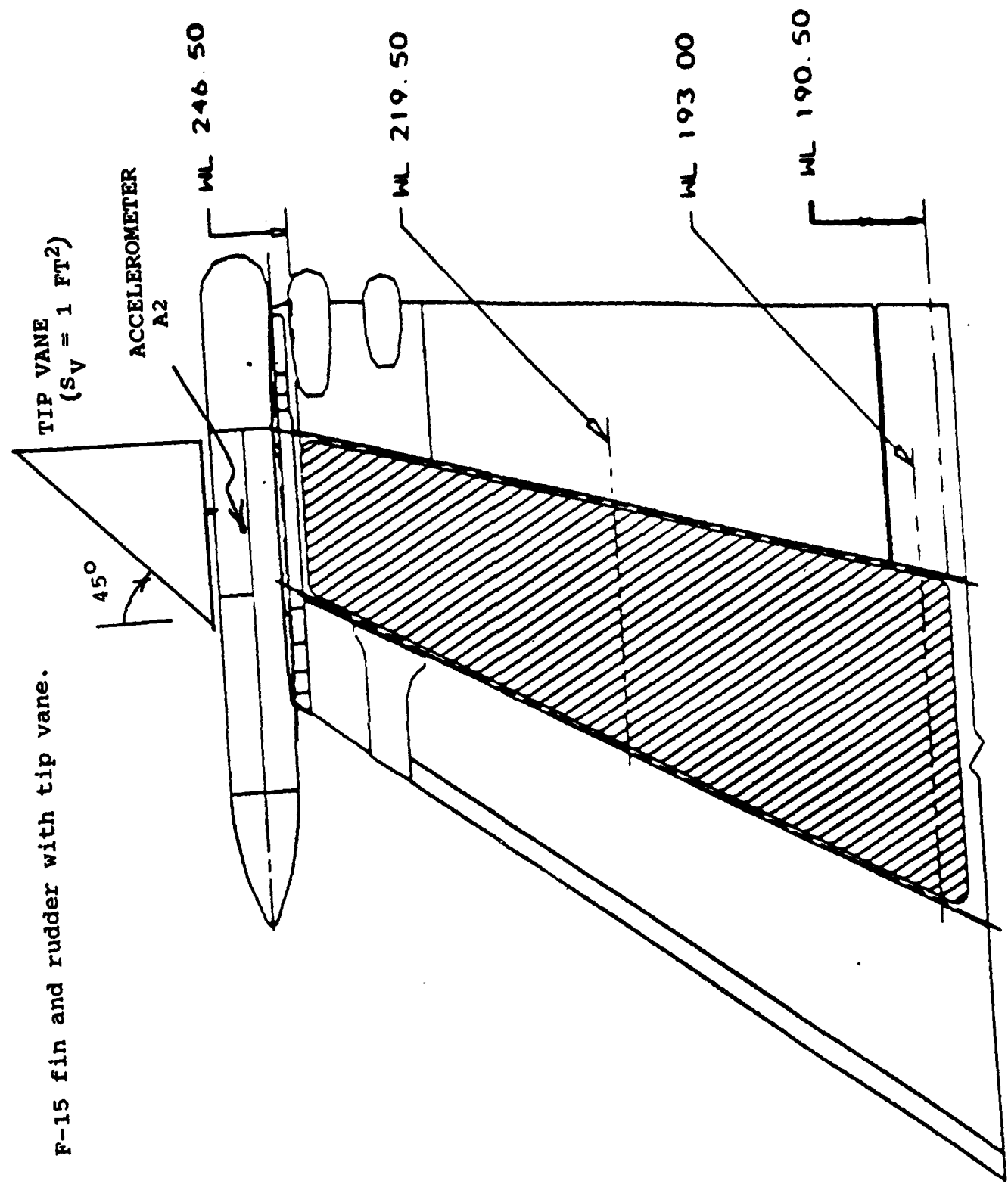


Figure 36. Root locus plot for feedback from F-15 fin accelerometer A4 to rudder command. Scales are in  $\text{sec}^{-1}$ .

The conclusion from this part of the effort to date is that, if the F-15 rudder is to be used for response reduction, a more complicated control scheme must be devised. It is believed that the improved system will have to involve a different instrument location (probably farther aft) and/or multiple instruments feeding a better optimized control algorithm. The latter alternative is regarded as more likely to be successful. It was decided, however, not to pursue this approach further at present. The small amplitudes of Mode #2 throughout the fin/rudder (cf. Fig. 28 a) are simply unrepresentative of the operational aircraft.

Although an auxiliary surface for aerodynamic excitation is unacceptable to the operators of the F/A-18, a tip vane like that illustrated (not to scale) on Fig. 37 might be feasible on the land-based F-15. The device chosen for initial study was a  $45^\circ$ -delta, hydraulically or electrically actuated so as to rotate  $\delta_T(t)$  about a vertical axis through its aerodynamic center (roughly at 60% of the root chord). It can develop a side force (or "lift")  $Y_T$  directly proportional to its angle  $\delta_T$  relative to the fin. That relationship was assumed quasi-steady, for convenience, but LATIS1 can readily account for aerodynamic unsteadiness as a function of frequency. Such a refinement would have an insignificant effect on feasibility. The axis location minimizes actuator loads and power, so it is not unreasonable to assume motions of a few degrees' amplitude up to a frequency of 50 Hz or higher.

Figure 37. F-15 fin and rudder with tip vane.



A location close to that pictured in Fig. 37 was chosen. If the coordinates of the base are  $x_{VT}$ ,  $z_{VT}$ , one can show that the vane adds to the right-hand side of Eq. (2) a term of the form

$$Q_{iT} = \delta_T(Y) \frac{\partial Y_T}{\partial \delta_T} [\phi_i(x_{VT}, z_{VT})] \quad (37)$$

$$+ h_T \frac{\partial \phi_i(x_{VT}, z_{VT})}{\partial z}$$

Here  $h_T$  is the height of the center of pressure above the base. The aerodynamic coefficient  $\partial Y_T / \partial \delta_T$  is proportional to the vane's lift-curve slope multiplied by  $qS_T$ , where  $S_T$  (1 ft<sup>2</sup> in the figure and examples) is the plan area. Dynamic pressure  $q$  should, at high  $\alpha$ , be reduced below  $q_\infty$ . But at the elevated position on the tail this reduction is probably not as large as those in Table 2. Although not applied here, there should also be a small adjustment due to losses in the gap between vane and fin tip.

Aside from the added cost, weight and complexity, one should point out another disadvantage of such devices. They will likely be situated in a region of violent motion due to combined structural dynamic and aerodynamic excitation. (Note the tip acceleration peak of 450 g, recorded for F/A-18 with LEX fence off and plotted on Fig. 40, Ref. 5.) It follows that the design must not only be reliable but very rugged.

Granted these circumstances, a tip-vane control system was studied which used accelerometer A2 as sensor. The signal was integrated once, multiplied by a gain constant and fed directly

to angle  $\delta_T$ . This results in a co-located velocity feedback system which is known to be extremely robust. Fin motion was then calculated just as in previous examples, with the PSD at A2 serving as a measure of response and an inverse measure of fatigue life. The results are presented in Figs. 38-40 at three increasing values of relative gain. In each case the input pressure spectrum is the same and is proportional to that in Fig. 31. The lower left-hand PSD characterizes the tip-vane activity, whereas acceleration at A2 appears at the upper left.

The RMS level of tip-vane displacement is a measure of control effort. Accordingly Table 4 was prepared to summarize the results.

Table 4

Root-mean-square levels of acceleration and tip-vane angle associated with the four levels of control in Figs. 38-40.

Relative Gain	RMS Acceleration at A2 (g's)	RMS Displacement $\delta_T$ (deg.)
Open-Loop	45.9	0
0.1	27.6	3.56
0.25	20.59	6.39
0.5	17.3	11.3

As in the case of the F/A-18 rudder, one sees a nonlinear effect of increasing control effort, with dramatic response reductions occurring at only a few degrees of RMS  $\delta_T$ . The 40% drop in RMS acceleration for slightly over  $3.5^\circ$  could constitute quite a

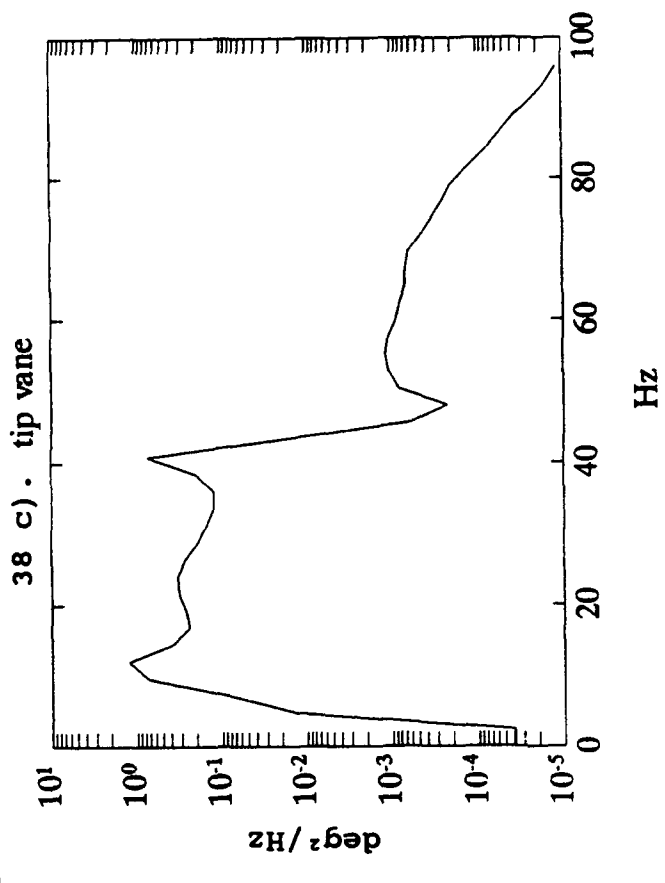
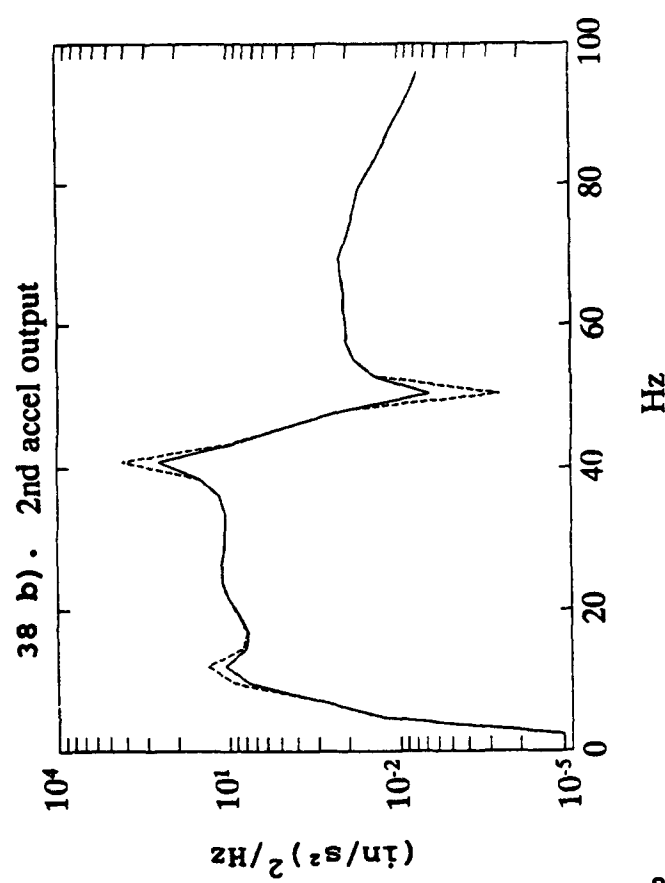
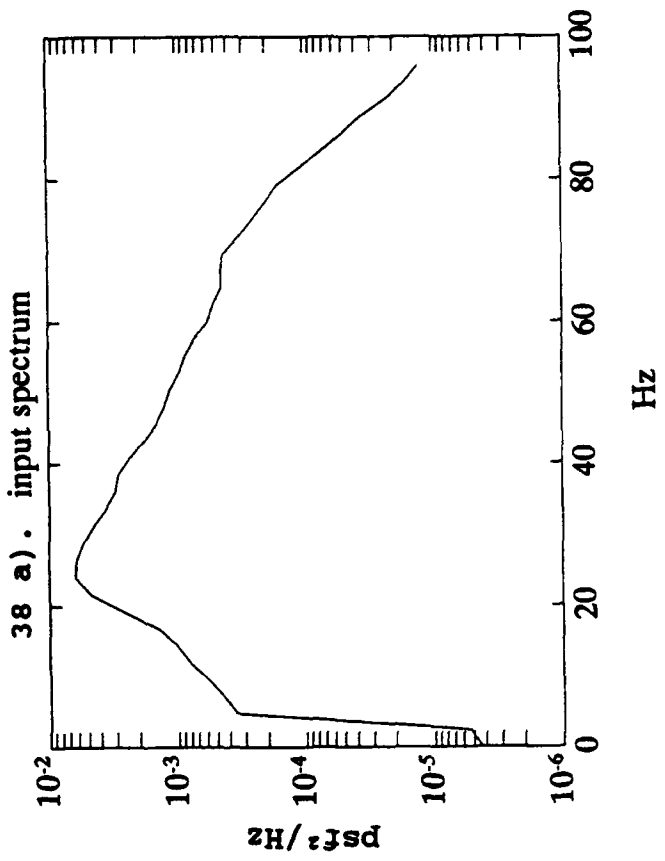


Figure 38. Input and response PSD's for tip-vane control of buffeting of F-15 fin at  $\alpha = 22^\circ$ ,  $q_\infty = 245$  psf. Dashed A2 acceleration curve is open loop, solid curve for a relative feedback gain of 0.1

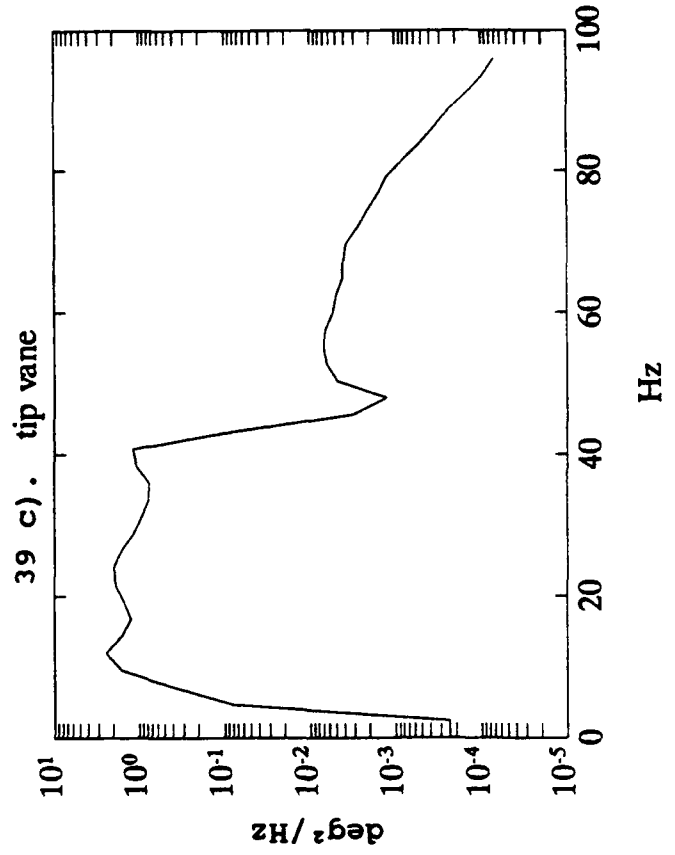
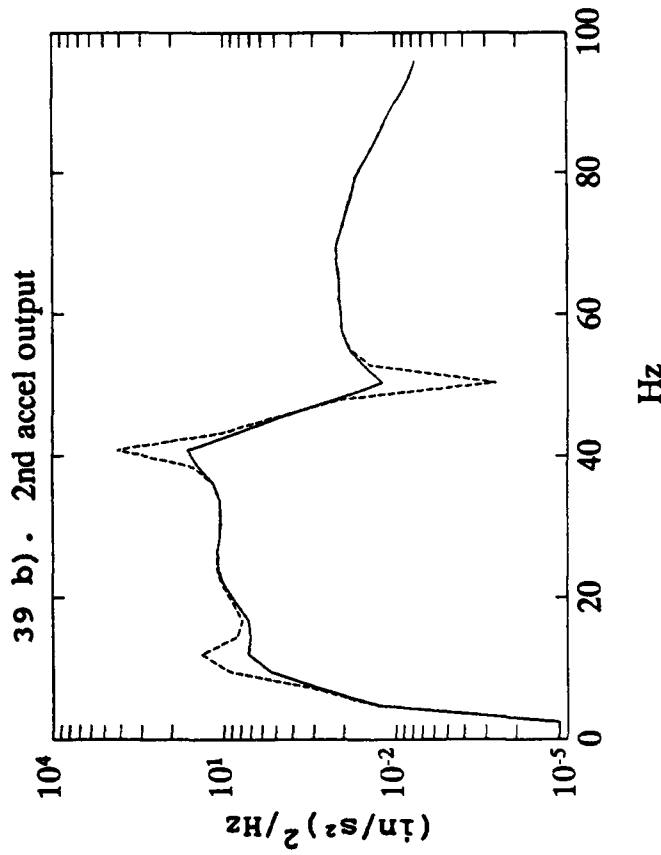
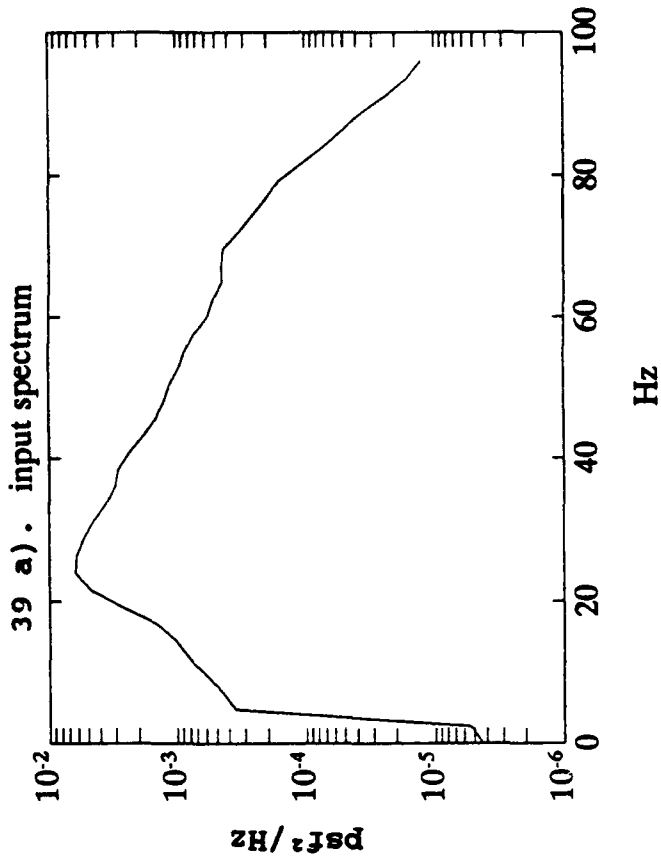


Figure 39. Same as Fig. 38, except feedback gain of 0.25.

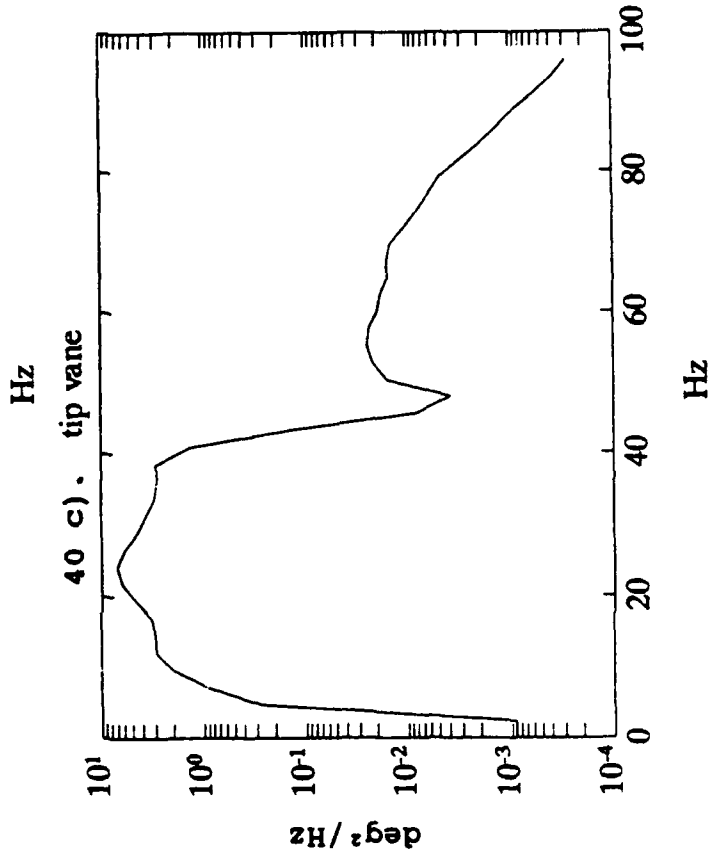
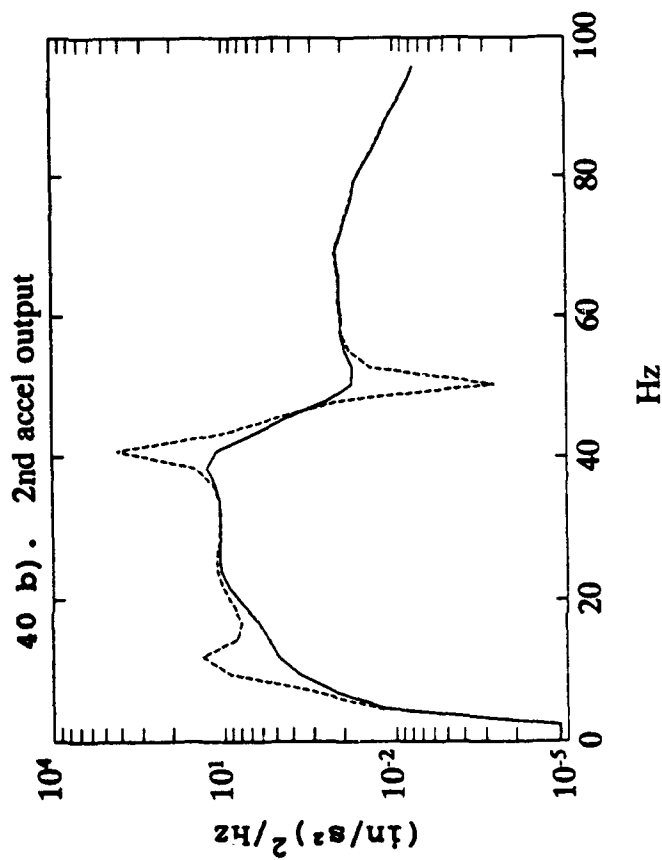
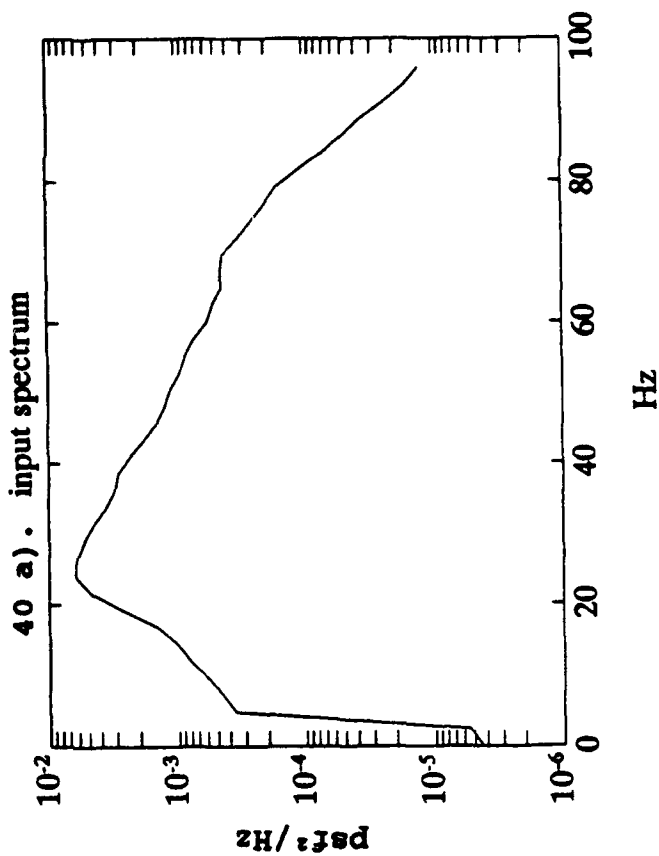


Figure 40. Same as Fig. 38, except feedback gain of 0.5.



satisfactory accomplishment. Admittedly, only one flight condition was here analyzed, and there was no systematic effort to calculate fatigue life. If the present preliminary findings are at all meaningful, one might anticipate that life increases of 0(10) or more might be predicted due to installation of a device even smaller than that shown in Fig. 37.

The conclusions from research on an empennage resembling, in some respects, that of the F-15 are more tentative than for F/A-18. A simple control system feeding back from a single accelerometer to the rudder is unlikely to ameliorate fin buffeting. A more sophisticated system -- probably using more than one sensor -- could perhaps meet the objective, but this has not been demonstrated. On the other hand, a small active vane mounted at the fin tip shows much better promise for response reduction and fatigue-life extension.

All these concluding statements, however, require re-examination. This is because the second mode used herein of free empennage vibration, although based on stiffness & mass data supplied by the manufacturer, does not compare well with what was measured in the laboratory. Only when a more accurate mode shape, displaying substantially larger displacements of the fin/rudder relative to the stabilator, is embodied in the equations of motion can this work on active control be completed with confidence.

## 5.0 CONCLUSIONS AND RECOMMENDATIONS

The most significant finding of this research -- albeit based on theoretical analysis and not yet proven in practice -- is that feedback control has the potential for enhancing the fatigue life of the empennage structure on aircraft designed to operate at high angles of attack. Quite simple control algorithms, employing a single sensor such as a fin-tip accelerometer and driving an existing control surface, are often adequate for the task. Although the theory used in this investigation was conventional and assumed a linear system, the various approximations appear suitable for design purposes. It is believed that the statistical representation of the buffeting input has been improved so as to account, in a more refined way, for partial correlations among the pressures.

The first example treated was an F/A-18 fin/rudder, and its structural dynamic behavior has been successfully modeled. Moderate levels of active rudder control can reduce the RMS root bending moment by over 30%, thus increasing fatigue life by a factor ten or more. A second example -- the F-15 -- apparently cannot have the problem ameliorated by simple rudder control. But a small active tip vane was shown, in a practicable way, to reduce substantially the empennage buffet response. However, the structural dynamic model employed resembled the full-scale structure only qualitatively and needs revision before the F-15 conclusions can be quantified.

The methodology developed here seems capable of adaptation to study active buffet control on other highly-maneuverable, twin-finned aircraft.

Some recommendations for future research:

- o Wind-tunnel tests of aeroelastic models with active control are needed to validate the proposed technology.
- o New twin-finned fighter designs must be analyzed and tested to determine the severity of the buffeting problem. For them active control holds promise as one way of alleviating the response.
- o A general set of analytical tools should be codified and made available to interested users. More sophisticated control theory than that applied here should be included.
- o Methods of structural life estimation, beyond the cumulative damage hypothesis, should be adapted for the empennage buffeting problem. (Reference 15 presents an important effort in this direction for aircraft resembling the F/A-18.)
- o The F-15 plant used herein should be made more accurate, so as to permit active control studies that could be applicable at full scale.

## REFERENCES

1. Triplett, W. E., "Pressure Measurements on Twin Vertical Tails in Buffeting Flow," AFWAL-TR-82-3015, Vols I & II, prepared for USAF Flight Dynamics Laboratory, April 1982.
2. Triplett, W. E., "Pressure Measurements on Twin Vertical Tails in Buffeting Flow," J. Aircraft, Vol. 20, No. 11, November 1983, pp. 920-925.
3. Patel, S. R., "Empennage Dynamic Buffet Loads," briefing by Lockheed-Boeing F-22 Structures A. & I. Team, March 19, 1993.
4. Hebbar S. K., Platzer, M. F., and Liu, Da-M., "Effect of Canard Oscillations on the Vortical Flowfield of a X-31A-Like Fighter Model in Dynamic Motion," AIAA-93-3427-CP, Proceedings, AIAA Applied Aerodynamics Conf., Monterey CA, August 1993, Part 1, pp. 241-250.
5. Lee, B. H. K., et al., "Wind Tunnel Investigation and Flight Tests of Tail Buffet on the CF-18 Aircraft," in Aircraft Dynamic Loads Due to Flow Separation, AGARD-CP-483, NATO Advisory Group for Aerospace Research and Development, Sorrento, Italy, April 1990.
6. Bisplinghoff, R. L., Ashley, H., and Halfman, R. L., Aeroelasticity, Addison-Wesley Publishing Co., Reading MA, 1955.
7. Zimmerman, N. H., Ferman, M. A., and Yurkovich, R. N., "Prediction of Tail Buffet Loads for Design Application," Rept. 89-1378-CP, presented at AIAA et al. 30th Structures, Structural Dynamics and Materials Conf., Mobile AL, April 1989, pp. 1911-19.
8. Lan, C. E., et al., "Investigation of Empennage Buffeting," NASA CR-176973, January 1986; Lan, C. E. and Lee, I. G., "An Investigation of Empennage Buffeting," Status Report on NASA Grant NAG2-371, September 1985-January 1986.
9. Rodden, W. P., and Albano, E., "A Doublet-Lattice Method for Calculating Lift Distributions on Oscillating Surfaces in Subsonic Flows," AIAA Journal, Vol. 7, No. 2, 1969, pp. 279-285.
10. Meirovitch, L., Elements of Vibration Analysis, 2nd Ed., McGraw-Hill Book Co., New York, 1986.
11. Zimmerman, N. H., and Ferman, M. A., "Prediction of Tail Buffet Loads for Design Application," Vols. I and II, Rept. No. NADC-88043-60, July 1987.
12. Bryson, A. E., and Ho, Y. C., Applied Optimal Control, Blaisdell, Waltham MA, 1969.

13. Franklin, G. F., Powell, J. D., and Emami-Naeini, A., Feedback Control of Dynamic Systems, Addison-Wesley Publishing Co., Reading MA, 1986.
14. Bisplinghoff, R. L., and Ashley, H., Principles of Aeroelasticity, reprinted by Dover Publications, NY, 1975.
15. Harbison, S. T., et al., "Development of Techniques for Incorporating Buffet Loads in Fatigue Design Spectra," Vols. I - II, Rept. No. NADC-90071-60, prepared for Naval Air Development Center, Warminster PA, March 1990.
16. Miner, M. A., "Cumulative Damage in Fatigue, " Journal of Applied Mechanics, Vol. 12, A159, 1945.
17. Lee, B. H. K., and Brown, D., "Wind Tunnel Studies of F/A-18 Tail Buffet," J. Aircraft, Vol. 29, No. 1, January-February 1992, pp. 146-152.
18. Houbolt, J. C., Steiner, R., and Pratt, K. G., "Dynamic Response of Airplanes to Atmospheric Turbulence Including Flight Data on Input and Response," NASA Technical Report R-199, June 1964.
19. Lee, B. H. K., and Tang, F. C., "Buffet Load Measurements on an F/A-18 Vertical Fin at High Angle of Attack," AIAA 92-2127-CP, copyright 1992 by American Institute of Aeronautics & Astronautics.
20. Dowell, E. H., et al., A Modern Course in Aeroelasticity, 2nd Ed., Kluwer Academic Publishers, Dordrecht, 1989.
21. Mabey, D. G., "Buffeting Criteria for a Systematic Series of Wings," J. Aircraft, Vol. 26, No. 6, June 1989, pp. 576-582.
22. Edwards, J. W., "Assessment of Computational Prediction of Tail Buffeting," NASA Technical Memorandum 101613, January 1990.
23. Schiff, L. B., et al., "Numerical Simulation of High-Incidence Flow over the Isolated F-18 Fuselage Forebody," J. Aircraft, Vol. 28, No. 11, October 1991, pp. 609-617.
24. Ghaffari, F., et al., "Navier-Stokes Solutions About the F/A-18 Forebody-Leading-Edge Extension Configuration," J. Aircraft, Vol. 27, No. 9, September 1990, pp. 737-748.
25. Ghaffari, F., et al., "Multiblock Navier-Stokes Solutions About the F/A-18 Wing-LEX-Fuselage Configuration," J. Aircraft, Vol. 30, No. 3, June 1993, pp. 293-303.
26. Modiano, D. L., and Murman, E. M., "Adaptive Computations of Flow Around a Delta Wing with Vortex Breakdown," AIAA-93-

3400-CP, Proceedings, AIAA Applied Aerodynamics Conf., Monterey, CA, August 1993, Part 1, pp. 1-9.

27. Kandil, O. A., et al., "Simulation of Tail Buffet Using Delta-Wing/Vertical Tail Configuration," pp. 82-83 of Wynne, E. C., Ed., Structural Dynamics Division Research and Technology Accomplishments for F.Y. 1992 and Plans for F.Y. 1993, NASA Langley Research Center, T.M. 107713, January 1993.
28. Vortex Flow Aerodynamics, AGARD-CP-494, NATO Advisory Group for Aerospace Research and Development; Symposium held in Scheveningen, The Netherlands, October 1990.
29. Panton, R. L., "The Effects of a Contoured Apex on Vortex Breakdown," AIAA 89-0193, presented at 27th Aerospace Sciences Meeting, Reno NV, January 1989.
30. Towfighi, J., and Rockwell, D., "Instantaneous Structure of Vortex Breakdown on a Delta Wing via Particle Image Velocimetry," AIAA Journal, Vol. 31, No. 6, June 1993, pp. 1160-1162.
31. Thompson, S. A., Batill, S. M., and Nelson, R. C., "Separated Flowfield on a Slender Wing Undergoing Transient Pitching Motions," J. Aircraft, Vol. 28, No. 8, August 1991, pp. 489-495.
32. Komerath, N. M., et al., "Flow over a Twin-Tailed Aircraft at Angle of Attack: Part I: Spatial Characteristics," J. Aircraft, Vol. 29, No. 3, May-June 1992, pp. 413-420.
33. Laschka, B., and Breitsamter, C., "A Contribution to the Phenomenon of Fin Buffeting for Vortex Dominated Aircraft Configurations," Report of Institute for Fluid Mechanics, Technical University Munich, 1992.
34. Soltani, M. R., Bragg, M. B., and Brandon, J. M., "Measurements on an Oscillating 70-Deg. Delta Wing in Subsonic Flow," J. Aircraft, Vol. 20, No. 3, March 1990, pp. 211-217.
35. Fisher, D. F., Del Frate, J. H., and Richwine, D. M., "Inflight Visualization Characteristics of the NASA F-18 High Alpha Research Vehicle at High Angles of Attack," NASA-TM 4193, May 1990.
36. Lan, C. E., "The Unsteady Suction Analogy and Applications," AIAA Journal, Vol. 20, No. 12, December 1982, pp. 1647-1656.
37. Lee, B. H. K., and Dunlavy, S., "Statistical Prediction of Maximum Buffet Loads on the F/A-18 Vertical Fin," J. Aircraft, Engineering Note, Vol. 29, No. 4, April 1992, pp. 734-736.

38. Martin, C. A., and Thompson, D. H., "Scale Model Measurements of Fin Buffet Due to Vortex Bursting on F/A-18," in Manoeuvring Aerodynamics, AGARD-CP-497, Toulouse, France, May 1991, pp. 12-1 - 12-10.
39. Moss, S. W., Cole, S. R., and Doggett, Jr., R. V., "Some Subsonic and Transonic Buffet Characteristics of the Twin-Vertical-Tails of a Fighter Airplane Configuration," AIAA Paper No. 91-1049, AIAA/ASME/ASCE/AHS/ASC 32nd Structures, Structural Dynamics and Materials Conference, Baltimore MD, April 1991.
40. Mabey, D. G., and Cripps, B. E., "Some Measurements of Buffeting on a Flutter Model of a Typical Strike Aircraft," AGARD-CP-339, Ground/Flight Test Techniques and Correlation, Cesme, Turkey, October 1982, pp. 13-1 - 13-9.
41. Shah, G. T., et al., "Effect of Vortex Flow Characteristics on Tail Buffet and High-Angle-of-Attack Aerodynamics of a Twin-tail Fighter Configuration," presented at NASA High- $\alpha$  Technology Conference, NASA Langley Research Center, Hampton VA, November 1990.
42. Washburn, A. E., Jenkins, L. N., and Ferman, M. A., "Experimental Investigation of Vortex-Fin Interaction," AIAA 93-0050, presented at 31st Aerospace Sciences Meeting, Reno NV, January 1993.
43. Meyn, L. A., and James, K. D., "Full Scale Wind Tunnel Studies of F/A-18 Tail Buffet," AIAA 93-3519, presented at Applied Aerodynamics Conf., Monterey CA, August 1993.
44. Malcolm Gerald N., "Forebody Vortex Control - A Progress Review," AIAA-93-3540-CP, Proceedings, AIAA Applied Aerodynamics Conf., Monterey CA, August 1993, Part 2, pp. 1082-1116.
45. Rao, D. M., Puram, C. K., and Shah, G. H., "Vortex Control for Tail Buffet Alleviation on a Twin-Tail Fighter Configuration," paper No. 89-2221, SAE Aerospace Technology Conference and Exposition, Anaheim CA, September 1989.
46. Edinger, L. D., "Design of Elastic Mode Suppression Systems for Ride Quality Improvement," J. Aircraft, Vol. 5, No. 2, March-April 1968, pp. 161-168.
47. Bean, D. E., and Wood, N. J., "An Experimental Investigation of Twin Fin Buffeting and Suppression," AIAA-93-0054, presented at 31st Aerospace Sciences Meeting, Reno NV, January 1993.
48. Gu, W., Robinson, O., and Rockwell, D., "Control of Vortices on a Delta Wing by Leading-Edge Injection," AIAA Journal, Vol. 31, No. 7, July 1993, pp. 1177-1186.

49. Reed, W. H., III, "Active Tail Buffet Alleviation for Twin-Tail Fighter Aircraft," briefing prepared by Dynamic Engineering, Inc., September 11, 1992.
50. Communication from Prof. S. Hanagud, Georgia Institute of Technology, February 1993.



## APPENDIX A

### DERIVATION AND CALCULATION OF SPECTRA OF BUFFETING INPUT PRESSURES AND AIRLOADS

#### A.1 MATHEMATICAL BACKGROUND

By reference to Eqs. (2) and (4), one sees that the buffeting disturbance enters the  $i^{\text{th}}$  modal equation of motion through a term of the form

$$Q_{iD}(t) = \iint_{S_F} \Delta p(x, z, t) \phi_i(x, z) dx dz \quad (A1)$$

Here  $\Delta p$  is the aerodynamic force per unit fin area in the positive  $y$ -direction; although written without a subscript, it here represents only the contribution of turbulence due to vortex bursting. Information on  $\Delta p$  is statistical and published in such papers as Refs. 1, 5 and 7. The fact that most pressure data are given separately for opposite sides of a model fin will be dealt with later.

For the moment, it is observed that fundamental understanding about RMS levels, spatial and temporal correlations of  $\Delta p$  can be obtained from quantities such as

$$R_{kk}(\tau) = \lim_{T \rightarrow \infty} \left\{ \frac{1}{T} \int_0^T \Delta p(x_k, z_k, t) \Delta p(x_k, z_k, t+\tau) dt \right\} \quad (A2)$$

and

$$R_{k\ell}(\tau)$$

(A3)

$$= \lim_{T \rightarrow \infty} \left\{ \frac{1}{T} \int_0^T \Delta p(x_k, z_k, t) \Delta p(x_\ell, z_\ell, t+\tau) dt \right\}$$

Here  $(x_k, z_k)$  and  $(x_\ell, z_\ell)$  are typical observation points on the surface.  $R_{kk}$  and  $R_{k\ell}$  are, respectively, auto- and cross-correlation functions. For a stationary, random process they are independent of the time origin, depending only on the interval  $\tau$  between two measurements. It is readily proved that  $R_{kk}$  is an even function of  $\tau$  and that

$$R_{k\ell}(\tau) = R_{\ell k}(-\tau) \quad (A4)$$

From measurements on the Canadian CF-18 model, a few examples of cross-correlations in the chordwise and spanwise directions can be found in Figs. 34-38 of Ref. 19. They clearly show that the relations among the pressures drop off quite rapidly as the separation increases between two points, thereby throwing into question the conservative assumption of 100% spatial correlation. Most of the published information, however, involves power and cross-spectral densities, calculated digitally from data streams generated by rapid-response instruments. For that reason, and because formulas like Eqs. (8), (9) and (11) are so convenient, PSD's and CSD's will be the objects of choice.

As explained in Subsection 2.4 and based on the useful physical interpretation of Eq. (9), these functions of frequency

are obtained by Fourier transformation of twice  $R_{kk}$  and  $R_{kl}$ :

$$\begin{aligned} \text{PSD}_{kk}(f) &= \int_{-\infty}^{\infty} [2 R_{kk}(\tau)] e^{-2\pi i f \tau} d\tau & (A5) \\ &= 4 \int_0^{\infty} R_{kk}(\tau) \cos(2\pi f \tau) d\tau = \text{PSD}_{kk}(-f) \end{aligned}$$

$$\begin{aligned} \text{CSD}_{kl}(f) &= \int_{-\infty}^{\infty} [2R_{kl}(\tau)] e^{-2\pi i f \tau} d\tau & (A6) \\ &= C_{klR}(f) + iC_{klI}(f) \end{aligned}$$

The PSD is, of course, a real quantity. The CSD is complex, having real & imaginary parts separable as in the last line of Eq. (A6). It can also be proved that

$$\text{CSD}_{kl}(f) = \text{CSD}_{lk}^*(f) \quad (A7)$$

With only PSD's and CSD's available for the buffeting pressures, similar expressions must be worked out for the generalized forces of Eq. (A1). Their power spectra are studied first. In the process, the assumption will be made that spatial integrals over the fin area can be interchanged with the time integration and limiting process involved in the definition of correlation.

$$R_{ii}(\tau) = \lim_{T \rightarrow \infty} \left\{ \frac{1}{T} \int_0^T Q_{iD}(t) Q_{iD}(t+\tau) dt \right\}$$

$$\begin{aligned}
&= \text{Lim}_{T \rightarrow \infty} \left\{ \frac{1}{T} \int_0^T \left[ \iint_{S_F} \Delta p(x, z, t) \phi_i(x, z) dx dz \right] \cdot \right. \\
&\cdot \left. \left[ \iint_{S_F} \Delta p(\xi, \rho, t+\tau) \phi_i(\xi, \rho) d\xi d\rho \right] dt \right\} \quad (A8) \\
&= \iint_{S_F} \iint_{S_F} \phi_i(x, z) \phi_i(\xi, \rho) \left\{ \text{Lim}_{T \rightarrow \infty} \frac{1}{T} \int_0^T \Delta p(x, z, t) \cdot \right. \\
&\cdot \left. \Delta p(\xi, \rho, t+\tau) dt \right\} dx dz d\xi d\rho
\end{aligned}$$

Evidently, the limit inside the braces in the last member of Eq. (A8) is a cross-correlation between pressures expressed as functions of pairs of coordinates  $(x, z)$  and  $(\xi, \rho)$ , which in turn define points that can run over the entire area of the fin. This would be quite impractical to measure. What can be obtained are pressure PSD's/CSD's for a number of discrete locations. This suggests dividing the fin into  $M$  small areas  $\Delta S_k$ , each centered on a measurement point  $(x_k, z_k)$ . By assuming  $\Delta p$  nearly constant over each area, one is led to replace spatial integrals with sums. For example, Eq. (A1) becomes, approximately,

$$Q_{iD}(t) \approx \sum_{k=1}^M \Delta S_k \Delta p_k \phi_{ik} \quad (A9)$$

where the subscripts on  $\Delta p_k$  and  $\phi_{ik}$  associate them with  $(x_k, z_k)$ . Similarly, Eq. (A8) is replaced by

$$R_{ii}(\tau) \tag{A10}$$

$$\equiv \sum_{k=1}^M \sum_{\ell=1}^M \Delta S_k \Delta S_\ell \phi_{ik} \phi_{i\ell} [R_{k\ell}(\tau)]$$

Here  $R_{k\ell}(\tau)$  is the pressure cross-correlation defined by Eq. (A3); when the indices become equal during summation, it is just  $R_{kk}(\tau)$  of Eq. (A2).

After Eq. (A10) is multiplied by 2 and Fourier transformed, the resulting expression in the frequency domain reads

$$\text{PSD } (Q_i(f)) \tag{A11}$$

$$\equiv \sum_{k=1}^M \sum_{\ell=1}^M [\Delta S_k \phi_{ik}] [\Delta S_\ell \phi_{i\ell}] [\text{CSD}_{k\ell}(f)] ,$$

This power spectrum is now written in the notation of Eq. (10), Subsection 2.4. It is worth noting that, in the double summation of Eq. (A11), products of contributions from  $\Delta S_k$  and  $\Delta S_\ell$  (with  $k \neq \ell$ ) appear twice. In view of Eqs. (A6) and (A7), each such pair simplifies as follows:

$$[\Delta S_k \phi_{ik}] [\Delta S_\ell \phi_{i\ell}] [\text{CSD}_{k\ell}(f) + \text{CSD}_{\ell k}(f)] \tag{A12}$$

$$= [\Delta S_k \phi_{ik}] [\Delta S_\ell \phi_{i\ell}] 2C_{k\ell R}(f) ,$$

the imaginary parts having cancelled. Hence Eq. (A11) can also be written

$$\text{PSD } (Q_i(f)) \quad (A13)$$

$$\begin{aligned} &= \sum_{k=1}^M [\Delta S_k \phi_{ik}]^2 [\text{PSD}_{kk}(f)] \\ &+ \underbrace{\sum_{k=1}^M \sum_{\substack{\ell=1 \\ (k \neq \ell)}}^M [\Delta S_k \phi_{ik}][\Delta S_\ell \phi_{i\ell}][C_{k\ell R}(f)]} \end{aligned}$$

Equation (A13) shows the power spectrum of  $Q_{iD}$  to be a real quantity, as expected.

A derivation parallel to the foregoing produces a working approximation for the CSD between any pair of generalized forces. For  $i \neq j$ ,

$$\text{CSD}(Q_i Q_j) \quad (A14)$$

$$= \sum_{k=1}^M \sum_{\ell=1}^M [\Delta S_k \phi_{ik}][\Delta S_\ell \phi_{j\ell}][\text{CSD}_{k\ell}(f)]$$

Since Eq. (A7) can no longer be usefully invoked, the cross-spectra of Eq. (A14) are seen to be complex functions of frequency. It does appear that

$$\text{CSD } (Q_j Q_i) = \text{CSD}^* (Q_i Q_j) , \quad (A15)$$

which has the interesting consequence that the matrix  $[S_Q]$  of Eq. (10) is Hermitian. Note also that, when  $i = j$ , Eq. (A14) reduces

directly to Eq. (A11) or (A13). Hence Eq. (A14) implies all the needed spectra.

Before one turns to the practical determination of approximate inputs for control-system design, it is worth deriving two limiting forms of Eq. (A14).

- 1) 100% spatial correlation among  $\Delta p$ 's over the entire fin. The most straightforward assumption in this case is to write

$$\text{CSD}_{k\ell}(f) = \text{PSD}_{kk}(f) = \text{PSD}_p(f) \quad (\text{A16})$$

for all stations. This implies, of course, not only perfect correlation but a constant RMS level of  $\Delta p$ . It reduces Eq. (A14) to

$$\begin{aligned} \text{CSD}(Q_i Q_j) & \quad (\text{A17}) \\ & \equiv \text{PSD}_p(f) \left[ \begin{array}{c} M \\ \Sigma \\ k=1 \end{array} \Delta S_k \phi_{ik} \right] \left[ \begin{array}{c} M \\ \Sigma \\ \ell=1 \end{array} \Delta S_\ell \phi_{j\ell} \right] \end{aligned}$$

Discussion of spatially variable RMS  $\Delta p$  is necessary, however, since this is actually what occurs. Suppose one chooses a reference station ("REF") on the fin, preferably where the RMS  $\Delta p$  is quite large. Then, for any other station, say  $k$ , perfect correlation should imply

$$\text{PSD}_{kk}(f) = K_k^2 \text{PSD}_{\text{REF}}(f) \quad (\text{A18})$$

By integration over all frequencies, one sees from Eq. (9) that  $K_k^2$  is the ratio of mean-square  $\Delta p$ 's between  $k$  and "REF." Equation (13) of the main text is, therefore, confirmed. More obscure is that the relation

$$CSD_{k\ell}(f) = K_k K_\ell PSD_{REF}(f) \quad (A19)$$

is also implied. It does appear, however, that Eq. (A19) can be proved by Fourier-transforming Eq. (A3) while setting  $\Delta p(t)$  at stations  $k$  and  $\ell$  equal to  $K_k$  and  $K_\ell$ , respectively, times  $\Delta p_{REF}(t)$ . The resulting expressions for the fully-correlated generalized-force spectra are thereby reduced to

$$CSD(Q_i Q_j) \quad (A20)$$

$$\cong PSD_{REF}(f) \left[ \sum_{k=1}^M K_k \Delta S_k \phi_{ik} \right] \left[ \sum_{\ell=1}^M K_\ell \Delta S_\ell \phi_{j\ell} \right]$$

This is essentially Eq. (15) of the main text. It was used in calculations on the F/A-18.

- 2) Zero spatial correlation between pairs of fin stations. In this case, for  $k \neq \ell$ ,

$$CSD_{k\ell}(f) = 0, \quad (A21)$$

so that Eq. (A14) becomes



$$\hat{=} \sum_{k=1}^M [(\Delta S_k)^2 \phi_{ik} \phi_{jk}] [\text{PSD}_{kk}(f)]$$

Equation (A22), in combination with Eq. (A18) above, will be seen to confirm Eq. (16) of the main text.

Numerical treatment of the case of partial spatial correlation is deferred until discussion of the F-15 fin loading below.

#### A.2 EXAMPLE OF THE F/A-18

Application of Eq. (A20) to the F/A-18 was complicated by the forms in which data are available in the literature. Thus Ref. 11 provides PSD's of  $\Delta p$  for five stations on the fin at  $\alpha = 32^\circ$  (here reproduced as Fig. 14) and PSD's for the single central station at eight values of  $\alpha$  (here reproduced as Fig. 15). On the other hand, Ref. 5 reports a program of measurement involving 24 locations on the CF-18 model fin (see Fig. 8 of that paper for details). However, on their Figs. 23 and 24 for the single  $\alpha = 30^\circ$ , Ref. 5 plots RMS pressures on just the inboard and outboard surfaces of the fin separately.

After careful study, it was decided here to take a reference spectrum for  $\Delta p$  from Ref. 11 and to require their five  $\Delta p$  spectra at one  $\alpha$  to serve as a check for calculations based on the finer

grid with  $M = 24$  available from Ref. 5 and the other Canadian publications. One important assumption underlies this approach: that the pressure perturbations are instantaneously  $180^\circ$  out of phase between opposite inboard and outboard stations. This would certainly be true of the time-dependent pressures if it were a case of small-disturbance potential flow (cf. Chap. 5 of Ref. 6). Since the instantaneous  $[p(t)-p_\infty]$  would then be equal and opposite, however, the RMS values would also be equal at opposite stations, and Figs. 23-24 of Ref. 5 indicate that this is not exactly correct. Nevertheless, this approximation is justified by other evidence. Lacking a more rigorous alternative, anticorrelation is assumed.

The Ref. 5 data are given in terms of pressure coefficients. In general, if the pressure force is positive outward,

$$\Delta p(t) = q_\infty [C_{pI}(t) - C_{pO}(t)] , \quad (A23)$$

where the subscripts refer to inboard and outboard fin surfaces. Now, for anticorrelated disturbances,

$$C_{pI} = -kC_{pO} \quad (A24)$$

By squaring Eq. (A23), substituting Eq. (A24) and averaging over time, one is led to the mean-square relation

$$\overline{\Delta p^2} = q_\infty^2 (k + 1)^2 [\overline{C_{pO}^2}] \quad (A25)$$

Correspondingly, for the RMS values

$$\Delta P_{RMS} = q_{\infty} [C_{pIRMS} + C_{pORMS}] \quad (A26)$$

Space limitations prevent reproduction of all the tedious but straightforward details involved in the numerical application of Eqs. (A18), (A19) and (A20). As a reference spectrum\*, that shown nondimensionally in Fig. 2 was chosen for  $\alpha = 32^\circ$ . Although the Ref. 5 data are for  $\alpha = 30^\circ$ , these angles of attack are believed close enough not to invalidate the work.

Areas  $\Delta S_k$  were derived, at full scale, for points corresponding to the 24 measurement stations of Ref. 5. Modal amplitudes  $\phi_{ik}$  were computed from the same power series used with LATIS1 to find the  $\bar{A}_{ij}$ . The coefficients  $K_k$  followed from applying Eq. (A26) to numbers read from Figs. 23 & 24, Ref. 5, multiplying by  $q_{\infty}$  and dividing by the reference RMS  $\Delta p$ , which was 0.0174 psi on the McDonnell model (at  $q_{\infty} = 7.5$  psf.). The aforementioned direct proportionality of all pressures to  $q_{\infty}$  was invoked when determining PSD's/CSD's of the dimensional generalized forces for control-system design at full scale. The final numerical results are those given in Eqs. (34) & (35) of the main text.

It must be emphasized that the numerical precision of the process just described definitely does not justify the four

---

\*Reference spectra and RMS  $\Delta p$  levels for other  $\alpha$ 's, used in the structural life estimations, were taken directly from Fig. 15.

decimal places quoted. For example, the Ref. 5 figures could be read only with some uncertainty in the third decimal place. More significant are the results of a comparison attempted between the direct  $\Delta p$  data of Ref. 11 (at 12%-scale) and the data of Ref. 5 (at 6%-scale). In Table A1 are listed, for the five fin stations tested in the former report, the values of coefficient  $K_k$ . The adjacent column gives corresponding coefficients interpolated from Ref. 11 and embodying the Eq. (A26) approximation.

Table A1

Dimensionless RMS  $\Delta p$ 's from Ref. 11,  
 along with estimated corresponding  
 quantities from Ref. 5.  
 $\alpha = 32^\circ$ ,  $q_\infty = 7.5$  psf.

Station	% Chord	% Span	$K_k$ (Ref. 11)	Est. $K_k$ (Ref. 5)
1	45	30	0.796	0.58
2 (REF)	45	60	0.968	0.58 <sub>5</sub>
3	45	90	0.690	0.46
4	10	60	1.363	0.56
5	80	60	0.746	0.56

Incidentally, it was also possible to compare the  $K_k$  at Station 2 for values of  $q_\infty$  from 3.0 to 11.5. They increased from 0.918 to 0.991, the last number being the one equated to unity for the reference spectrum. Over the 24 Ref. 5 stations,  $K_k$  ranged from 0.387 to 0.813, the latter quantity appearing to be an "outlier."

Faced with Table A1, the only comment one can make is that scale differences, measurement inaccuracies and other sources of approximation render the analytical estimation of absolute buffet

response levels a very imprecise undertaking. It is worth repeating, however, that the relative consequences of introducing active control of this response are felt to be predictable with considerably greater confidence.

### A.3 EXAMPLE OF THE F-15.

As discussed in the main text, Vol. II of Ref. 1 is the source for extensive PSD data and some CSD data, taken at  $\alpha = 22^\circ$ ,  $q_\infty = 12$  psf, on a 13%-scale model. Figure 41 shows the locations of 78 high-frequency-response pressure transducers, installed in inboard and outboard pairs as close as possible to one another on the fin. Figures 103 through 178\*, Ref. 1, plot one-sided PSD's for these stations on a "rigid" structure. Although the curves display some "noise" and a few instrument-related spikes at 60 Hz, by careful drafting one can construct the anticipated smooth spectra from all of them. These spectra are remarkably consistent in shape, and nearly all have a well-defined peak slightly above 30 Hz.

Located at 3% of the chord and 78%-span, station #7 outboard (marked on the figure) was chosen for reference purposes. Smoothed data from there appear on Figs. 31 & 32 above. In order to proceed with generalized-force calculation, it is again necessary to presume that the inboard and outboard pressures are anticorrelated. Figure 201e of Ref. 1 is one source of support for this hypothesis. It graphs the phase angle of the CSD be-  
\*Two channels are missing.

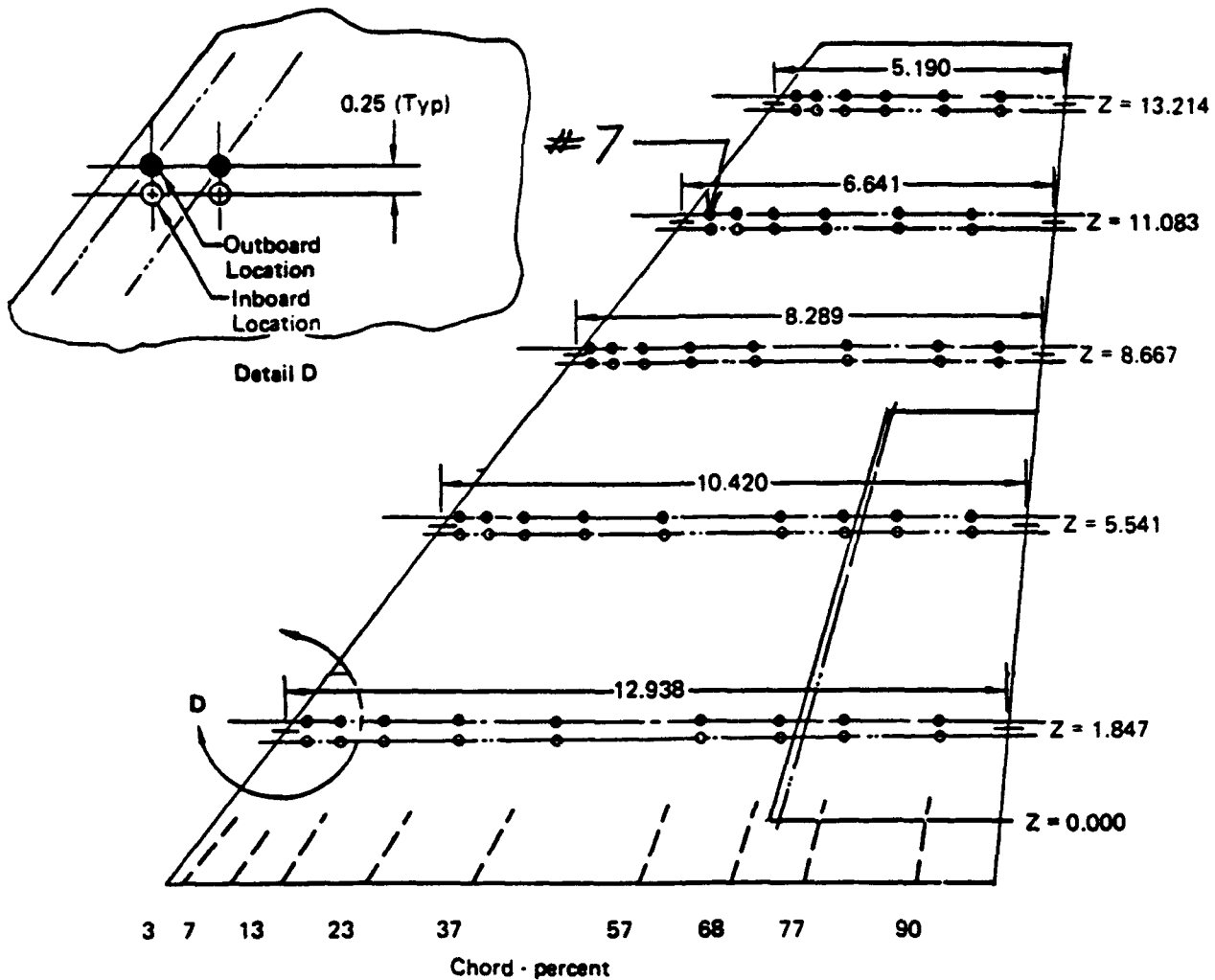


Figure 41. Pressure transducer locations on a 13% scale model of F-15 fin/rudder. (Dimensions are in inches except for percent-chord lines. A few sensor locations very close to the leading edge are omitted.)

ween two opposite stations bracketing the 7%-chord, 78%-span location. At  $f = 0$ , the plot starts from  $180^\circ$ , but above about 8 Hz it drops into the range  $140^\circ - 150^\circ$ . Noting that the cosines of  $180^\circ$  and  $150^\circ$  differ by less than 14%, one concludes that retaining the  $180^\circ$  approximation over the whole frequency range may not be inconsistent with many other simplifications common to research on buffet response.

Since the RMS level of pressure is furnished with each PSD plot, it would be an easy matter to compute  $39 K_k$  from Eq. (A18). The fully-correlated or uncorrelated generalized-force spectra would then follow immediately from Eq. (A20) or (A22), respectively. It was regarded as a matter of interest, however, to allow for partial correlation on F-15. This requires studying how Eqs. (A13) and (A14) can be adapted for active control purposes.

As written, and if all needed data were at hand, Eqs. (A13)-(A14) involve complicated functions of frequency (or reduced frequency) that are different for each  $i, j$  combination. There are 16 of these, which reduces to 10 because of the Hermitian property of the matrix  $[S_Q]$ . As a preliminary,  $39 K_k$  &  $\Delta S_k$ , along with  $4 \times 39$  modal amplitudes  $\phi_{ik}$ , were determined at the known set of pressure stations. The dimensionless factors in Eq. (A20) were found to have the following values

i	$\sum_{k=1}^{39} K_k \phi_{ik} \frac{\Delta S_k}{S_F}$
1	0.3407
2	0.01302
3	0.1001
4	0.02014

The small number here for  $i = 2$  is, incidentally, a warning that the second mode will not play as large a role in the present analysis as it should and did on the full-scale F-15.

Turning to partial correlation, the additional information available from Ref. 1 is as follows: for the outboard row of transducers at 78%-span, complete CSD's between the second station chordwise and five stations lying behind it. For each of these CSD's there are plots of magnitude, phase angle, real part and imaginary part. No CSD's are provided between transducers in different chordwise rows. There is, therefore, a presumption that these rows are uncorrelated. It is supported by the physical nature of the turbulent flow and to some degree by evidence such as the correlations on Figs. 35 & 38 of Ref. 19.

Given this very incomplete state of knowledge, it was decided to neglect all inter-row correlations and to assume that in each row the chordwise CSD's varied with distance  $x$  in the same way as they do at 78%-span. For use in Eq. (A13), these assumptions permit the real parts  $C_{kQR}(f)$  to be worked out straightforwardly. For Eq. (A14), the notation was adopted



$$\text{CSD}_{k\ell}(f) = |\text{CSD}_{k\ell}(f)| \exp(i\theta_{k\ell}(f)) \quad (\text{A27})$$

The next step in simplification was to normalize the spectrum  $\text{PSD}_{\text{REF}}(f)$  from Station #7. For other stations, the relations were assumed:

$$\text{PSD}_{kk}(f) \cong K_k^2 \text{PSD}_{\text{REF}}(f) \quad (\text{A28})$$

and

$$\text{CSD}_{k\ell}(f) \cong K_{k\ell}^2 [\text{PSD}_{\text{REF}}(f)] \exp(i\theta_{k\ell}(f)) , \quad (\text{A29})$$

with

$$\text{CSD}_{k\ell}(f) = 0 \quad (\text{A30})$$

when  $k, \ell$  are not in the same chordwise row. It follows from Eq. (A29) that

$$|\text{CSD}_{k\ell}(f)| = K_{k\ell}^2 [\text{PSD}_{\text{REF}}(f)] \quad (\text{A31})$$

Also the relation

$$\text{CSD}_{\ell k}(f) = \text{CSD}_{k\ell}^*(f) \quad (\text{A32})$$

proved helpful when  $k$  and  $\ell$  were interchanged in summations.

Study of the plots of phase angle  $\theta_{k\ell}$  vs.  $f$  suggested that, for  $k \neq \ell$ , this quantity varies linearly with frequency, with the slope of the variation almost linearly dependent on the

separation  $[x_\ell - x_k]$ . From the 78%-span data, it was estimated that

$$\frac{d\Phi_{k\ell}}{df} \equiv \begin{cases} 0 & , (x_\ell - x_k) < 4 \\ 0.068 (x_\ell - x_k - 4) & , (x_\ell - x_k) \geq 4 \end{cases} \quad (\text{A33})$$

(Distances are in inches on the model.) This formula was used for all chordwise rows.

Figures  $K_{k\ell}^2$  in Eq. (A31) were calculated by taking the area under each side from  $f = 0$  to  $\infty$ . With the normalized area under  $[\text{PSD}_{\text{REF}}(f)]$  equal to unity, so that  $K_{kk} = K_{77} = 1$ , the process led to the following sequence of  $K_k$  values for that row: 1, 0.609, 0.256, 0.232, 0.217, 0.179 and 0.1415. From these and Eq. (A33), CSD properties were estimated for the other four rows in Fig. 41.

Given all the foregoing, it was tedious but feasible to work out the PSD's and CSD's by means of Eqs. (A13) and (A14), respectively. Close examination shows that each  $\text{PSD}(Q_i(f))$  will equal a constant times the reference spectrum of Eqs. (A28) and (A31). Retention of the phase angles in Eq. (A29), however, complicated the  $\text{CSD}(Q_i Q_j)$  and proved unacceptable to the control-system designer. Therefore, as a final approximation for the purposes of this report, each  $\Phi_{k\ell}(f)$  was replaced by its constant value at the peak of the graph of the corresponding  $|\text{CSD}_{k\ell}(f)|$  vs. frequency. Thus the cross spectra retained their complex property, but only in an averaged sense.

While avoiding the reproduction here of numerous tables and graphs, it is hoped that the foregoing provides adequate understanding of how the buffeting inputs were handled for Subsection 4.2.

## APPENDIX B

### SUMMARY OF PRIOR AND CONCURRENT RESEARCH

#### B.1 PAST EXPERIENCE WITH BUFFETING

In this Appendix designed to review the literature, it is useful to begin with some repetition of previous discussion. As described in the classical texts on loads and aeroelasticity (e.g., Ref. 6, pages 8, 626; Ref. 20, pages 336-348, 411), "buffeting" generally is a phenomenon of forced response at intermediate to high angles of attack, where turbulent separated flow from a partially-stalled lifting surface or bridge cross section, etc., produces time-dependent loading on that surface itself or on a rearward surface like a stabilizer in the turbulent wake. Although nearly as old as manned aviation -- since every stall produces some "shaking" -- buffeting began to stand out as a systematic operational issue for the highly-maneuverable fighters of World War II. Many of these machines were capable of sustaining locally transonic flow conditions on upper surfaces near the center section of their wings. The resulting shock waves could produce significant amounts of separation even at moderate angles of attack. The associated time-dependent airloads generated vibrations that could be sensed by the pilot. An even more disturbing situation arose when the separated wake was able to pass across the horizontal stabilizer and elevator. There was a direct cable connection between the latter and the control stick so that the pilot became aware of buffeting through stick shaking as well as the overall airframe response.

When this problem was encountered, a flight test (or wind-tunnel) program was often conducted with the vehicle flown at various combinations of Mach number, angle of attack and normal load factor. Thus isolines of buffet severity could be constructed, and these were usually plotted on a diagram of lift coefficient vs. flight Mach number or speed (the recent Ref. 21 contains many examples in its Figs. 3-8 for swept wings). Sometimes such testing would result in the specification of regions in the flight envelope which should be avoided -- or entered only under unusual or emergency circumstances -- because the associated shaking might lead to loss of control or damage to the vehicle. It is worth noting, however, that the "transonic buffet" just described never caused major structural failure and was rarely a significant source of fatigue damage.

By contrast, the sort of buffeting envisioned in the present research constitutes a threat to the structural integrity of the affected aircraft and surely cannot be avoided by "red-lining" the flight or performance envelope. For a whole generation of modern fighters, several operational advantages have been well demonstrated which are associated with controlled flight at  $\alpha$  near or exceeding maximum lift. Canard as well as conventional aft control surfaces are sometimes employed. More importantly the wings of these aircraft have highly-sweptback leading edges adjacent to the fuselage intersection. Most are also fitted with chines or leading-edge extensions (LEX). A key feature of such wings is that, at angles above a few degrees, boundary-layers

flowing off the leading edges and LEX-fuselage combination give rise to one or more pairs of counter-rotating vortices. These vortices grow in strength with increasing angle. They remain stable and well-defined up to angles in a range between about  $20^{\circ}$  and  $30^{\circ}$  depending on aspect ratio and details of the LEX/leading edge arrangement. Their presence causes a nonlinear enhancement of lift which is especially significant for combat maneuverability.

As can be inferred from figures reproduced in the next subsection, the vortex system can pass close to twin dorsal fins and induce dynamic loads thereon at angles of attack as low as  $10^{\circ}$ . These loads become progressively more severe with increasing angle, however, and their peak range is associated with a phenomenon called "bursting." This results from a vortex instability whose consequence is a "bubble" or substantially enlarged volume of violently turbulent fluid motion.

## B.2 MEASUREMENT AND PREDICTION OF THE FLOWFIELD ABOVE SWEPTBACK WINGS AT HIGH $\alpha$

The vortex flowfield above swept and delta lifting surfaces, the location of bursting and the subsequent turbulent motion responsible for buffeting have been subjects of widespread research interest. With considerable overlap in individual cases, this work can be divided between theoretical predictions and experimental measurements in flight, wind and water tunnels. As for the former, up to year 1990 they were the focus of a definitive survey performed for NATO AGARD by Edwards (Ref. 22).

Although he also discusses some experimental investigations and summarizes buffet response prediction, the majority of the Ref. 22 literature citations involve computational fluid dynamic (CFD) studies based on Euler or approximate Navier-Stokes equations of motion.

Typical of more recent CFD research are publications by Schiff et al. (Ref. 23); Ghaffari et al. (Refs. 24, 25); and Modiano & Murman (Ref. 26). References 23-25 deal with the F/A-18 forebody and forward wing, whereas Ref. 26 concerns an isolated delta wing and carries Euler calculations up to  $\alpha = 52^\circ$ . See also Kandil (Ref. 27). Apparently in most cases these and other studies are quite successful when simulating the pre-burst vortex structure and burst location, but quantitative details within the burst region have proved elusive. The present authors regret that space limitations prevent them from reproducing some of the very interesting results, such as the colored illustrations in Ref. 25.

Reference 22 undertook to quantify the computational demands for wholly theoretical response predictions. Based on the CRAY 2 as representative of the then-current class of mainframes, Edwards anticipated a "three order of magnitude decrease in computer runtime" required to bring such predictions down to feasible size. Whereas such computer improvements are perhaps within sight in 1993, it is no surprise that all response analyses to date have relied on experimental data rather than CFD for the pressure inputs.

Regarding laboratory measurements of buffet-related flow-fields, it is impossible here to do justice even to those programs which focus on the problem of twin vertical tails. An indication of numbers is furnished by the over twenty relevant papers, dealing with steady & unsteady boundary conditions on wings & bodies, which appeared just in one AGARD vortex symposium (Ref. 28). References 29 and 30 are typical of experiments on delta and related lifting surfaces in water channels at chord Reynolds Nos. of  $0 (10^4)$ . Similarly, one can cite Refs. 31-33 for measurements in air by various techniques, not to speak of several other publications (e.g., by Nelson and colleagues).

Since the Reynolds Nos. differ so markedly among these studies, a legitimate question concerns how great is the influence of this parameter on velocity fields, pressures on submerged bodies, etc. There seems to exist a consensus that its effects are negligibly small in view of the overall complexity of the buffet phenomenon. One should point, however, to a lack of unanimity. Thus on deltas in unsteady motion, Soltani et al. (Ref. 34) report significant changes in resultant aerodynamic loads when  $Re$  is increased from 1.0 to  $1.87 \times 10^6$ . As for Mach No. effects in the fin buffet regime, they are clearly rather unimportant because, at the  $\alpha$ 's of interest, maneuvering aircraft would experience destructively large normal loads above  $M = 0.5$  or so.

In the context of flow visualization, one should further



mention the full-scale data that are among the products of the interagency High Angle-of-Attack Research Vehicle (HARV) program. Reference 35 provides an early example of HARV flowfield depictions, which also appear in Ref. 28 and elsewhere.

Laschka and Breitsamter (Ref. 33) is used here as a vehicle for discussion of the relationship between flow velocities and pressures on the buffeting fins. Their paper is believed to be the first attempt to use hot-wire anemometers and collect detailed data on time-dependent flow velocities throughout the vortical turbulent field. Reference 33 employs a rather generic delta-wing model, with no LEX but a canard stabilizer and a single center-line fin. Measurements are reported up to  $\alpha = 30^\circ$  over the entire surface of a single plane of observation, Fig. 42, normal to the fuselage axis and located near the trailing edge of the fin root. The  $\alpha$ -range employed is more representa-

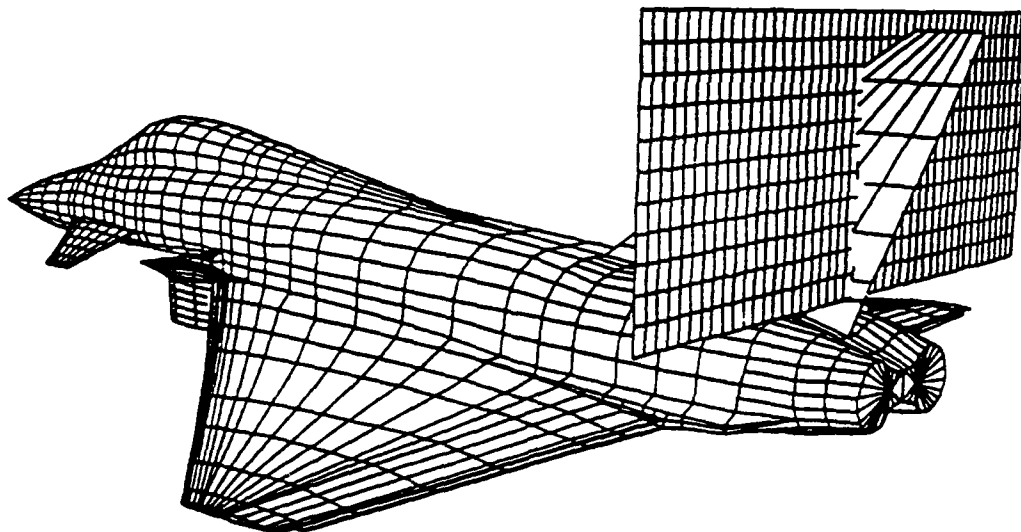


Figure 42. Location of the measurement plane. (Figure 3 of Ref. 33).

tive of F-15 than F/A-18, but the plane extends far enough laterally to encompass the positions of typical twin fins.

Flow measurements include three components of mean velocity, RMS values of all fluctuating components, and power spectra of certain components. These last are of special interest, because they display a fairly "peaky" spectrum which can be compared with those of turbulent pressures on fins available from the literature for both F-15 and F/A-18 (cf. Fig. 2 and Section 4). As one example of this correlation, the PSD's of lateral velocity at  $\alpha = 28^\circ$  and stations pertinent to the F-15 fin locations show maxima near Strouhal Nos. of 0.6 - 0.8, based on free-stream speed and wing mean aerodynamic chord. This agrees well with the experimental value of 0.6 which RANN, INC. chose to model pressure inputs for F/A-18 fin buffeting in the  $\alpha = 30^\circ$  range.

Figure 43 reproduces the Ref. 33 mean crossflow velocity vectors for three angles of attack. At  $\alpha = 15^\circ$  the small, unburst vortex can be seen quite far inboard. But when  $\alpha = 30^\circ$  is examined one can easily identify the large volumes occupied by what is a highly unsteady turbulent flow. Even more interesting among many measurements are the dimensionless root-mean-square (RMS) components such as the spanwise  $\sqrt{v'^2}/U_\infty$ , shown for five  $\alpha$ 's in Fig. 44. The numbers on the contours are in percent, and maximum values near 12% occur near the typical fin locations. Even though the streamwise velocity components  $u$  are found in Ref. 33 to be somewhat lower than the free-stream  $U_\infty = 40$  m/s, one can still infer that the local time-dependent angles of

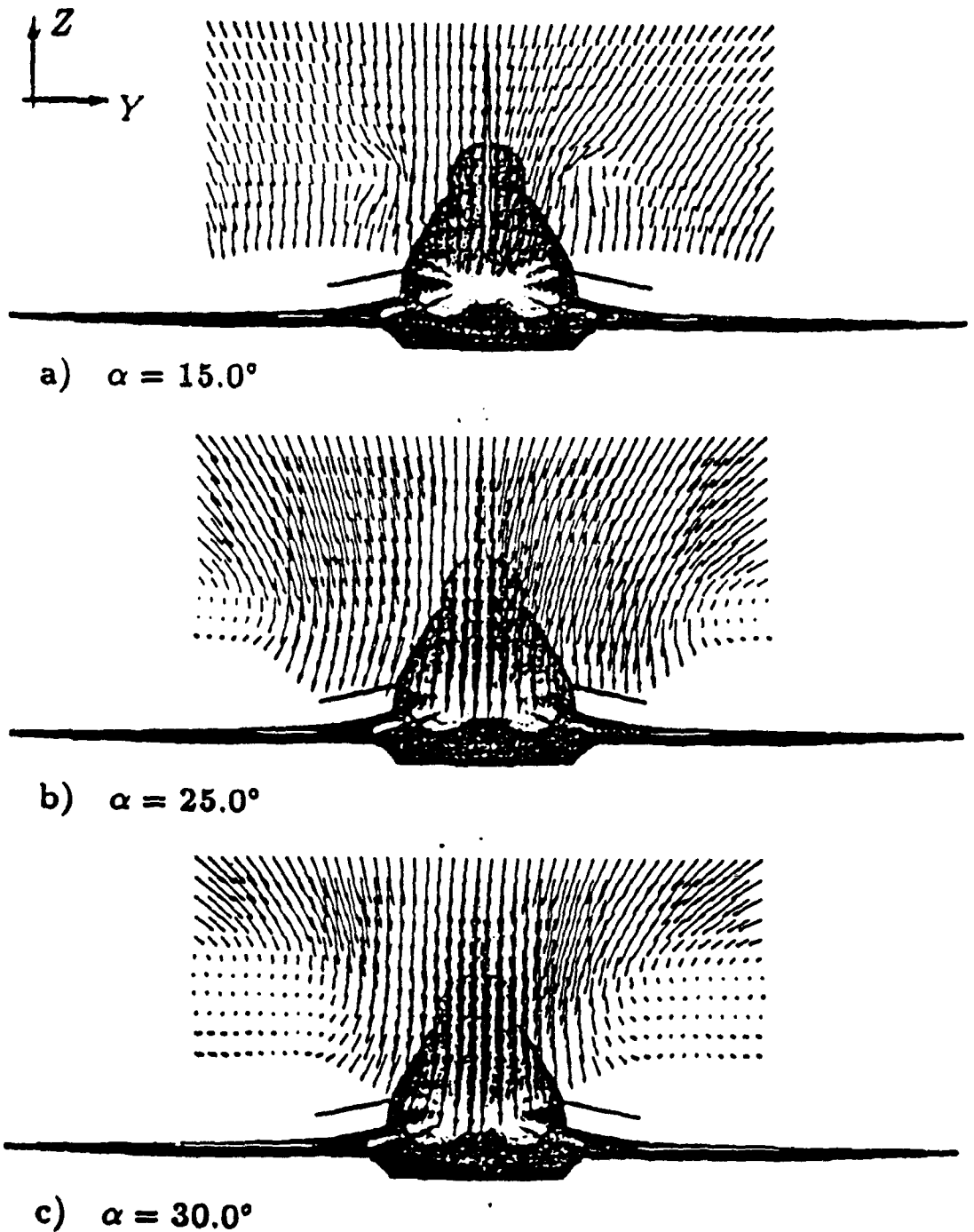
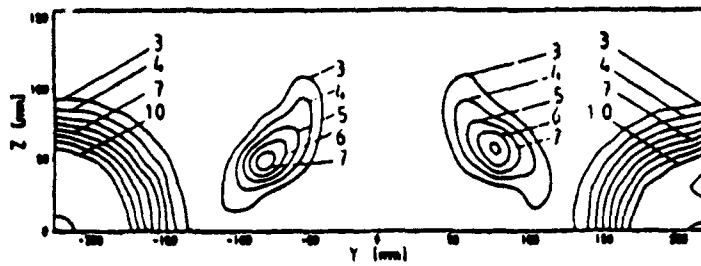
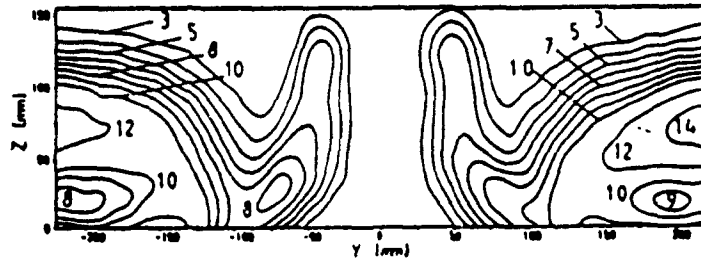


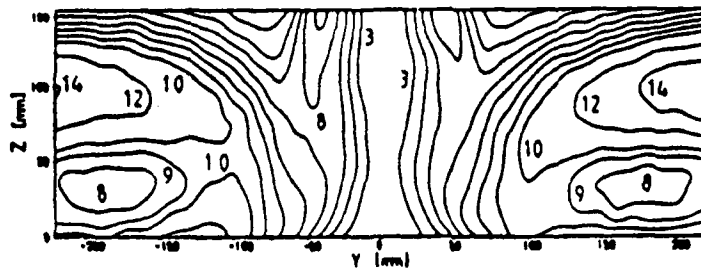
Figure 43. Velocity vector  $|u_{yz}|$  in the measurement plane at  $\alpha = 15.0^\circ$ ,  $\alpha = 25.0^\circ$  and  $\alpha = 30.0^\circ$ ;  $Re = 1.0 \times 10^6$ .  
 (Adapted from Fig. 4 of Ref. 33.)



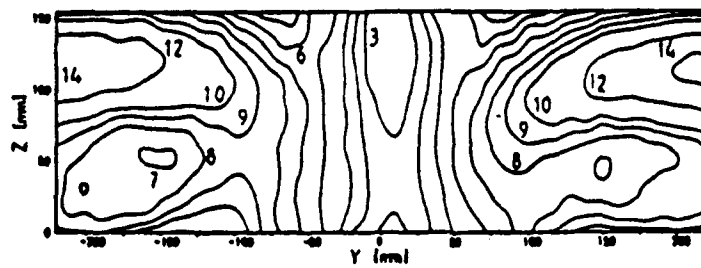
b)  $\alpha = 20.0^\circ$



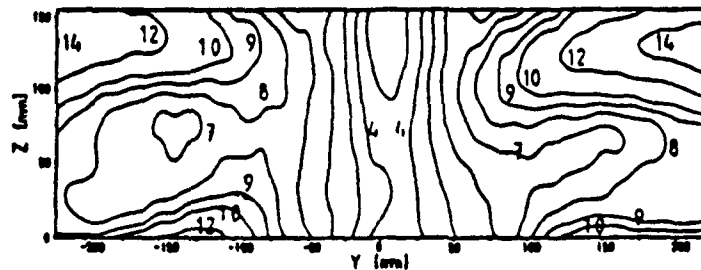
c)  $\alpha = 25.0^\circ$



d)  $\alpha = 28.0^\circ$



e)  $\alpha = 30.0^\circ$



f)  $\alpha = 31.5^\circ$

Figure 44. Contours of dimensionless RMS lateral crossflow velocities  $\sqrt{v'^2}/U_\infty$  in the measurement plane at five  $\alpha$ 's. (Adapted from Fig. 13, Ref. 33. Numbers are per cent.)

attack responsible for fin buffeting tend to be in the vicinity of  $10^\circ$  or less. Furthermore the mean incidence of the twin fins on all such aircraft at zero sideslip is known to be quite small. Regarded as a source of "interference" airloads, even the severe turbulence seems therefore unlikely to cause flow separation. One can then speculate that, if the statistical properties of this turbulence were well known, simple or "classical" unsteady aerodynamic theory might be suitable for predicting the pressures and airloads produced thereby.

### B.3 MEASUREMENT AND PREDICTION OF "OPEN-LOOP" BUFFET RESPONSE

In order to save space, prior work will be summarized in a single section which covers both twin-fin response prediction methods and papers dealing mainly with measurements of pressures & response quantities like acceleration, bending moment, etc. The latter have been carried out extensively in flight and on wind-tunnel models down to 6% of full-scale. References 1 and 2, which involve a 13%-scale replica of the F-15, document the first major collection of high-frequency pressure data. In Subsection 2.4 and Appendix A, derivations and numerical details are furnished on the use of those results to construct input forces.

As for the F/A-18, Refs. 7, 11 & 15 present both pressure and response data in the context of describing the McDonnell Aircraft methods for calculating buffet-induced motions, stresses and structural life estimates. Indeed, the "rigid tail" method

of Zimmerman and Ferman (Ref. 11) provided guidance for the scheme applied in the present report.

One of the first attempts to quantify buffeting of twin fins was reported by Lan et al. in Ref. 8 -- a paper which also contains an appendix by Wentz on water-tunnel studies of F/A-18 vortex-fin interaction. One of the most useful contributions of Ref. 8 was a survey of various approaches previously used to predict conventional transonic buffeting. Lan's own formulation of the fin equations of motion appears to neglect the aerodynamic loads due to the motion itself (called  $\bar{A}_{ij}$  in Sect. 2 above, and the input forces are based on vortex strengths from an unsteady version of the Polhamus suction analogy (cf. Ref. 36). These approximations notwithstanding, Ref. 8 does contain fairly successful estimates of response quantities. For example the RMS fin-root bending moment on F/A-18 is found to be 265.4 ft-lb at  $\alpha = 25^\circ$  and flight dynamic pressure  $q_\infty = 30$  psf. If one assumes this moment to scale on  $q_\infty \ell^3$  (with  $\ell$  any reference length), then Fig. 21, Vol. II of Ref. 11 yields a corresponding RMS of 405 ft-lb. At  $\alpha = 30-32^\circ$  and the same dynamic pressure, a value of about 1200 ft-lb is estimated here in Subsection 4.1, and it is known that the airloads are considerably higher at the higher angle of attack.

Lee and coauthors at Canadian Research Council have been responsible for a comprehensive series of buffet measurements relevant to the CF-18 model of this fighter. Reference 5 describes the coordinated products of a major flight-test program

and wind-tunnel data from an exquisite 6%-scale model. Additional model information has been published in Refs. 17 and 19 (see also the analysis in Ref. 37). Taken at 24 pairs of fin locations in six chordwise rows, pressure histories are recorded on two sides of the rigid model fin. Regrettably full power spectra are not provided for each transducer, and little information is given from which pressure differences  $\Delta p$  can be inferred. For present purposes, it was therefore necessary also to use  $\Delta p$  spectra for five locations on a 12%-scale model from Vol. II of Ref. 1 and to integrate data from both sources during estimation of the input generalized forces employed in Sects. 2-4.

It is assumed that full data traces from the 6% model must have been preserved and that they form the basis of various response predictions reported for the CF-18 (Ref. 5 and elsewhere). Given these traces along with adequate computational resources, one could certainly improve the precision of calculated benefits of active buffet control.

Several other programs involving buffet measurements deserve mention. The Australian Aeronautical Research Laboratory (e.g., Ref. 38) studied F/A-18 models of 1/48-scale in a water tunnel and 1/9-scale in a low-speed wind tunnel. In both instances the effects of adding LEX fences were emphasized. Flow visualization in water determined vortex burst behavior, whereas fin accelerations and unsteady surface pressures were reported from the 1/9-scale model. The favorable influences of the fences found by other investigators were fully confirmed.

Also on F/A-18, but at 1/6-scale on a flexible model in the NASA Langley Research Center Transonic Dynamics Tunnel, Ref. 39 reports fin bending moments and values of a "buffet intensity parameter" proposed by Mabey & others (e.g., Ref. 40). Data are given for  $\alpha$ 's from  $-10^\circ$  to  $+40^\circ$  and for Mach Nos.  $M$  between 0.3 and 0.95. In agreement with all other investigations, buffet response was found to be highest in the range  $\alpha = 30^\circ - 40^\circ$ . By contrast with Refs. 1, 11, etc., however, Ref. 39 concludes that the response was not linearly proportional to dynamic pressure  $q_\infty$ . This apparent inconsistency is believed due to two facts, the first of which is that the tests were carried well into the transonic  $M$ -regime. Here shocks can affect the loading, but under conditions beyond where the high- $\alpha$  phenomenon can occur in flight. The second reason is that the Ref. 39 model had flexible fins with different natural frequencies, which responded primarily in their respective first bending modes. Over a variety of test conditions, even though the driving pressure inputs were  $q_\infty$ -proportional, one would not necessarily observe the same proportionality in the bending moment responses.

Additional measurements of vortex-fin interaction have been undertaken by Shah et al. (Ref. 41) and quite recently by Washburn, Jenkins and Ferman (Ref. 42). Although it deals with a simplified configuration consisting of twin fins mounted above a  $76^\circ$  delta wing, Ref. 42 is especially interesting because of the varied locations of rigid and flexible tails. Measurements include surface vortex flow visualizations, aerodynamic loads &



pressures, strains and other response quantities. The program is ongoing, so that further results may be anticipated in the near future from the Ref. 42 authors and colleagues.

Finally this review of fin buffet research would be incomplete without mention of NASA's High Alpha Technology Program (HATP), and in particular the tests of a full-scale F/A-18 in the Ames Research Center 80 ft-by-120 ft tunnel. The first buffet-related results of this program were described by Meyn and James in Ref. 43. Their instrumentation consisted of 16 pairs of unsteady pressure transducers in four chordwise rows on the fin.  $\alpha$ 's between  $18^\circ$  and  $50^\circ$  were studied along with a range of sideslip angles (only zero sideslip reported in Ref. 43). Especially at the higher Strouhal numbers, typical power spectra of  $\Delta p$  are shown to agree well with 12% scale data from Ref. 11; the value of  $f\ell/U_\infty$  at the  $\alpha = 32^\circ$  spectral peak is about 0.5 vs 0.6 at small scale, despite a difference of a factor of eight between the Reynolds Nos. Properties of fin root bending moments -- found by integration of contributions from the 16  $\Delta p$ 's -- are given with LEX fence off and on. Again, the latter configuration produces considerably lower moments except above  $\alpha = 40^\circ$ , where the authors note that vortex burst has moved ahead of the fence location.

As one point of comparison with the present study, it is remarked that, with LEX fence on at  $\alpha = 32^\circ$  and  $q_\infty = 33$  psf, an RMS bending moment of 830 ft-lb is calculated in Ref. 43. For the same  $\alpha$ -range at  $q_\infty = 300$  psf, Sect. 4 below estimates this

moment at 12,000 ft-lb. Direct scaling on  $q_\infty$  would reduce this to 1320 ft-lb at the wind-tunnel condition; as in the comparison with Ref. 8, it is expected that elastic response of the fin structure would cause this last figure to be somewhat higher than the 830 ft-lb.

At the time of writing, additional full-scale unsteady pressure measurements had just been completed. NASA had instrumented the right fin of the F/A-18 with 48 pairs of transducers, and USAF the left fin with 36 pairs. When these data are reduced and spectral-analyzed, another valuable source of buffet excitation will become available.

#### B.4 PASSIVE AND ACTIVE CONTROL OF FIN BUFFETING

The use of various passive and active schemes for modifying the vortex pattern generated by forebodies of highly-maneuverable aircraft -- and thereby improving aerodynamic control in various ways -- has recently formed a subject of intensive research and application. Primarily in a context of lateral-directional control, Malcolm published in mid-1993 a very complete survey (Ref. 44). Although it was not specifically covered in that review, several of the approaches discussed therein are relevant to the buffet phenomenon. The present subsection summarizes some additional literature.

If one selects the word "passive" to characterize aerodynamic devices of fixed or slowly-varying geometry, then surely the

LEX fences installed on the F/A-18 fleet are the most significant and successful in this category. As described in Ref. 5 and elsewhere, they are the final product of considerable testing, involving 125 fence variants. The final shapes chosen were thin streamwise plates, 8.3 in high, 32 in long and with 30°-swept leading and trailing edges, installed alongside position lights adjacent to the cockpit. As referenced above, they caused the buffet response to drop by roughly one-half in the  $\alpha$ -range of greatest severity.

Two other passive concepts for buffet alleviation are examined at model scale in a paper by Rao et al. (Ref. 45). They consisted of 1.) fences erected by hinging & rotating a portion of each F/A-18 LEX about an axis parallel to the fuselage, and 2.) small dorsal extensions ahead of the fin leading edges. As can be seen from "buffet factors" plotted on Fig. 10 of Ref. 45, both were effective in reducing fin structural response, especially at  $\alpha$ 's above 30°.

On the borderline between passive and active control would be the employment of devices like constrained viscoelastic layers, tuned vibration absorbers, tuned dampers, etc. In personal conversation with C. Johnson, president of CSA Engineering, Inc., RANN, INC. has learned of their proprietary work on tuned dampers for reducing F/A-18 buffet response. The initial CSA investigation, under U.S. Navy support, has demonstrated the effectiveness of this approach.

As for fully active control, Triplett in Ref. 2 mentioned that feedback to the F-15 rudder was under consideration in the early 1980's to improve structural life. In fact, "elastic mode suppression" has been used for various purposes on large aircraft since at least the Boeing 747 and the B-1 bomber (see, e.g., Ref. 46). Three examples are known to the authors of recent investigations directly relevant to fin buffet. One consists of blowing or sucking air along the LEX or wing leading edges, which can be done in a steady or time-dependent fashion. Reference 47 describes wind-tunnel testing at University of Bath, England, on a generic  $60^\circ$ -delta wing model with twin fins. Various flow-field measurements were made, including laser light visualizations and unsteady pressures on the fins. Especially interesting was the effect of tangential air-jet blowing along the wing (TLB). This reduced both the strength and height of the primary vortices, roughly in proportion to the blowing coefficient. In turn, the  $\alpha$  for a given level of buffet excitation was increased, from which there followed a possible overall diminution of potential fatigue damage to the fin. It is noted that TLB has been pursued for several years by Wood and colleagues as an approach to various kinds of flight-vehicle control (e.g., direct-lift augmentation, roll control, pitch damping). Because of its versatility, it is regrettable that this scheme is so difficult to implement practically on an operational aircraft. (See also Ref. 48.)

A briefing by Reed (Ref. 49) describes the efforts of Dyna-

mic Engineering, Inc., to adapt a device developed by them to modify actively the fin response. This consists of a vane/cylinder exciter originally intended for wind-tunnel flutter testing. It operates by means of a rotating cylindrical vane at the trailing edge of a small lifting surface. Under active control from nearby accelerometers, it is proposed to be attached to the tip of a 1/6-scale model of the F/A-18 available for testing at NASA's Transonic Dynamics Tunnel. This approach is believed to have promising potential.

A technology that goes by the generic name of "smart structures" is also felt to have long-range potential in the present context. Piezoelectric or piezoceramic plates can be inserted into existing or newly-designed structure with the objectives of sensing and/or effecting rapid shape changes. Previously used for suppressing vibration, refining the figure of optical surfaces and the like, these have now been adapted by Hanagud (Ref. 50) to fin buffeting. On a full-scale F-15 in the laboratory, velocity feedback to piezoceramic actuators was shown to reduce the sinusoidal response at a resonant condition by "more than fifty percent."